

PHASE 2 INITIAL BOREHOLE DRILLING AND TESTING, IGNACE AREA

*WP10 – Geological Integration Report for Borehole
IG_BH04*

APM-REP-01332-0372

October 2022

Nuclear Waste Management Organization

nwmo

NUCLEAR WASTE
MANAGEMENT
ORGANIZATION

SOCIÉTÉ DE GESTION
DES DÉCHETS
NUCLÉAIRES



Nuclear Waste Management Organization
22 St. Clair Avenue East, 4th Floor
Toronto, Ontario
M4T 2S3
Canada

Tel: 416-934-9814
Web: www.nwmo.ca

**Phase 2 Initial Borehole Drilling and Testing, Ignace
Area**

**WP10 – Geological Integration Report for Borehole
IG_BH04**

APM-REP-01332-0372

October 2022

Nuclear Waste Management Organization

Document History

Title:	Phase 2 Initial Borehole Drilling and Testing, Ignace Area. WP10 – Geological Integration Report for Borehole IG_BH04		
Report Number:	APM-REP-01332-0372		
Revision:	R000	Date:	October 2022
Author Company(s)	Nuclear Waste Management Organization		
Authored by:	Aaron DesRoches, Andrew Parmenter, Stefan Markovic (NWMO)		
Verified by:	Raymond Munier		
Accepted by:	Sarah Hirschorn (Geoscience Director)		

Revision Summary		
Revision Number	Date	Description of Changes/Improvements
R0	2022-10	Initial issue

ABSTRACT

Title: Phase 2 Initial Borehole Drilling and Testing, Ignace Area.
WP10 – Geological Integration Report for Borehole IG_BH04

Report No.: APM-REP-01332-0372

Author(s): Aaron DesRoches, Andrew Parmenter, Stefan Markovic (NWMO)

Company: Nuclear Waste Management Organization

Date: October 2022

The Initial Borehole Drilling and Testing project in the Ignace Area, Ontario is part of Phase 2 Geoscientific Preliminary Field Investigations of the Nuclear Waste Management Organization's (NWMO) Adaptive Phased Management (APM) Site Selection Phase. This project involves the drilling and testing of several deep boreholes within the northern portion of the Revell batholith. Borehole IG_BH04 is located approximately 23 km southeast of the Wabigoon Lake Ojibway Nation and 42 km northwest of the Town of Ignace. Access to the IG_BH04 drill site is via Highway 17 and a network of logging roads. This Geological Integration Report serves as the primary reference of the geological findings from the borehole drilling and testing activities at IG_BH04.

The objective of the Geological Integration Report is to summarize the main geological findings and provide an initial interpretation of the rock type and structural characteristics of the geosphere intersected by borehole IG_BH04, including delineation of rock unit and structural unit domains. In addition, distinct intervals of higher fracture frequency identified along the length of the borehole are documented. These components represent an initial geological model for IG_BH04 which can be further used in developing a site-scale 3D geological model.

Findings and uncertainties are summarized at the end of the report. One primary consideration is the understanding that the available information *is from a single borehole*. Whether or not the characteristics of the bedrock interpreted in this report will be representative of characteristics in other boreholes remains uncertain.

TABLE OF CONTENTS

ABSTRACT iii

1	INTRODUCTION.....	1
1.1	Technical Objectives and Scope of Report.....	1
2	Background Information.....	2
2.1	Geological Setting	2
2.2	Background and Overview of Borehole Drilling and Testing.....	5
2.2.1	Drilling Site Description.....	5
2.3	Borehole Construction Details for IG_BH04	7
2.3.1	Borehole Deviation Analysis	8
3	Integrated Geological Interpretation.....	10
3.1	Data Used for Geological Interpretation	11
3.1.1	Terminology	12
3.2	Geological Results	13
3.2.1	Lithological Interpretation.....	13
3.2.2	Alteration Interpretation	30
3.2.3	Rock Unit Classification	33
3.2.4	Structural Interpretation	37
3.2.4.1	Structures	40
3.2.4.2	Interpreted Fracture Sets.....	56
3.2.4.3	Fracture Infill Minerals	59
3.2.5	Structural Unit Classification.....	68
3.2.6	High Fracture Frequency Intervals (HFFIs)	70
4	Summary of Findings and Uncertainties.....	85
4.1	Findings.....	85
4.2	Uncertainties	89
5	References 91	
Appendix A:	 Summary List of Work Packages Completed for IG_BH04.....	93
Appendix B:	 Petrography and lithogeochemistry data.....	95

Appendix C:	Geophysical Near and Far Density Log Correction	102
Appendix D:	Structure log integration methodology	105
Appendix E:	Stereonets of Fractures by Structural Unit	109
Appendix F:	Stereonets of IG_BH04 High Fracture Frequency Intervals (HFFI)	113
Appendix G:	Summary of borehole logs at 1:1,000 scale	117

LIST OF TABLES

Table 1: Details of Borehole Diameter for IG_BH04	8
Table 2: Summary of Rock Types Encountered in IG_BH04	13
Table 3: Summary average of major oxides in the rock types of IG_BH04. Note that only 3 main rock types broadly classified as biotite granodiorite-tonalite were analyzed.	18
Table 4: Mean geophysical response values for each logged rock type.....	27
Table 5: Summary of alteration assemblages observed in IG_BH04 during geological core logging. Note that because multiple alteration assemblages could be logged in the same interval, the sum of total alteration logged is greater than the length of the borehole.	31
Table 6: Summary of Classified Rock Units	36
Table 7: Summary of structures observed in the borehole.....	37
Table 8: Summary of interpreted fracture sets in the borehole. Presents the general description of the orientation with a mean dip and dip direction.	58
Table 9: Position ranges and standard statistics for fracture frequencies captured within the defined structural units (SU) within the borehole.....	70
Table 10: High Fracture Frequency Intervals from IG_BH04	73

LIST OF FIGURES

Figure 1: Location and Geological setting of borehole IG_BH04 in the northern portion of the Revell batholith.....	3
Figure 2: Location of the drilling site for borehole IG_BH04.....	6
Figure 3: Aerial view of the site, looking northeast. Access road is in the lower right corner of photo.	7
Figure 4: Schematic of Borehole IG_BH04 showing casing, wedge, and grout locations/intervals (Wood, 2021a).....	8
Figure 5: Compilation of borehole IG_BH04 deviation measurements. Data sets include up- and down-hole televiwers surveys and gyro surveys. Average and standard deviation between the gyro and televiewer survey measurements are presented. Final borehole path (easting, northing, TVD) is defined based on final gyro measurements from the Sprint-IQ survey.	9
Figure 6: a) Borehole deviation presented as the total borehole closure versus true vertical depth; and b) bullseye plot showing the planned borehole trajectory (black) compared to the final Reflex EZ-gyro survey trajectory (red).	10
Figure 7: Input datasets used to derive a final lithology log. From left: optical televiewer log, four suites of continuous geophysical logs that aid in distinction of rock types, logged alteration (by type), and final lithology log. Due to the low spectral gamma counts, K, U and Th were evaluated using a 10 m window, resulting in a smoothing of their profiles. Note also that due to low spectral gamma counts, K, U and Th contents could not be reliably reported in % or ppm. Grey band represents the zone of influence of steel wedge.	15
Figure 8: Classification/nomenclature of felsic granitoid phases according to the normalized modal mineral content (Quartz + Alkali-feldspar + Plagioclase = 100 Vol%) as determined	

- from investigation of 30 samples. Average modal mineralogy for each sample was determined semi-quantitatively using polished thin sections and plotted on a simplified ternary Streckeisen diagram after Le Bas and Streckeisen (1991).17
- Figure 9: Plutonic Rock Classification (Debon and Le Fort, 1983). Diagram axes correspond to proportions of K-feldspar and plagioclase to quartz. P is calculated from $(K-(Na+Ca))$ and Q is calculated from $((Si/3) - (K+Na+(2*Ca)/3))$. Parameters calculated as oxide percentages converted to millications.19
- Figure 10: Representative example of biotite granodiorite-tonalite (sample IG_BH04_MG010). a) Core sample photograph. b) Photomicrograph showing a coarse zoned subhedral plagioclase crystal with abundant muscovite and some epidote in the core of the crystal; sample 04-MG010, cross-polarized light. c) Photomicrograph showing a zoned euhedral zircon and a diminutive subhedral apatite surrounded by alkali feldspar (K-feldspar) and plagioclase; sample IG_BH04_MG010, cross-polarized light. Sericite (white mica) alteration can be seen in cores of plagioclase crystals; crossed polarizers transmitted light.....20
- Figure 11: Representative example of biotite granodiorite-tonalite (sample IG_BH04_MG016). a) Core sample photograph. b) Photomicrograph of thin section showing titanite associated with biotite and epidote in sample 04-MG016, plane polarized light; c) Same view as Figure 10b, cross-polarized light.....22
- Figure 12: Representative examples of a granodiorite-tonalite (feldspar-phyric tonalite subunit) (IG_BH04_MG030). a) Core sample photograph. b) Photomicrograph showing a coarse zoned subhedral plagioclase porphyroclast with inclusions of muscovite; sample 04-MG030, cross-polarized light. c) Photomicrograph showing chlorite with Berlin blue birefringence that replaced a biotite grain; plagioclase (on the of central chlorite grain) is extensively 'sericitized' (replaced by fine muscovite); sample 04-MG030, cross-polarized light.23
- Figure 13: Representative examples of subordinate rock types: a) Amphibolite (619.21- 619.34 m), b) Feldspar-phyric tonalite dyke (435.50-435.61 m), c) Quartz dyke (989.13-989.18 m), d) Aplite dyke (761.60-761.65 m)24
- Figure 14: Chondrite-normalized rare-earth element (REE) plot (after Taylor and McLennan, 1985) of rock types from IG_BH04 and a representative average of 2.8 Ga low-heavy REE (HREE) tonalite-trondhjemite-granodiorite (TTG) from the Fennoscandian shield (black squares; Halla, 2018). Y-axis shows concentrations (expressed as logarithm to the base 10 of the value) of REE (x-axis, by atomic number) in IG_BH04 samples normalized to a reference Chondrite standard. REE patterns of biotite granodiorite-tonalite and feldspar-phyric biotite granodiorite-tonalite demonstrate steep fractionation and significant depletion of HREE.....26
- Figure 15: Violin plots show the distribution of geophysical log responses associated with the logged rock types. Each violin shows the distribution of the data values with the median (thick dashed line), and quartiles (thin dashed lines) marked. Rock types are ordered based on total data counts from left to right in each graph.....29
- Figure 16: Cross plots showing correlations between neutron, density, natural gamma and potassium count values of all rock types encountered in IG_BH04. Colored points represent mean values of the geophysical responses and the error bars represent standard deviation30
- Figure 17: Alteration types and distribution along the borehole based on geological core logging and analysis of the optical televiewer log resulting in a final alteration log. A2 indicates

intervals with slight alteration, A3 indicates intervals with moderate alteration, and A4 indicates intervals where alteration is pervasive along the borehole length.....	32
Figure 18: Common alteration assemblages logged in IG_BH04. A) Potassic alteration: Pink to orange discoloration, halos around quartz and feldspar crystals, interpreted as formation of secondary K-feldspar. B) Chloritization: Core photo displays epidote/chlorite fracture infill, with minor iron oxide (hematite), and weak bleaching around the fractures in tonalite. C) Hematization: Photo shows a contact between tonalite and mafic/amphibolite unit; on the left side of the photo hematite alteration is visible in tonalite as a reddish / rusty discoloration. The mafic unit displays chlorite alteration; the chlorite is partially to completely replacing biotite (field-level interpretation). D) Silicification: Core photo displays light to medium grey discoloration. E) Carbonatization: Core photo displays the contact between a tonalite and an amphibolite. The foliated, light grey, amphibolite displays pervasive carbonate alteration. F) Bleaching: Note a patch exhibiting apparent whitening (~51-58cm). G) Sericitization: Note white alteration patches reflecting the presence of fine white mica. H) Albitization: White phenocrystals were interpreted as partial to complete replacement of original plagioclase.	33
Figure 19: Summary of final logged lithology, alteration and key geophysical logs presented alongside interpreted rock units for IG_BH04. Due to the low spectral gamma counts, K, U and Th were evaluated using a 10 m window, resulting in a smoothing of their profiles.....	35
Figure 20: Equal Area Lower Hemisphere Projection (stereonet) showing poles to planar structural measurements, unweighted (n = 2550).	38
Figure 21: Equal Area Lower Hemisphere Projections (stereonets) showing a summary of the poles for planar structural measurements. Top: all data – contours, unweighted (n = 2550). Bottom: all data – contours, Terzaghi-weighted (n = 5066).....	39
Figure 22: Examples of primary igneous and ductile structures. a) Subtle variation in biotite content (from left to right) defining a primary igneous layering, in biotite granodiorite-tonalite (770 m along borehole). b) Weak foliation defined by alignment of biotite.....	41
Figure 23: Stereonet showing poles and unweighted contours for Igneous Primary Structures (IPS; n = 45).	42
Figure 24: Stereonet showing poles and unweighted contours for all oriented geological contacts (n = 44).	43
Figure 25: Stereonet showing poles for amphibolite contacts (n = 20). Open symbols identify broken contacts (BR) and filled symbols identify intact contacts (IN).	44
Figure 26: Stereonet showing the distribution of poles to contacts for felsic rock occurrences, including aplite (n = 2), feldspar-phyric tonalite (n= 4) and quartz (n = 2) dykes, and biotite tonalite (n = 13) and feldspar-phyric biotite granodiorite-ton	45
Figure 27: Summary log showing the frequency per metre of brittle structures (left) in comparison to stick plots that show the distribution of all brittle structures (Joints – JN, Veins – VN and Faults - FLT) and all ductile structures (Shear Zones – SHR and Foliation – FO).	46
Figure 28: Stereonets showing orientation information for Foliation (FO). All data – poles, unweighted (n = 8).....	47
Figure 29: Stereonets showing orientation information for Shear Zones. Top: All data – poles and contours, unweighted (n = 26). Bottom: All Shear Zone data, Terzaghi-weighted contours (n = 38).	48

Figure 30: Examples of brittle structure. a) Broken hairline joint with iron stain and hematite alteration, in biotite granodiorite-tonalite (278 m). b) Broken joint with no surface alteration cross-cutting intact joint, in biotite granodiorite-tonalite (172 m). Note that mm-scale geological aperture logged for broken joint was reduced to 0 mm based on televiewer interpretation. c) Intact mm-scale quartz-filled vein, in biotite granodiorite tonalite (593 m). d) Intact hairline to mm-scale epidote and calcite-filled veins surrounded by hematite alteration, in feldspar-phyric biotite granodiorite-tonalite (946 m). e) Broken fault plane with quartz infill, in biotite granodiorite-tonalite (827 m). f) Soft-gouge-filled fault zone at sheared and altered contact between amphibolite (left) and biotite granodiorite-tonalite (right; 579 m).	49
Figure 31: Stereonets showing orientation information for Joints (JN). Top: All data – poles and contours, unweighted (n = 2162). Open symbols identify broken Joints (JN-BR) and filled symbols identify partially intact/intact Joints (JN-PIN/IN). Bottom: All Joint data, Terzaghi-weighted contours (n = 4318).	51
Figure 32: Stereonets showing orientation information for all Veins (VN). Top: All data – poles and contours, unweighted (n = 300). Open symbols identify broken Veins (BR) and filled symbols identify partially intact/intact Veins (PIN/IN). Bottom: All Vein data, Terzaghi-weighted contours (n = 609).	53
Figure 33: Stereonets showing orientation information for Faults (FLT; n = 8) and a Broken Core Zone (BCZ; n = 1). Open black symbols identify poles to broken Faults (BR) and filled black symbols identify poles to partially intact/intact Faults (PIN/IN). The red symbol identifies the pole to the Broken Core Zone.	54
Figure 34: Stereonet plot showing poles to all fracture planes logged as broken during geological core logging, with unweighted contours (n = 180).	55
Figure 35: Stereonet plot showing poles to all fracture planes logged as intact or partially intact, with unweighted contours (n = 2288).	55
Figure 36: Stereonets of all oriented fractures, including all joints, veins and faults. Top: All fractures – poles, unweighted (n = 2468). Identified pole clusters are colour-coded to highlight their distribution. Middle: All fractures – contours (n = 2468), unweighted. Bottom: All fractures – contours, Terzaghi-weighted (n = 4934). Middle and bottom stereonet are overlain by final fracture set interpretation. See text and Table 9 for additional summary. .	57
Figure 37: Summary log showing the frequency per metre of all brittle structures (left) in comparison to stick plots that show the distribution of all fractures assigned to defined fracture sets 1, 2, and 3, as well as unassigned random fractures. It is understood that there is some uncertainty in the present assessment, including based on the relatively large number of fractures remaining unassigned. The fracture set interpretation will continue to be refined as other boreholes are drilled in different directions.	59
Figure 38: Summary log showing the frequency per metre (Fracture Freq.) of all brittle structures (left) in comparison to stick plots that show the distribution of the most common infill mineral phases including quartz (Qz), chlorite (Chl), iron oxide stain (Fe), calcite (Ca), epidote (Ep), a granitic (Gt) assemblage that includes some combination of alkali-feldspar (Afs) with quartz, plagioclase and biotite, and, fractures that exhibit either clay (Cl), broken rock (Br), or soft clay gouge (Go_So).	60
Figure 39: Stereonet plot showing poles to all fracture planes logged with quartz +/- chlorite, calcite, iron oxide stain, epidote, or rarely pyrite (n = 602).	61
Figure 40: Stereonet plot showing poles to all fracture planes logged with chlorite (n = 590)	62

- Figure 41: Stereonet plot showing poles to all fracture planes logged with iron staining (n = 202).63
- Figure 42: Stereonet plot showing poles to all fracture planes logged with calcite (n = 362).....64
- Figure 43: Stereonet plot showing poles to all fracture planes logged with epidote (n = 354). ...65
- Figure 44: Stereonet plot showing poles to all fracture planes logged with granitic infill, including alkali-feldspar +/- quartz, plagioclase and biotite (n = 342).66
- Figure 45: Stereonet plot showing poles to all fracture planes logged with clay, broken rock, or soft gouge (n = 37).67
- Figure 46: Stereonet showing poles to all fractures logged as having no identifiable mineral infill phase. Fractures logged in 'televiewer' (TV) datasets only, geological 'core' logging only (Core), or identified in 'both' datasets, are distinguished (n = 745).68
- Figure 47: Per metre fracture frequency (left), the sum of aperture per metre (centre) and cumulative fracture frequency curve (right) showing vertical distribution of all logged joints, faults, and veins along the borehole. The cumulative fracture frequency curve shows changes in slope where boundaries in structural units (SU) are defined. Structural unit boundaries are marked on the figure, and their positions are described in Table 9.69
- Figure 48: High fracture frequency intervals (HFFIs) interpreted based on fracture intensity from borehole fracture frequency log. Six high fracture frequency intervals are outlined by interval depths and the red dashed line represents the peak location. Stick plots indicate the distribution of each fracture type (joint, vein, fault) along the length of the borehole. ...72
- Figure 49: Terzaghi-weighted stereonet plot of fractures (JN, VN) within high fracture frequency interval HFFI_1 from 94.08 – 116.97 m. Two peaks are defined, a major peak with a mean orientation of 228/84 (best fit plane shown as black great circle) and a minor peak with a mean orientation of 292/86 (best fit plane shown as grey great circle; Dip Direction/Dip convention).74
- Figure 50: Core from a portion of HFFI_1 (95.17 – 110.00 m). Biotite granodiorite-tonalite is characterized by well spaced, shallow and steeply dipping fractures.75
- Figure 51: Core from a portion of HFFI_2 (309.27 – 326.69 m). Biotite granodiorite-tonalite with visible pink alteration logged mainly as hematization and potassic alteration. There is a local increase in fracturing in proximity to the zones of alteration76
- Figure 52: Boxed core images showing the majority of the HFFI_3 (from 424.54 – 442.06 m). Interval is dominated by biotite granodiorite-tonalite with a 1 m interval of feldspar-phyric tonalite dyke. Pink coloured alteration is present throughout the length of the core interval logged mainly as potassic alteration and minor chloritization. Carbonatization is logged within the feldspar-phyric tonalite dyke. Fractures are well spaced in the biotite granodiorite-tonalite and more concentrated within the dyke.77
- Figure 53: Boxed core images showing a portion of HFFI_4 (a: 570.33 – 587.67 m). Interval is dominated by biotite granodiorite-tonalite with a 0.5 m interval of amphibolite. Pink coloured alteration is present throughout the length of the core interval logged mainly as potassic alteration and hematization. Fracture intensity peaks within the amphibolite and continues as a broad highly fractured interval into the biotite granodiorite-tonalite rock deeper in the interval.78
- Figure 54: Boxed core images showing the majority of the HFFI_5 (from 616.74 – 637.03 m). The interval starts in amphibolite, transitioning down hole across a sheared contact into

variably altered biotite granodiorite-tonalite. A visibly dark grey section of the biotite granodiorite-tonalite is a result of silicification, hematization and potassic alteration. Brittle structures throughout the interval dip moderately to steeply towards the SW, W, and NW.80

- Figure 55: Boxed core images showing the majority of the HFFI_6 (from 941.02 – 978.01 m). The interval starts with two amphibolites, interlayered with feldspar-phyric biotite granodiorite-tonalite. The majority of the interval exhibits chloritization, most evident in association with distinct bleached halos around fractures in the feldspar-phyric biotite granodiorite-tonalite. Epidote, iron oxide, and calcite infilled fractures are common. The majority of brittle structures are near vertical and strike NNE.82
- Figure 56: Lineament traces near IG_BH04 interpreted from LiDAR DEM and airborne geophysics data (DesRoches et al., 2018). Lineament traces are dominantly north-northeast trending, with fewer westerly to northwesterly trending lineaments. The approximate trace of IG_BH04 is shown as a white line.84
- Figure 57: Rose diagram of the lineaments (N = 94) around IG_BH04 (see Figure 56) interpreted from LiDAR DEM and airborne geophysics data (DesRoches et al., 2018). a) Unweighted; b) Length-weighted to highlight more prominent lineaments. Lineament orientations are plotted using a bin size of 15 degrees.85
- Figure 58: Rose diagrams of the borehole logged fracture orientations using a minimum dip angle of 45 degrees, and bin size of 5 degrees. a) Unweighted (N = 1706 is the total number of fractures); b) Terzaghi-weighted to account for directional bias of the borehole path (weighted N = 3945 is the sum of the weightings).85
- Figure 59: Summary log of geological information, including (from left to right), final log of lithology, alteration, classification of rock units, per metre fracture frequency, and structural units, representing the 1-dimensional geological model for IG_BH04.87

1 INTRODUCTION

Borehole Drilling and Testing project in the Ignace Area, Ontario is part of Phase 2 Geoscientific Preliminary Field Investigations of the Nuclear Waste Management Organization's (NWMO) Adaptive Phased Management (APM) Site Selection Phase.

Following the first stage of the Phase 2 Initial General Field Studies summarized by Golder (2015) and in collaboration with the community, an area located in the northern portion of the Revell batholith was selected by the NWMO for further investigation through an initial borehole drilling campaign, which involves drilling and testing of several deep boreholes. The location of IG_BH04 is shown in Figure 1 and Figure 2. IG_BH04 had a planned inclination of -70° towards an azimuth of 110° . Further details on the final borehole path are presented in Section 2 of this report.

Borehole IG_BH04, is located approximately 21 km southeast of the Wabigoon Lake Ojibway Nation and 43 km northwest of the Town of Ignace. Access to the IG_BH04 drill site is via Highway 17 and a network of logging roads (Figure 2). This single borehole integration report serves as the primary reference of the geological findings from the borehole drilling and testing activities at IG_BH04.

The borehole coring, and geological logging and sampling were carried out by a team led by Wood Canada Ltd. (Wood) on behalf of the NWMO. Downhole geophysics was carried out by Golder Associates Ltd. (Golder) on behalf of the NWMO. The borehole drilling and coring, and geological and geotechnical core logging activities are described in two separate technical reports (Wood, 2021a and Wood, 2021b) including activities related to the mobilization and set up of the borehole drilling site, the recovery and logging of the bedrock core, drilling water management and groundwater sampling. The borehole geophysical logging activities carried out by Golder are described in Golder (2022). All activities are documented in work package (WP) data reports that describe test methods, collected data and calculations, where applicable. The full list of work packages and associated data reports is included in Appendix A.

This report, which represents the tenth work package (WP10 Integration and Synthesis), presents an integrated summary of geological and geophysical information collected primarily during the completion of three work packages, including, WP02: Borehole Drilling and Coring (Wood, 2021a), WP03: Geological and Geotechnical Core Logging, Photography and Sampling (Wood, 2021b) and WP05: Geophysical Well Logging and Interpretation (Golder, 2022a).

1.1 Technical Objectives and Scope of Report

The objective of this Geological Integration report is to evaluate relevant data, and provide an interpretation of the lithological and structural characteristics of the geosphere intersected by borehole IG_BH04. This initial interpretation may be revised as further boreholes are drilled to form a holistic interpretation for the geosphere.

Additional information related to developing an understanding of the petrophysical and transport properties of the bedrock of the Revell batholith, as well as the geomechanical, hydrogeological, litho- and hydrogeochemical, and thermal properties will be reported on separately and integrated into a Descriptive Geosphere Site Model (DGSM) report. The DGSM report will summarize the additional borehole- and laboratory-derived data related to these topics and will present this information including a geological model that integrates the WP10 results for each of the boreholes. The information presented in this report, which focuses on IG_BH04, represents the first step in this integration process.

The scope of this Single Borehole Data Integration report is summarized in the following sections:

- Section 1 provides the report introduction and includes the summary of technical objectives and scope of the sections in the report.
- Section 2 first briefly describes the geological setting for the area around the borehole location, and then provides an overview of the borehole drilling and testing activity. This includes a brief site description, a summary of the borehole construction and deviation surveys of the borehole.
- Section 3 presents the integrated summaries of the lithological, alteration and structural characteristics of the bedrock intersected by the borehole (Section 3.2). Then, using this information, an initial geological model, with interpretation of rock units, structural units, and high fracture frequency intervals for the borehole, is presented.
- Section 4 summarizes the findings and addresses uncertainties.
- Appendix A lists all Work Packages and Work Package report names produced as part of the full suite of activities associated with IG_BH04.
- Appendix B presents the petrographic, modal mineralogy and lithogeochemical data, which are summarized in Section 3.
- Appendix C presents a table of values summarizing the correction applied to the geophysical near and far density log.
- Appendix D contains the methodology for integrating the un-oriented structural dataset generated during WP03 with the televiewer geophysical logs collected during WP05 to produce a final log of oriented structures. The integrated structural dataset is presented in Section 3.
- Appendix E presents lower hemisphere equal area projections (stereonet) summarizing the brittle fractures for each structural unit (SU) in the borehole, defined in Section 3.2.5.
- Appendix F presents lower hemisphere equal area projections (stereonet) summarizing the structural orientation information for all high fracture frequency intervals (HFFI) in the borehole, defined in Section 3.2.6.
- Appendix G presents a summary of the borehole logs for IG_BH04 at 1:1,000 scale.

2 BACKGROUND INFORMATION

2.1 Geological Setting

The approximately 2.7-billion-year-old Revell batholith is located in the western part of the Wabigoon Subprovince of the Archean Superior Province. The batholith is roughly elliptical in shape trending northwest, is approximately 40 km in length, 15 km in width, and covers an area of approximately 455 km². Based on recent geophysical modelling, the batholith has a relatively flat base that extends to depths of nearly 4 km in some regions (SGL, 2020). The batholith is surrounded by supracrustal rocks of the Raleigh Lake (to the north and east) and Bending Lake (to the southwest) greenstone belts (Figure 1).

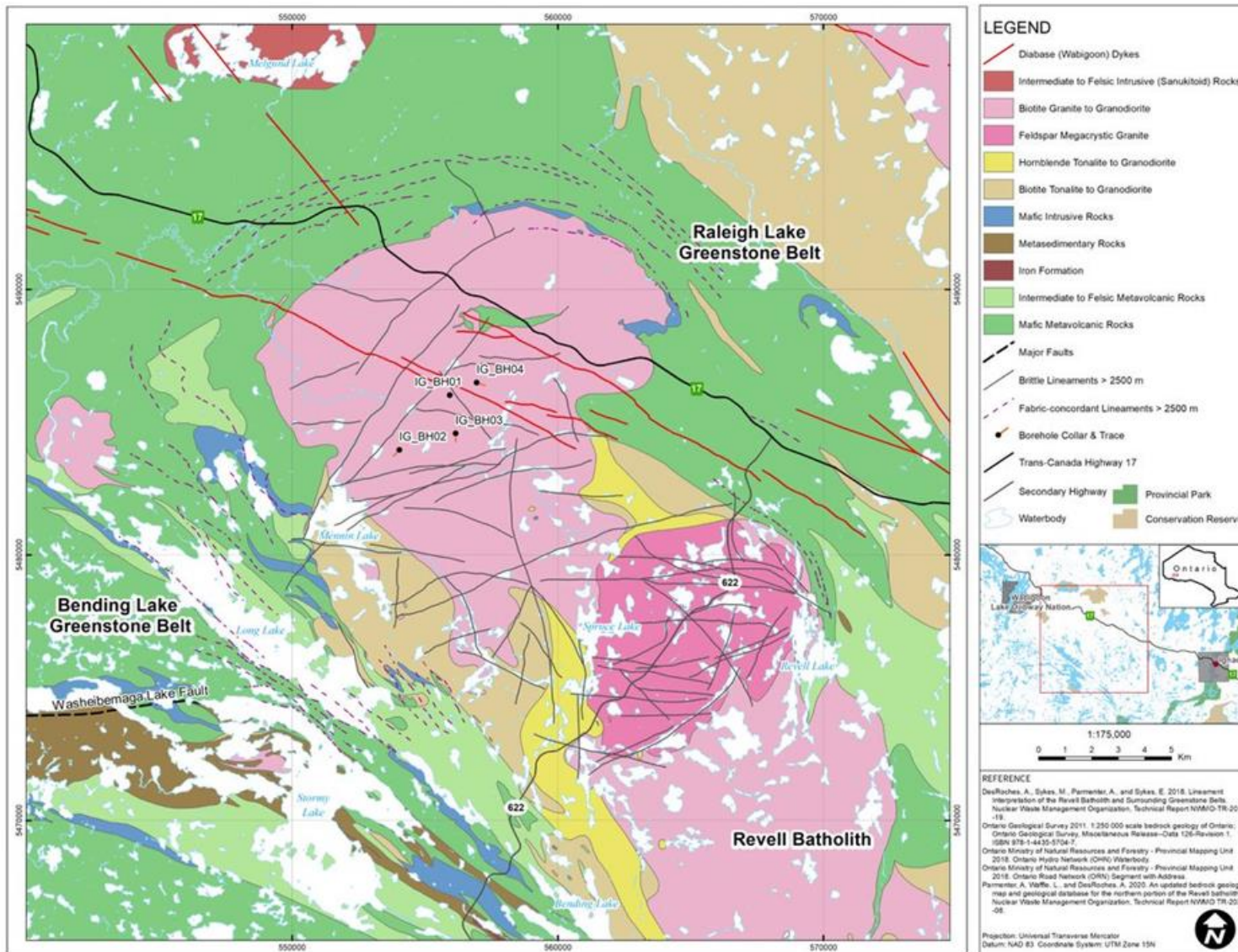


Figure 1: Location and Geological setting of borehole IG_BH04 in the northern portion of the Revell batholith.

Four main rock units are identified in the supracrustal rock group: mafic metavolcanic rocks, intermediate to felsic metavolcanic rocks, metasedimentary rocks and mafic intrusive rocks (Figure 1). Sedimentation within the supracrustal rock assemblage was largely synvolcanic, although sediment deposition in the Bending Lake area may have continued past the volcanic period (Stone, 2009; Stone, 2010a; Stone, 2010b). All supracrustal rocks are affected, to varying degrees, by penetrative brittle-ductile to ductile deformation under greenschist- to amphibolite-facies metamorphic conditions (Blackburn and Hinz, 1996; Stone et al., 1998). In some locations, primary features, such as pillow basalt or bedding in sedimentary rock units are preserved. In other locations, primary relationships are completely masked by penetrative deformation. Uranium-lead (U-Pb) geochronological analysis of the supracrustal rocks produced ages that range between 2734.6 +/-1.1 Ma and 2725 +/-5 Ma (Stone et al. 2010).

Three main suites of plutonic rock are recognized in the Revell batholith (Figure 1), including, from oldest to youngest: a Biotite Tonalite to Granodiorite suite, a Hornblende Tonalite to Granodiorite suite, and a Biotite Granite to Granodiorite suite. Plutonic rocks of the Biotite Tonalite to Granodiorite suite occur along the southwestern and northeastern margins of the Revell batholith. The principal type of rock within this suite is a white to grey, medium-grained, variably massive to foliated or weakly gneissic, biotite tonalite to granodiorite. One sample of foliated and medium-grained biotite tonalite produced a U-Pb age of 2734.2 +/-0.8 Ma (Stone et al., 2010). The Hornblende Tonalite to Granodiorite suite occurs in two irregularly shaped zones surrounding the central core of the Revell batholith. Rocks of the Hornblende Tonalite to Granodiorite suite range compositionally from tonalite through granodiorite to granite and also include significant proportions of quartz diorite and quartz monzodiorite. One sample of coarse-grained grey mesocratic hornblende tonalite produced a U-Pb age of 2732.3 +/-0.8 Ma (Stone et al., 2010). Rocks of the Biotite Granite to Granodiorite suite underlie most of the northern, central and southern portions of the Revell batholith. Rocks of this suite are typically coarse-grained, massive to weakly foliated, and white to pink in colour. The Biotite Granite to Granodiorite suite ranges compositionally from granite through granodiorite to tonalite. This suite includes the oval-shaped potassium-feldspar megacrystic granite body in the central portion of the Revell batholith. One sample of coarse-grained, pink, massive potassium feldspar megacrystic biotite granite produced a U-Pb age of 2694.0 +/-0.9 Ma (Stone et al., 2010).

Borehole IG_BH04 is located in the northern portion of the Revell batholith, inside the Biotite Granite to Tonalite plutonic suite (Figure 1). Bedrock exposure in this part of the batholith is generally very good due to minimal overburden, few water bodies, and relatively recent forestry activities. The bedrock surrounding IG_BH04 is composed mainly of massive to weakly foliated felsic intrusive rocks that vary in composition between granodiorite and tonalite. Bedrock identified as tonalite transitions gradationally into granodiorite and no distinct contact relationships between these two rock types are typically observed (SRK and Golder, 2015; Golder and PGW, 2017). Massive to weakly foliated granite is identified at the ground surface to the southeast of the investigation area. The granite is observed to intrude into the granodiorite-tonalite bedrock, indicating that it is a distinct, younger intrusion (Golder and PGW, 2017).

A west-northwest trending mafic dyke interpreted from aeromagnetic data and observed during detailed mapping to be approximately 15-20 m wide, extends across the northern portion of the batholith (Figure 1; Golder and PGW, 2017). This dyke is associated with several other similarly-oriented mafic dykes that stretch across the northern portion of the Revell batholith and into the surrounding greenstone belts. All of these mafic dykes have a similar character and are interpreted to be part of the Wabigoon dyke swarm. One sample from the same Wabigoon swarm produced a U-Pb age of 1887 +/-13 Ma (Stone et al., 2010), indicating that these mafic dykes are Proterozoic in age. It is assumed based on surface measurements that these mafic dykes are sub-vertical (Golder and PGW, 2017).

Locally, bedrock is well exposed near IG_BH04 outcropping through a thin layer of overburden material and a few small wetlands (Figure 2). The exposed outcrops tend to form elongate linear ridges that have a dominant strike orientation towards the northeast. These ridges are described in DesRoches et al (2018) as northeast trending short and discontinuous linear valleys that may represent the surface expression of structural features that extend into the bedrock. The IG_BH04 is oriented such that it will investigate these potential features in the subsurface and will be summarized in the report below (; DesRoches et al., 2018).

Regional observations from mapping have indicated that fractures tend to be widely spaced (typical 30 to 500 cm spacing range) and dominantly comprised of sub-vertical joints with two dominant orientations trending northeast and northwest (SRK and Golder, 2015; Golder and PGW, 2017). These fracture orientations generally follow the same dominant orientations of brittle lineaments in the northern portion of the Revell batholith (DesRoches et al., 2018). Minor subhorizontal joints have been mapped with minimal alteration, suggesting they are younger and perhaps related to glacial unloading. One mapped regional-scale fault, the Washeibemaga Lake fault, trends east and is located to the west of the Revell batholith (Figure 1). Additional details of the lithological units and structures found at surface in the northern portion of the Revell batholith are provided in Golder and PGW (2017).

2.2 Background and Overview of Borehole Drilling and Testing

2.2.1 Drilling Site Description

The drilling site for borehole IG_BH04 is located approximately 21 km southeast of the Wabigoon Lake Ojibway Nation and 43 km northwest of the Town of Ignace. Access to the IG_BH04 drilling site is via Highway 17 and a network of logging roads. Access to the site was established along existing forest roads approximately 850 m, branching from Dymont road towards the north (Figure 2). The drilling site is approximately 70 m by 50 m and has an area of 3,500 m² (Figure 3). The borehole is located at the southern end of the drilling site. The drilling site was constructed to minimize the need for ground clearing and reduce the effects of erosion from water runoff. A large percentage of the site was rock outcrop, and a compacted aggregate pad was constructed to level off the area. An oblique aerial view of the site looking northeast is shown in Figure 3.

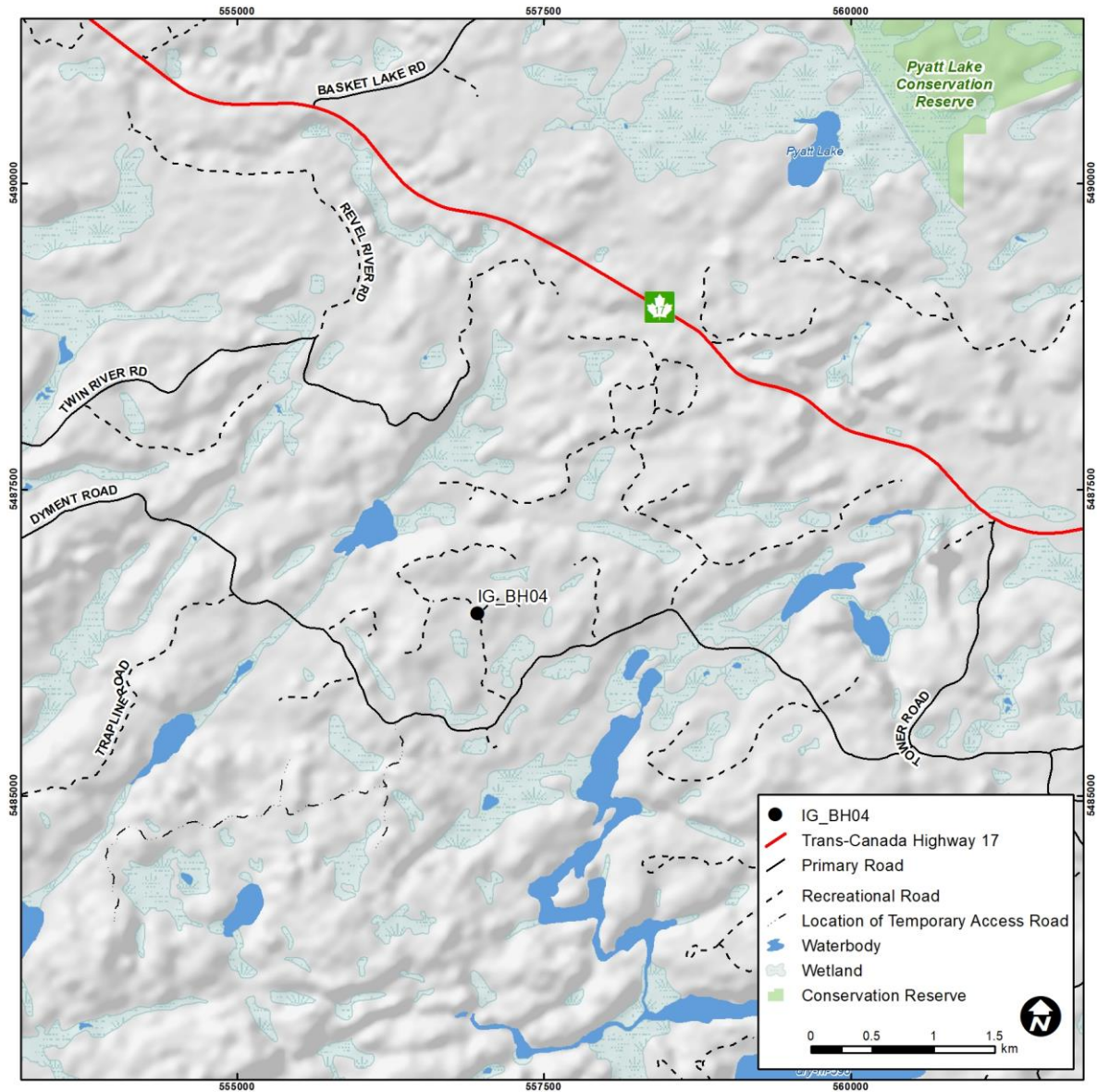


Figure 2: Location of the drilling site for borehole IG_BH04.



Figure 3: Aerial view of the site, looking northeast. Access road is in the lower right corner of photo.

2.3 Borehole Construction Details for IG_BH04

Borehole IG_BH04 was drilled at a planned inclination of -70° towards an azimuth of 110° using a diamond drill. Two sets of casing were installed in the upper parts of the borehole to ensure borehole stability, and reduce mixing of shallow and deep groundwaters. A schematic of the final borehole construction is shown in Figure 4. The down-axis position along the borehole is measured in metres from surface. .

PWT conductor casing was installed and cemented to a position of 5.97 m along the borehole, to prevent drill fluid from escaping through the fractured upper bedrock. No overburden was encountered or recovered during drilling and casing installation. The borehole was drilled to 100.77 m along the borehole and evaluated to determine a position to install the PQ casing. The borehole was reamed, and PQ casing was installed to the bottom of the drilled section at 100.77 m.

The PQ casing was cemented in place using a high sulphate resistant cement (LaFarge). Drilling and coring activities resumed until a depth of 110 m where a hydraulically conductive fracture was encountered. Grout was injected to seal the fracture before drilling resumed for the remainder of the borehole down to a drilled position along borehole of 1000.20 m. During the course of drilling, steel diverted wedges were used to control the deviation of the borehole. Steel wedges were installed at depth intervals of 371.21-377.21 m and 391.21-395.21 m. The final IG_BH04 borehole construction, including casing diameters and positions, and wedge locations are shown in Figure 4 and Table 1 (see Wood, 2021a for complete details on borehole drilling and construction).

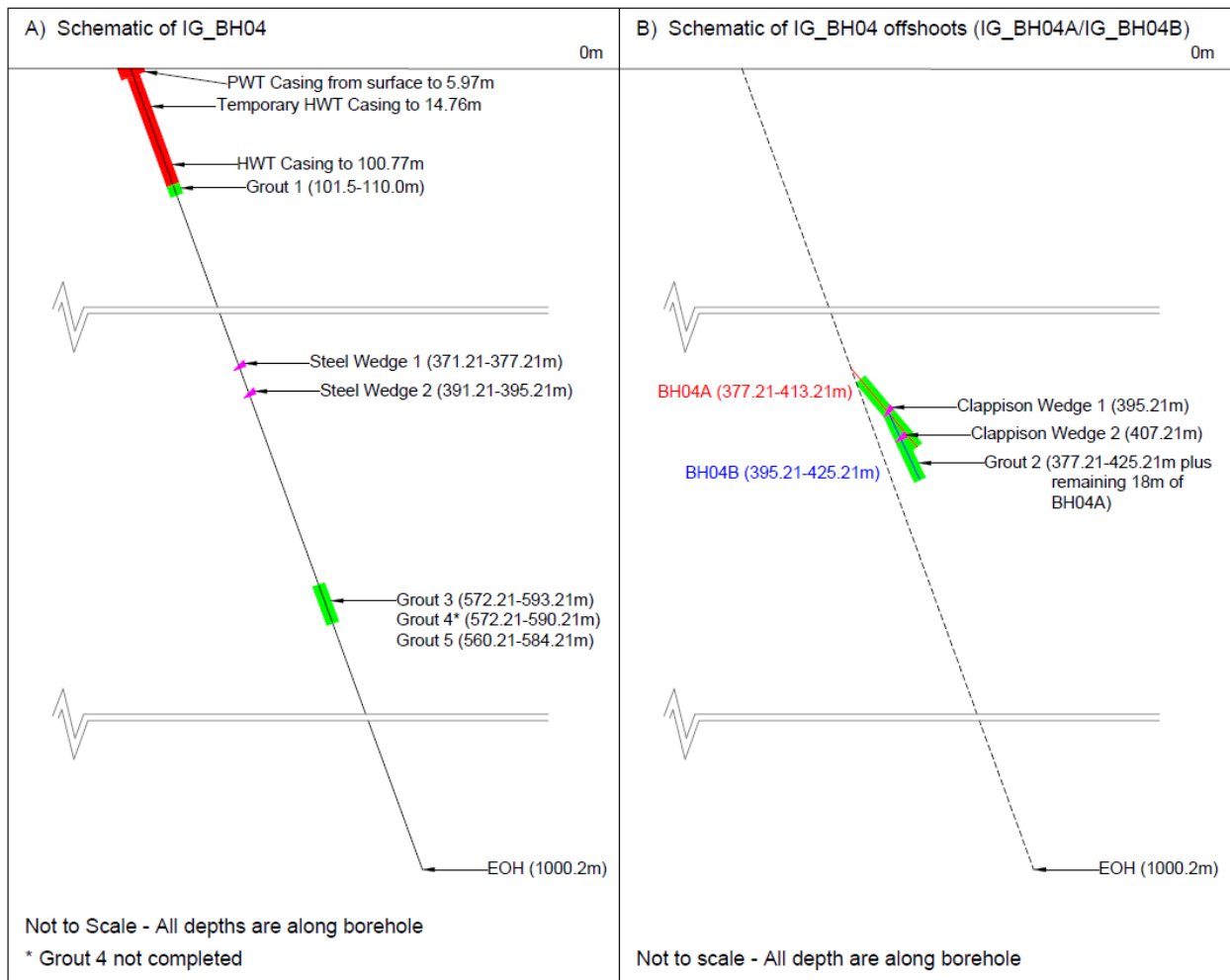


Figure 4: Schematic of Borehole IG_BH04 showing casing, wedge, and grout locations/intervals (Wood, 2021a).

Table 1: Details of Borehole Diameter for IG_BH04

Position from (m)	Position to (m)	Diameter Type	Borehole Diameter (mm)
0	5.97	Conductor (PWT) Casing and Surface (PQ) Casing	143.76
5.97	100.77	Surface (PQ) Casing	121.0
100.77	1000.20	Open Borehole (HQ size)	96

2.3.1 Borehole Deviation Analysis

Borehole IG_BH04 was planned with an inclination of -70° (equivalent tilt is 70°) towards an azimuth of 110° . Two steel wedges were installed to correct for borehole deviation during drilling (see Figure 4). Two downhole deviation surveys were conducted; one at 50 m intervals (downhole – multiple probe trips) to monitor deviation during drilling using the Reflex EZ-gyro probe, and the other at 10 m intervals at the end of drilling using the Reflex EZ-gyro (up hole – single trip; Wood, 2021a).

During the geophysical logging, four additional borehole deviation logs were continuously recorded using the onboard 3-axis magnetometer, and accelerometers within the acoustic and optical televiwer probes (Figure 5). These surveys provided continuous tilt and azimuth data at ~2 mm intervals of the probe while recording televiwer data (Golder, 2022). Due to the steel casing, the majority of the televiwer surveys were terminated at the base of the casing and are missing data from the first ~100 m of the borehole. A single televiwer survey conducted prior to installing the casing was used for this section of the borehole. Data from these surveys were mainly used to confirm and support the results of the final deviation survey using the Reflex EZ-gyro. Figure 5 presents individual azimuth and tilt profiles plotted from each televiwer run and the Reflex EZ-gyro run. The standard deviation for the azimuth and tilt profiles is calculated to show the variability amongst the different profile runs. The mean profiles for the televiwer runs are calculated and compared to interpolated profiles derived from the Reflex EZ-gyro measurements at 10 metre increments. Although the gyro survey is used for the final borehole deviation, the televiwer surveys provided an estimate of the magnitude of variability between different runs, as well as an average for comparison with the gyro survey. Overall, the standard deviation for the azimuth and tilt is shown to be less than 2 degrees and 0.5 degrees, respectively.

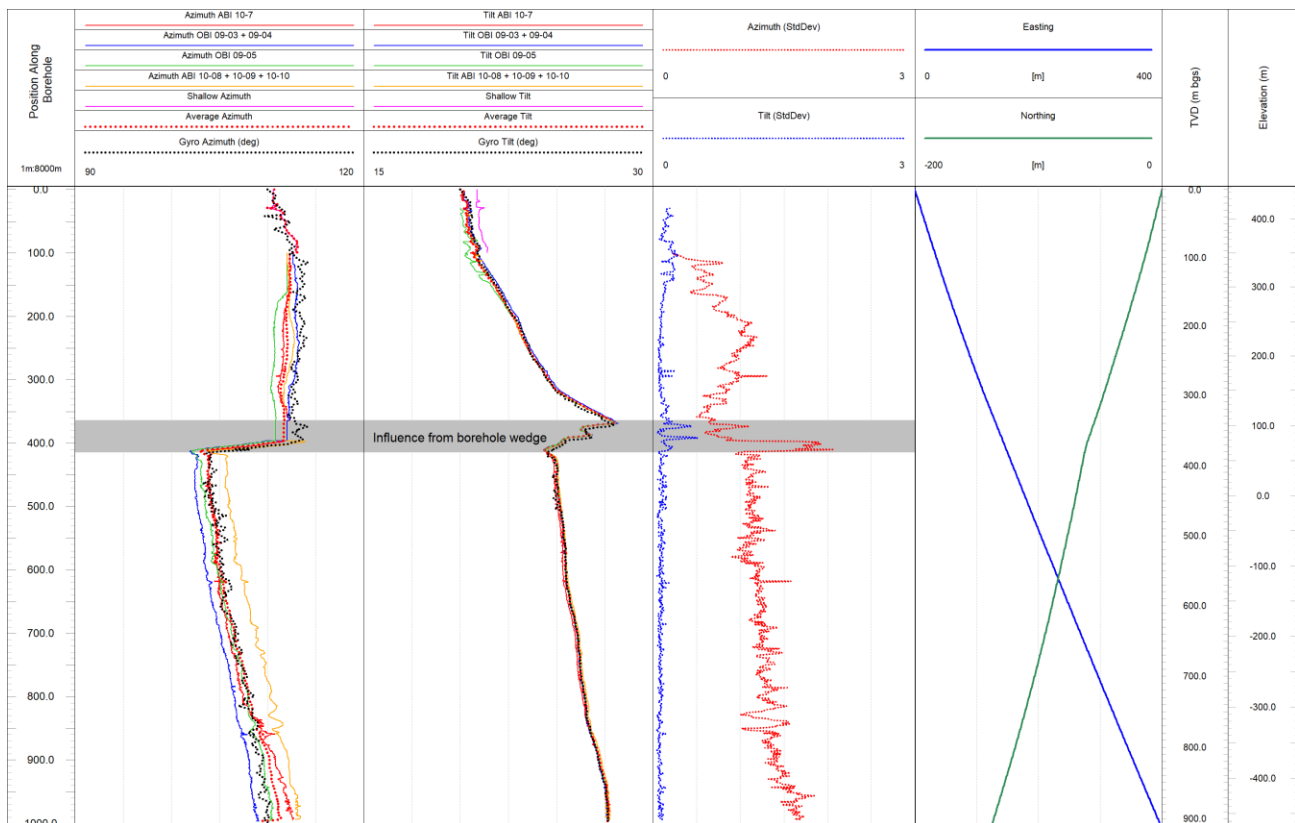


Figure 5: Compilation of borehole IG_BH04 deviation measurements. Data sets include up- and down-hole televiwers surveys and gyro surveys. Average and standard deviation between the gyro and televiwer survey measurements are presented. Final borehole path (easting, northing, TVD) is defined based on final gyro measurements from the Sprint-IQ survey.

By comparing manufacturer specifications between the Reflex EZ-gyro and the two televiwer probes, the Reflex EZ-gyro is considered more accurate. Additionally, data recorded using the Reflex EZ-gyro were performed in stationary mode, compared to the continuous mode of the televiwer probes. Despite the differences between the probes, the results indicated there is strong consistency between the average of the televiwers azimuth and tilt profiles and the Reflex EZ-gyro.

Borehole positioning was calculated using Reflex EZ-gyro survey data based on the Minimum Curvature Method, which, based on API (1985), yields the most accurate location. The three components of the location along the borehole (easting, northing and the true vertical depth (TVD)) were calculated for the Reflex EZ-gyro (10 m stations), and presented in Figure 5 and Figure 6. The borehole collar is located at Easting and Northing coordinates of 556957.25 m and 5486488.05 m, respectively, using the local UTM coordinate system (NAD83 CSRS UTM Z15N). The elevation of 443.302 masl (metres above sea level) represents the ground surface based on the CGVD2013 vertical datum. The final true vertical depth of the borehole, calculated using the measured actual orientation of the borehole and the final depth based on the retrieved core, is 906.81 mbgs. Figure 6 shows the borehole deviating 396.42 m to the East and 137.71 m to the South from the planned end location.

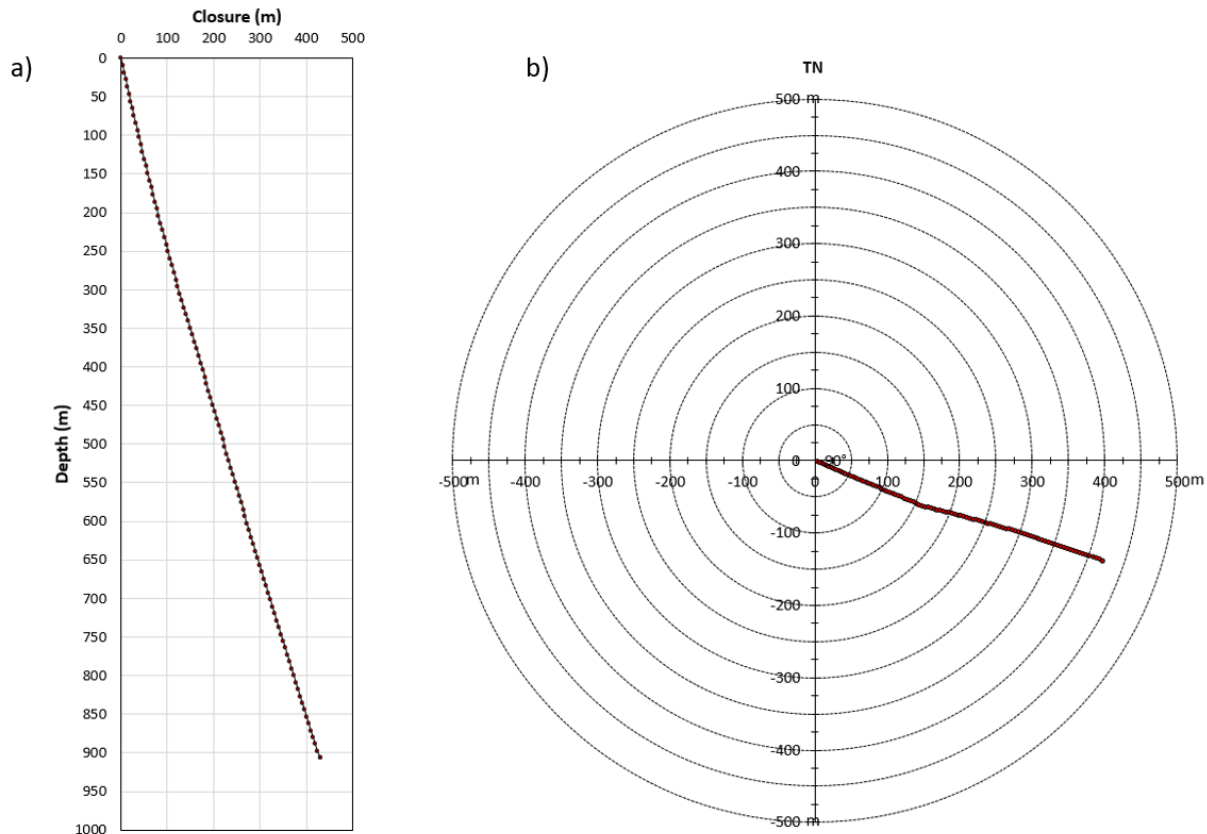


Figure 6: a) Borehole deviation presented as the total borehole closure versus true vertical depth; and b) bullseye plot showing the planned borehole trajectory (black) compared to the final Reflex EZ-gyro survey trajectory (red).

3 INTEGRATED GEOLOGICAL INTERPRETATION

The following section presents an integrated geological interpretation for IG_BH04 using the data collected during both geological core (WP03) and geophysical (WP05) logging activities, as well as relevant data from the laboratory analyses of core samples. The data sources and terminology used in order to develop the geological interpretation presented herein are described first in Section 3.1. The lithological interpretation, including final lithology and alteration logs, is presented in Sections 3.2.1 and 3.2.2, respectively, resulting in the development of an integrated rock unit model described in Section 3.2.3. A structural interpretation is presented in Section 3.2.4, resulting in a

structural unit model, described in Section 3.2.5, and a description of identified high fracture frequency intervals in Section 3.2.6.

3.1 Data Used for Geological Interpretation

The bedrock lithology, alteration and structural features were logged continuously over a total borehole length of 1000.2 m (Wood, 2021b). This initial analysis was largely based on visual inspection of the core to describe the unique rock and alteration types, as well as associated characteristics including texture, fabric and grain size. Variations in bedrock radiometric components were evaluated with the use of a handheld gamma-ray spectrometer, measured once per three metre core run, to help distinguish between the various granitoid phases encountered.

Structural features in the borehole were initially collected by geological core logging to evaluate unique structure types, mineral infillings and other associated characteristics. Recovered core was oriented during the coring process using the Reflex ACT III System and orientations of the logged structures were, in most cases, measured relative to an oriented reference line drawn along the length of the core axis. In few cases, defining an oriented reference line was not possible and structures were measured relative to an arbitrary reference line (for details see Wood, 2021b).

Following completion of the drilling and logging activities, continuous borehole geophysical logs were acquired and the results from some of these logs were used to enhance the analysis of lithology, alteration and structure (Golder, 2022). The orientations of logged structures based on arbitrary references lines were corrected through analysis of the continuous downhole optical and acoustic televiewer surveys, following the method described in Appendix C.

Geological core logging data determined to be relevant to geological interpretation include the following, as presented in the geological and geotechnical core logging (WP03) report (Wood, 2021b):

- Lithology
 - Rock Class & Rock Type
 - Rock Fabric
 - Textures (Igneous, Metamorphic)
 - Grain Size (Ground Mass, Phenocryst/Porphyroblast)
 - Defining Minerals
 - Colours & Intensity
- Alteration
 - State
 - Mineral Assemblage
- Weathering
 - State
- Structure
 - Position Along Borehole
 - Type
 - Broken/Intact/Partially Intact
 - Sub-Type
 - Infilling or Defining Mineral Details
 - Rock Wall Strength
 - Shape
 - Roughness
 - Dip and Dip Direction
 - Alpha, Beta, Gamma, and Delta Angles
 - Geological Aperture
 - Width (where applicable)

Geological aperture is an estimated measurement of the open space between two adjacent surfaces of a fracture determined visually during geological core logging, during interpretation of downhole televiewer logs, or during the integration of data from these two sources. For our purposes, geological apertures are estimated values due to the possible sources of uncertainty in how a reported aperture value relates to the true aperture of a fracture identified as broken. These uncertainties can be related to measurement inaccuracy, including where the opening is very small, where the opposing fracture planes are not parallel or fit poorly together, or due to limits in televiewer resolution. In addition, effects due to drilling or decompression may create or enhance the visible open space identified as aperture. Finally, aperture measured in core or on a borehole wall is only a local aperture that is not necessarily representative over the entire fracture.

To further enhance the bedrock lithology, alteration and structure along the length of the borehole, the following geophysical log results were determined to be most relevant:

- Optical Televiewer
- Acoustic Televiewer
- Natural Gamma
- Spectral Gamma
- Gamma-Gamma Density
- Neutron

All geophysical logging results are summarized in a separate geophysical logging report (Golder, 2022).

To further increase the lithological understanding of IG_BH04, 30 core samples were collected for whole-rock major and trace element lithogeochemical, and petrographic analysis. Representative core samples were crushed to 90% less than 2 mm, riffle split and pulverized to better than 85% passing 75 microns. The resulting sample was digested using 4 acid method and elemental composition was analyzed using inductively coupled plasma mass spectrometry (ICP-MS) (ME-MS61L method). Total carbon was analyzed using induction furnace (C-IR07 method) while loss on ignition was determined using thermogravimetric analysis (OA-GRA05 method). Polished thin sections of the subset of 30 samples were prepared at Queen's Facility for Isotope Research (QFIR), and mineral abundances were determined semi-quantitatively incorporating optical and electron microscopy methods (Scanning Electron Microscopy coupled with Mineral Liberation Analysis (MLA)). Results from these analyses are integrated below to present a final interpretation of the lithological and alteration characteristics of IG_BH04. The petrographic and lithogeochemical data are included in Appendix B.

3.1.1 Terminology

Several terms are introduced throughout this section to aid in describing the integration process. These include:

- | | |
|-----------------|--|
| Rock Unit | - A borehole length comprising a dominant rock type and/or a combination of rock types (and, if applicable, alteration and weathering types) that are considered distinct from adjacent parts of the borehole. A minimum unit thickness of five (5) m is used herein to define each rock unit. Each rock unit is uniquely labelled and can be repeated with a sub-label at different positions along a borehole, if appropriate. |
| Structural Unit | - A borehole length comprising a relatively uniform per metre fracture frequency that is distinct from adjacent parts of the borehole. Each structural unit is uniquely labelled and can be repeated with a sub-label at different positions along a borehole, if appropriate. |

- Rock Type - A rock having a unique, identifiable set of characteristics.
- High Fracture Frequency Interval - A cluster of fractures (i.e., faults, joints and/or veins) that exceeds a minimum relative fracture frequency threshold along a distinct borehole length.

3.2 Geological Results

This section presents the results from the integration of the geological core logging (WP03) and geophysical logging (WP05) datasets along with integration of the results from 30 samples selected for petrographic and lithochemical analysis (WP04D). Through the process of data integration, a total of seven distinct rock types are identified for IG_BH04 (Table 2). A final log of lithology is presented, which shows their distribution along the length of the borehole (Figure 7).

3.2.1 Lithological Interpretation

The main rock type intersected by borehole IG_BH04 is a biotite granodiorite-tonalite (Table 2). Additional rock types identified in IG_BH04 include a tonalitic end-member of the main rock type (biotite tonalite) as well as a slightly more granitic end-member of the main rock type (biotite feldspar-phyric granodiorite-tonalite)). Subordinate rock types (<2% total core recovery), include distinct metre- to sub-metre scale thick units of amphibolite, and several suites of sub-metre thick dykes of varying felsic composition (Table 2). A total of 999.53 m of core was recovered, starting at 0.67 m along borehole (Wood, 2021a). This final interpretation of the rock types encountered in IG_BH04, shown in Figure 7, presents an updated understanding relative to the information that was initially reported in the WP03 data report (Wood, 2021b).

Table 2: Summary of Rock Types Encountered in IG_BH04

Rock Type	Texture	Fabric	Grain Size (mm)	Total Logged Length (m)	% of Recovered Core
Biotite granodiorite-tonalite	Equigranular	Massive to weakly foliated	0.1-5	853.94	85.4%
Feldspar-phyric biotite granodioritetonalite	Porphyritic	Foliated to massive	<0.5*, 10** 1-3.5**	110.30	11.0%
Biotite rich tonalite	Equigranular	Massive	0.1-1	22.58	2.3%
Amphibolite	Equigranular	Massive to Foliated	<1	10.38	1.04%
Feldspar-phyric tonalite (feldspar-phyric felsic) dykes	Porphyritic	Massive	<1**, up to 7mm**	1.99	0.2%
Quartz dyke	Equigranular	Massive	5-10	0.29	<0.1%
Aplite dyke	Equigranular	Massive	<1	0.05	<0.1%

*Groundmass **Phenocrysts

A short summary of this evolution of understanding is included along with the lithological descriptions below that summarize the main characteristics of the rock types identified in IG_BH04.

Main Rock Type: Biotite granodiorite-tonalite and associated sub-units

The bedrock intersected by IG_BH04 is dominated by a medium-grained biotite granodiorite-tonalite rock where biotite is the primary mafic mineral. This rock unit and associated sub-units

represent a total of 98.34 % (986.51 m) of the recovered core. Although petrographic characteristics and mineral assemblage of biotite granodiorite-tonalite are fairly uniform throughout the core, three distinct sub-units were identified during field-level investigation, distinguished based on small variations in mineralogical assemblage, texture and grain size: 1) main biotite granodiorite-tonalite unit; 2) biotite feldspar phyric granodiorite-tonalite; 3) biotite-rich tonalite unit. The latter two sub-units, feldspar-phyric biotite granodiorite-tonalite and biotite-rich tonalite, appear to be younger intruding the main biotite granodiorite-tonalite unit. The main biotite granodiorite-tonalite unit comprises the largest section of the recovered core with 85.4 % (853.94 m) of the total core length, while the remaining feldspar-phyric biotite granodiorite-tonalite and biotite-rich tonalite comprise 11.0% (110 m) and 2.3% (22.58 m), respectively.

The general consistency in character of the recovered core with the bedrock identified on the ground surface and the rock units identified in cores recovered from adjacent boreholes, indicates that the biotite granodiorite-tonalite encountered in IG_BH04 is part of the same granodiorite-tonalite intrusive that was mapped at ground surface in the vicinity of the borehole (Golder and PGW, 2017) and logged in previous boreholes, IG_BH01 (NWMO and Golder, 2022), IG_BH02 (Parmenter et al., 2022a), and IG_BH03 (Parmenter et al., 2022b) at the Revell site.

Field-level interpretation of core lithology was aided with spot analyses of primary radioactive element contents, performed using a handheld gamma-ray spectrometer. A total of 158 measurements were collected from a hand-held gamma ray spectrometer in the biotite granodiorite-tonalite during core logging, and the results are:

- Potassium content ranges from 0 – 0.8 % with an average of 0.28 %
- Uranium content ranges from 0 – 5.9 parts per million (ppm) with an average of 0.53 ppm
- Thorium content ranges from 0 – 3.5 ppm with an average of 1.24 ppm

The low potassium content determined using hand-held gamma ray spectrometer is consistent with the field-level observation of the relatively low abundance of K feldspar in the main granodiorite-tonalite unit.

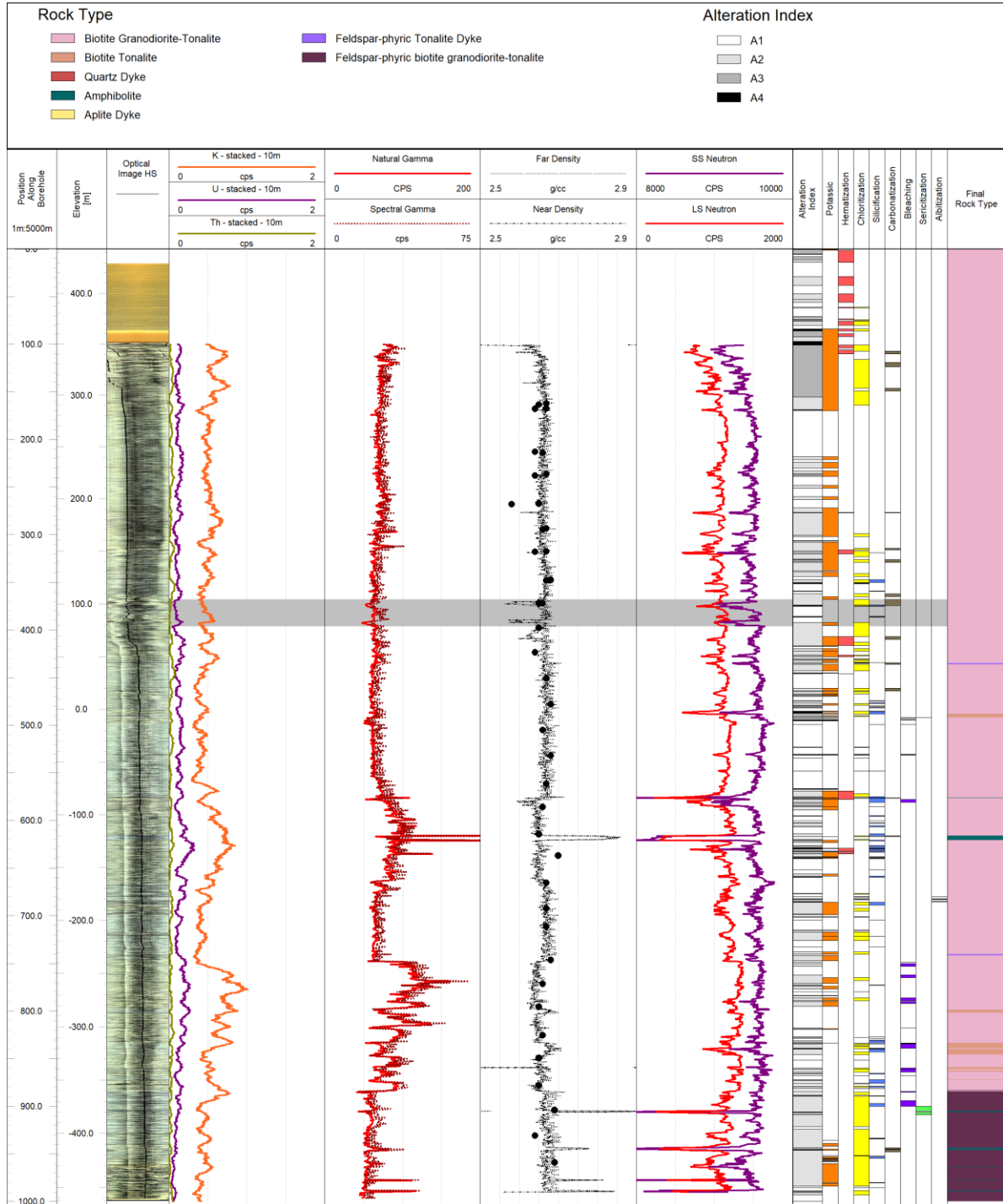


Figure 7: Input datasets used to derive a final lithology log. From left: optical televiewer log, four suites of continuous geophysical logs that aid in distinction of rock types, logged alteration (by type), and final lithology log. Due to the low spectral gamma counts, K, U and Th were evaluated using a 10 m window, resulting in a smoothing of their profiles. Note also that due to low spectral gamma counts, K, U and Th contents could not be reliably reported in % or ppm. Grey band represents the zone of influence of steel wedge.

Lithogeochemical and petrographic analyses were conducted on selected representative samples, complementing the field-level lithological classification. Petrographic characterization of the main rock units intersected by IG_BH04 are in close agreement with field-level observations. Semi-quantitative determination of mineral abundances in petrographic cross sections using optical microscopy and electron microscopy coupled with automated mineral identification using MLA shows that plagioclase, quartz and alkali feldspar are the main rock forming minerals. The main mafic mineral is biotite while the main accessory and trace mineral phases are titanite, apatite, rutile, zircon, monazite and calcite. Chlorite and muscovite are present as secondary replacement of biotite and plagioclase, respectively. Epidote is a common mineral, frequently associated with biotite (larger 100-300 micron, subhedral crystals) or muscovite (25-100 micron, subhedral crystals) in the core of plagioclase. It is possible that larger epidote crystals are primary magmatic, while smaller crystals may be of metamorphic origin (redistribution of K and Ca within calcium rich plagioclase).

The modal abundance of main minerals corresponds to tonalite and granodiorite on a Quartz, Alkali feldspar, Plagioclase (QAP) ternary diagram (Figure 8) with the exception of one sample from feldspar-phyric biotite granodiorite-tonalite subunit which can be classified as granite due to relatively higher K-feldspar abundance. The modal mineral composition of all samples is presented in Appendix B.

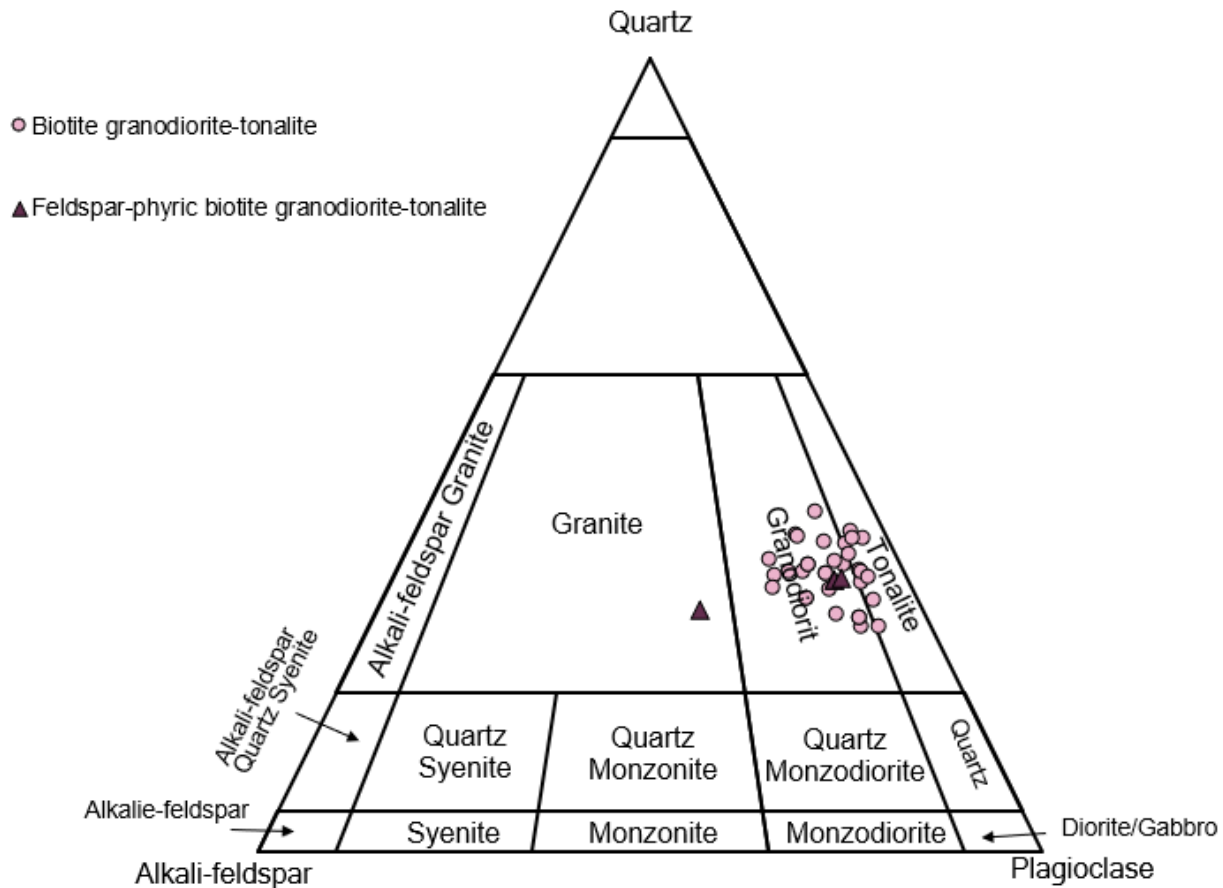


Figure 8: Classification/nomenclature of felsic granitoid phases according to the normalized modal mineral content (Quartz + Alkali-feldspar + Plagioclase = 100 Vol%) as determined from investigation of 30 samples. Average modal mineralogy for each sample was determined semi-quantitatively using polished thin sections and plotted on a simplified ternary Streckeisen diagram after Le Bas and Streckeisen (1991).

Using chemical equivalent of the QAP plot, the P–Q ('nomenclature') diagram developed by Debon and Le Fort (1983), corroborates the modal classification of biotite granodiorite-tonalite and associated subunits. The whole rock composition of IG_BH04 samples straddles tonalite and granodiorite fields in P-Q diagram (Figure 9) reflecting abundance of quartz (high Q [$Si/3 - (Na + K + 2 \times Ca/3)$]) and relatively lower proportion of K-feldspar compared to plagioclase (low P [$K - (Na + Ca)$]).

The main biotite granodiorite-tonalite unit and associated sub-units are silica rich ($SiO_2 > 70\%$) and peraluminous (Aluminium Saturation index $Al/Ca - 1.67P + Na + K = 1.15$ indicating that Al abundance exceeds alkalis), with high Na_2O content (average 4.45%) and low K_2O/Na_2O ratio (< 0.5 in all unit sub-types). The content of the ferromagnesian elements is low ($Fe_2O_3^* + MgO + MnO + TiO_2 \leq 3.63\%$, average 2.78%; $Fe_2O_3^* = \text{total Fe expressed as } Fe_2O_3$). Average elemental Mg, Ni and Cr contents are very low at 0.29%, 2.3 ppm and 9.6 ppm, respectively.

Petrographic description of biotite granodiorite-tonalite subtypes

The main biotite granodiorite-tonalite unit is light to medium white-grey, equigranular, phaneritic and medium-grained (1-5.0 mm) (Figure 10). Its main mineral phases are quartz, plagioclase,

potassium (alkali) feldspar, with modal abundance of 44-57 %, 24-37 % and 3-17 %, respectively, as determined with MLA petrographic analysis of thin sections. The biotite is the primary mafic mineral, comprising 2.9-7.9 modal % with average abundance of 5.4 modal % (n=33) as determined semi-quantitatively using the MLA technique. The biotite granodiorite-tonalite is predominantly massive although a weak biotite-defined foliation is locally apparent below 780m core depth (WP3 report, Wood 2021). There were 30 biotite granodiorite-tonalite samples from IG_BH04 sent for optical petrography (27 from main biotite tonalite unit and 3 from feldspar-phyric biotite granodiorite-tonalite), and they plot across the tonalite to granodiorite field on the QAP diagram (after Le Bas and Streckeisen, 1991; Figure 8). The same group of 30 samples were sent for bulk lithochemical analysis and the major oxides demonstrate a felsic composition (Table 3) and plot across the tonalite to granodiorite fields on the plutonic rock classification diagram (after Debon and Le Fort, 1983; Figure 9).

Table 3: Summary average of major oxides in the rock types of IG_BH04. Note that only 3 main rock types broadly classified as biotite granodiorite-tonalite were analyzed.

Rock Type	Major Oxide Composition (average, %)									
	SiO ₂	Al ₂ O ₃	Fe ₂ O ₃	MnO	MgO	CaO	Na ₂ O	K ₂ O	TiO ₂	P ₂ O ₅
Biotite granodiorite-tonalite	74.31	13.50	1.98	0.03	0.46	2.45	4.44	2.13	0.23	0.07
Feldspar-phyric Biotite granodiorite-Tonalite	69.74	14.08	2.46	0.03	0.66	2.87	4.54	1.99	0.31	0.07

The porphyritic sub-type of biotite granodiorite-tonalite was identified in nine intervals during core logging. These occurrences were logged as feldspar-phyric tonalite and comprised most of the core between 883 m depth and the borehole's end. The distinguishing feature of this unit is the presence of subhedral, white, up to 1 cm plagioclase porphyroblasts and finer mafic grain size (Figure 12). Three samples corresponding to this interval were sent for further petrographic and lithochemical analysis. The modal mineral abundance of three representative feldspar-phyric tonalite samples is similar to the rest of biotite granodiorite-tonalite with 28-30 % quartz, 7-26% alkali-feldspar, and 38-50 % plagioclase. The biotite is the main mafic mineral, comprising 3.6-6.4 modal % with average abundance of 5.3 modal % (4 thin sections from 3 core samples). One core sample (IG_BH04_MG028) is compositionally within the granite field on QAP diagram (K-feldspar content 26 %), while the remaining two may be classified as granodiorites. Note, however, that in P-Q classification IG_BH04_MG028 sample would be classified as tonalite.

Field-level observations identified several biotite-rich intervals with up to 20-25 % biotite (macroscopic identification). Based on field-level interpretation, these intervals were designated as biotite-rich tonalite (Table 2; WP3 report Wood 2021), distinguished from the main granodiorite-tonalite unit by finer grain size (fine-grained 0.1-1 mm) and darker colour (medium to dark grey). The contact between biotite granodiorite-tonalite and biotite tonalite unit varied between sharp and gradational. The biotite tonalite unit exhibits an equigranular texture and massive fabric.

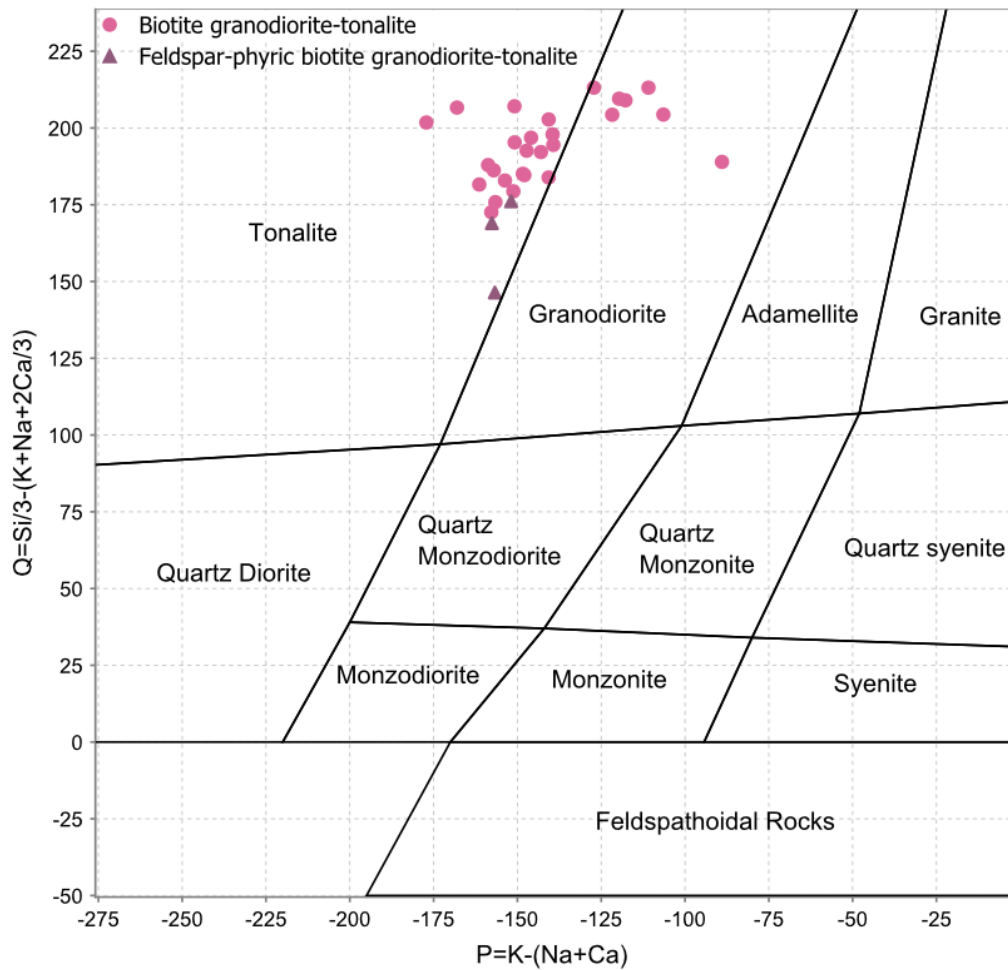


Figure 9: Plutonic Rock Classification (Debon and Le Fort, 1983). Diagram axes correspond to proportions of K-feldspar and plagioclase to quartz. P is calculated from $(\text{K} - (\text{Na} + \text{Ca}))$ and Q is calculated from $((\text{Si}/3) - (\text{K} + \text{Na} + (2 \cdot \text{Ca})/3))$. Parameters calculated as oxide percentages converted to millications.

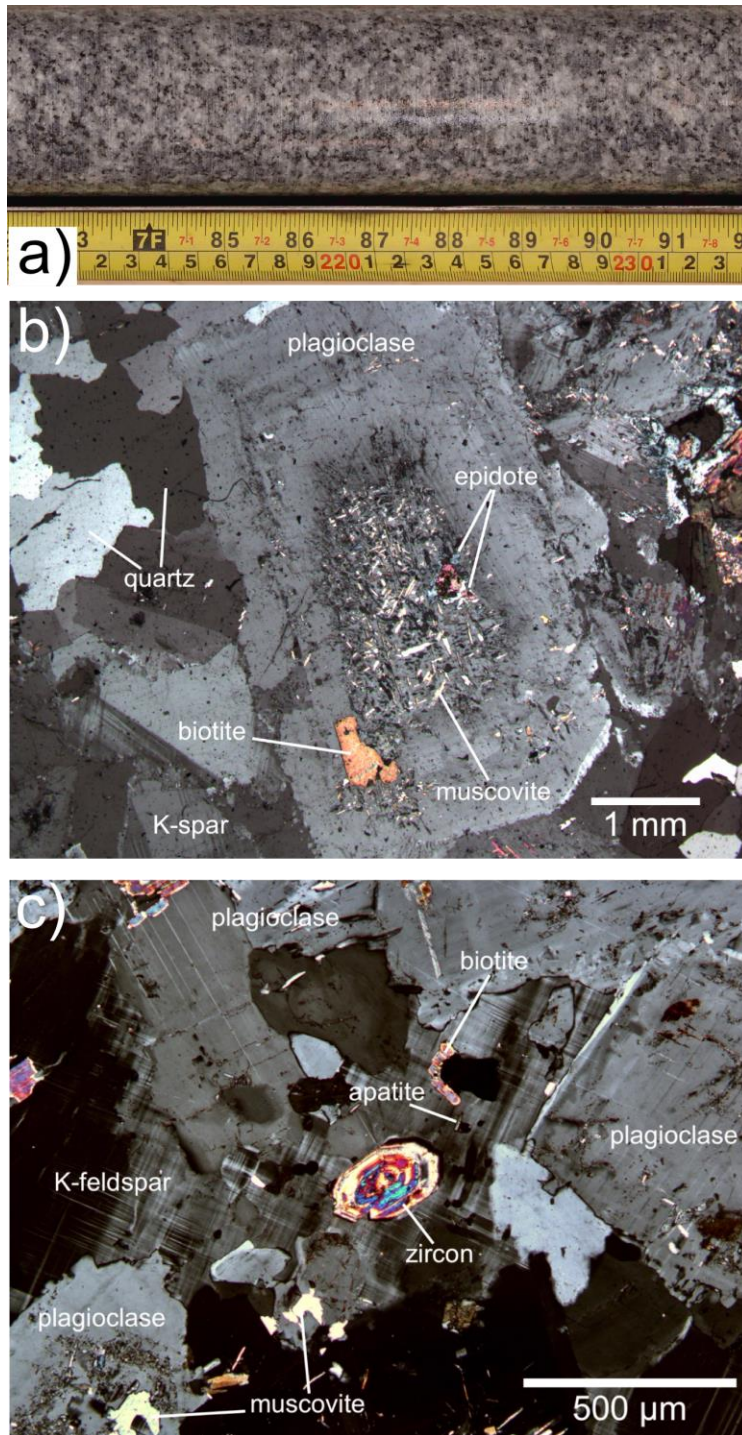


Figure 10: Representative example of biotite granodiorite-tonalite (sample IG_BH04_MG010). a) Core sample photograph. b) Photomicrograph showing a coarse zoned subhedral plagioclase crystal with abundant muscovite and some epidote in the core of the crystal; sample 04-MG010, cross-polarized light. c) Photomicrograph showing a zoned euhedral zircon and a diminutive subhedral apatite surrounded by alkali feldspar (K-feldspar) and plagioclase; sample IG_BH04_MG010, cross-polarized light. Sericite (white mica) alteration can be seen in cores of plagioclase crystals; crossed polarizers transmitted light.

Subordinate Rock Types

In IG_BH04, the subordinate rock types encountered (amphibolite, feldspar-phyric tonalite dykes, quartz dykes, and aplite dykes) represent a combined <2 % (13.02 m) of the recovered core (Table 2).

Amphibolite: IG_BH04 intercepted a small group of melanocratic intervals tentatively described during initial field interpretation as amphibolite. It should be noted that amphibolite is a field term designation for this unit and should not be construed to designate a metamorphic unit of amphibolite facies. Preliminary petrographic and lithogeochemical investigation of similar melanocratic units in adjacent boreholes IG_BH01, IG_BH02, and IG_BH03 reveals that units identified as amphibolite represent a complex and variable mineralogical assemblage including tremolite/actinolite (+/- hornblende), plagioclase, biotite, quartz, chlorite and epidote, broadly corresponding to dioritic composition. Macroscopically amphibolites are dark grey-green, equigranular, and usually fine-grained (<1 mm; Figure 13a). The mineral assemblages include plagioclase (albite), tremolite/actinolite, biotite, chlorite, and epidote, +/- titanite, calcite, quartz, and iron oxides. Ten occurrences of amphibolite were logged in IG_BH04, accounting for 10.38 m (1 %) of the total recovered core (Table 2). The amphibolites range in width from 0.07 m to 2.83 m. All amphibolite occurrences were observed below 535 m along borehole (Figure 7). Out of ten occurrences one was logged as "mafic" unit (575.78-576.34 m), and two units between 616-621 m were logged as metamorphic. The remaining amphibolite occurrences were logged as amphibolite dykes and occur below 905.00 m. During the integration of WP03 and WP05 data, a decision was taken to identify all of these subordinate rocks as amphibolite. The contact zones between amphibolite units and biotite granodiorite-tonalite are described as sharp, and commonly exhibit evidence of ductile to brittle-ductile strain localization. In geophysical logs, amphibolite occurrences express distinct increases in gamma density values and decreases in neutron values relative to the host biotite granodiorite-tonalite (Figure 7).

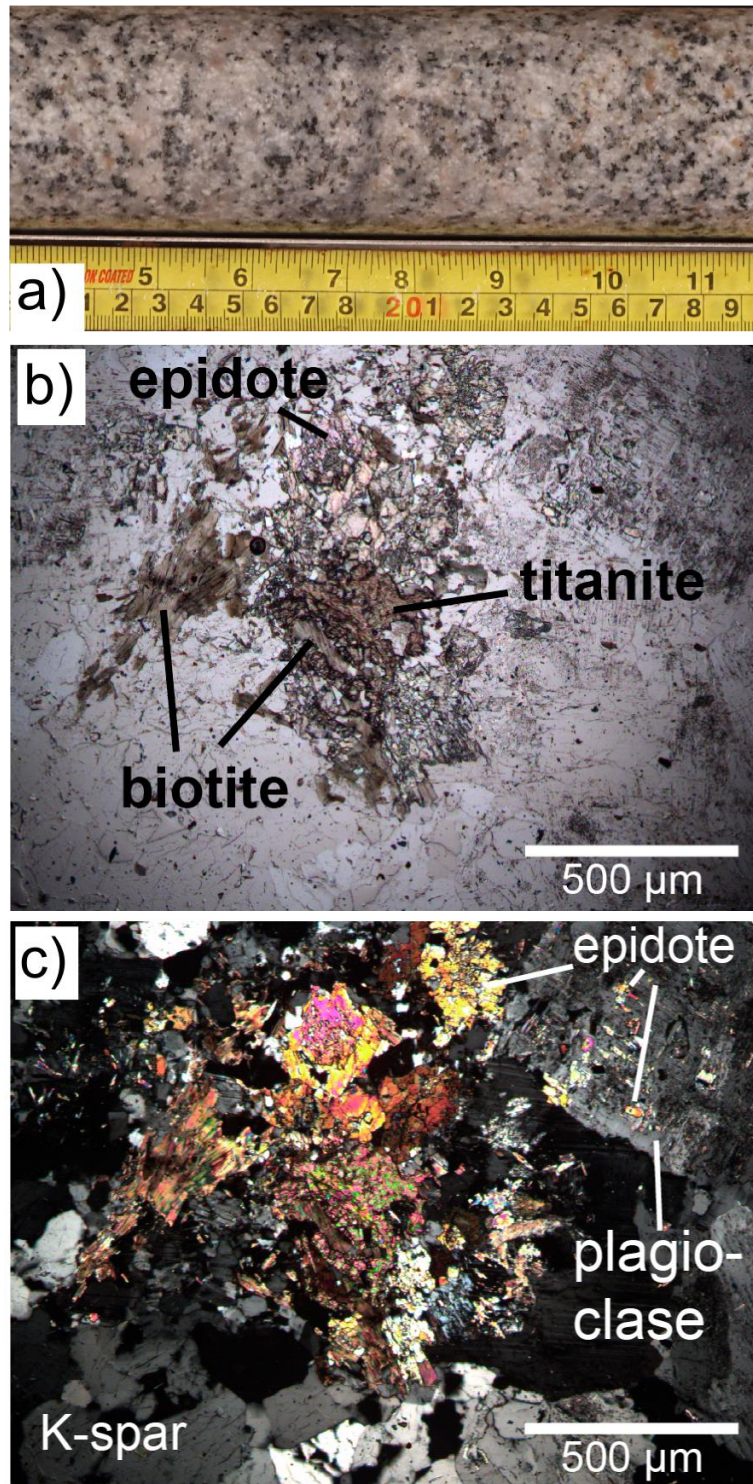


Figure 11: Representative example of biotite granodiorite-tonalite (sample IG_BH04_MG016). a) Core sample photograph. b) Photomicrograph of thin section showing titanite associated with biotite and epidote in sample 04-MG016, plane polarized light; c) Same view as Figure 10b, cross-polarized light.

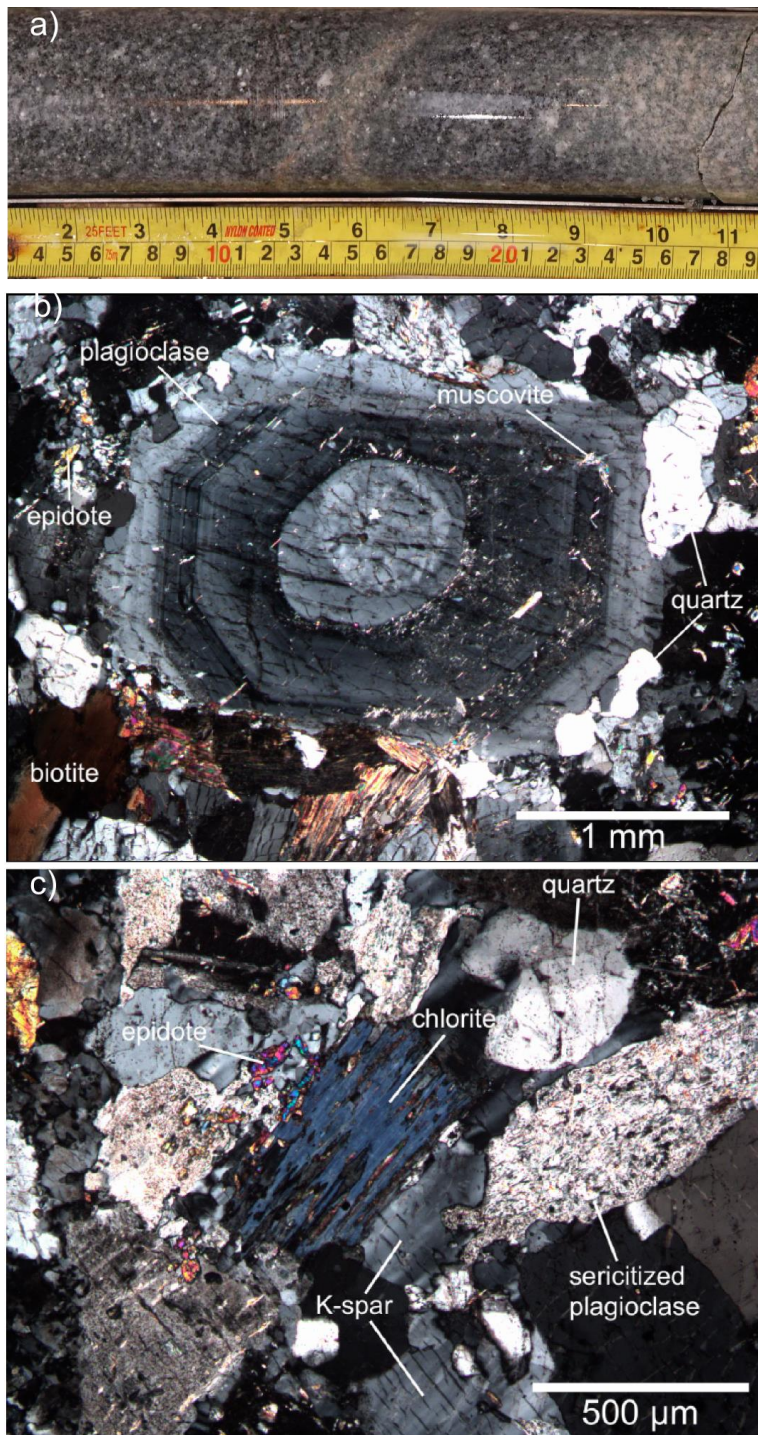


Figure 12: Representative examples of a granodiorite-tonalite (feldspar-phyric tonalite subunit) (IG_BH04_MG030). a) Core sample photograph. b) Photomicrograph showing a coarse zoned subhedral plagioclase porphyroblast with inclusions of muscovite; sample 04-MG030, cross-polarized light. c) Photomicrograph showing chlorite with Berlin blue birefringence that replaced a biotite grain; plagioclase (on the of central chlorite grain) is extensively 'sericitized' (replaced by fine muscovite); sample 04-MG030, cross-polarized light.

Feldspar-phyric tonalite dykes: Feldspar-phyric tonalite (logged as feldspar-phyric felsic) dykes intersect the main biotite granodiorite-tonalite in two intervals: 434.78–435.78 m and 740.55–741.54 m (Figure 7). The two intervals combined have a total length of 1.99 m, representing less than 1% of the recovered core. Based on field-level observation, these dykes are medium to dark grey with a fine-grained matrix composed primarily of quartz and plagioclase with 3–5% medium-grained feldspar phenocrysts up to 7 mm wide (Figure 13b). Contacts with the country rock are sharp, intact, with no chilled margin features, and commonly exhibit evidence of ductile strain localization.

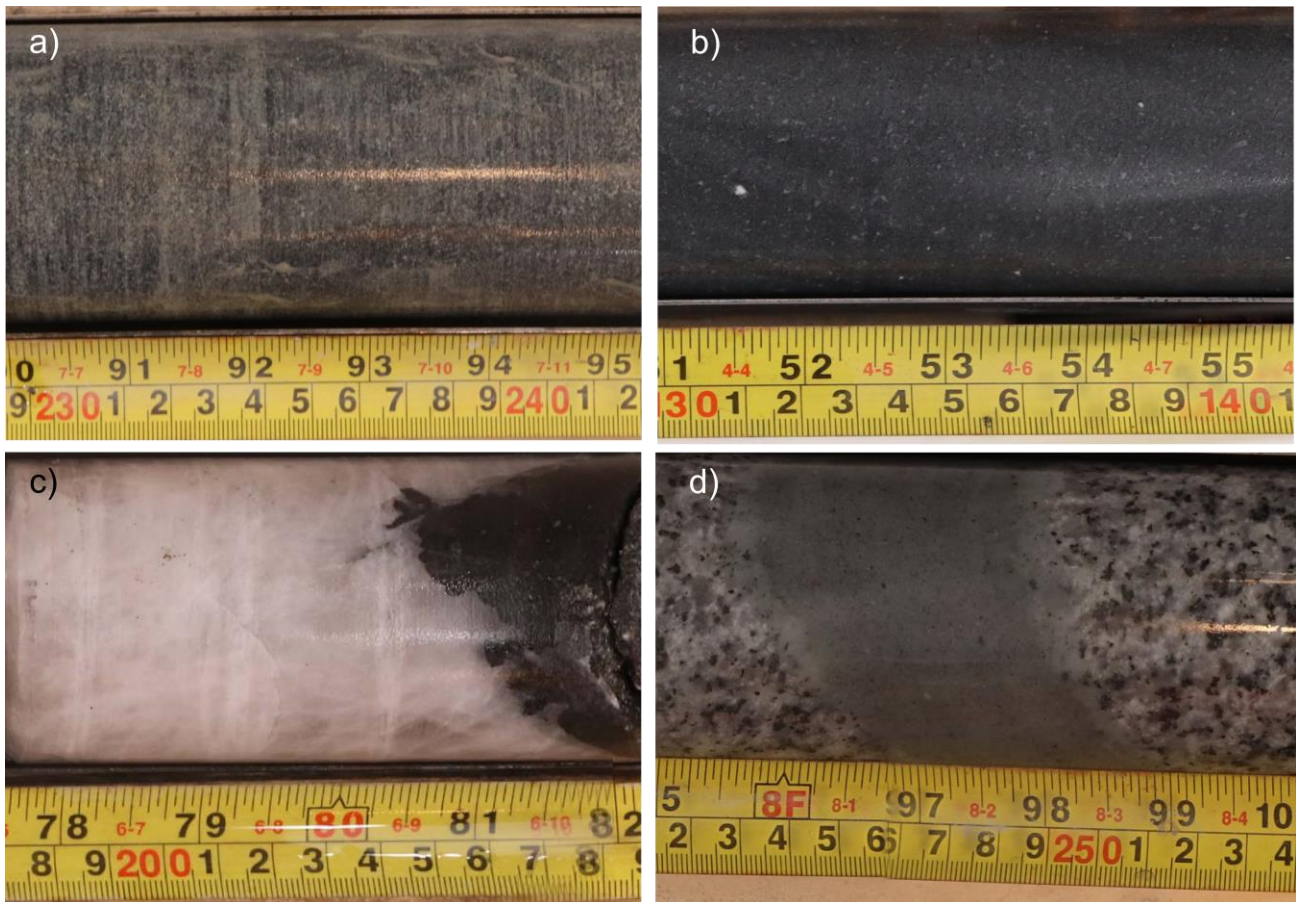


Figure 13: Representative examples of subordinate rock types: a) Amphibolite (619.21- 619.34 m), b) Feldspar-phyric tonalite dyke (435.50-435.61 m), c) Quartz dyke (989.13-989.18 m), d) Aplite dyke (761.60-761.65 m)

Quartz dyke: One quartz dyke occurrence (width of 0.29 m). This quartz-rich unit is milky white to smoky grey, massive, medium-grained (5-10 mm), and composed almost entirely of quartz with minor occurrences of the host rock-infilling fractures (Figure 13c). The contact zones between this dyke and the surrounding bedrock is described as intact, sharp and irregular.

Aplite dyke: One aplite dyke with a width of 0.05 m was logged at 761.60 m. The aplite dyke is light grey, equigranular, and fine-grained (<1 mm) to aphanitic. Based on field-level mineral identification, quartz and alkali feldspar are the main mineral phases, with minor biotite as the main mafic mineral (Figure 13d). The dyke contacts with the country rock are intact and sharp, with a slight silicified alteration halo of approximately 1 cm (Figure 13d).

Summary of rare-earth element data

All samples show high contents of light REE (LREE, Sum LREE_{average}=63.01) and low concentrations of heavy REE (HREE, Sum HREE_{average}=1.71). Chondrite-normalized rare-earth element (REE) plots of rare-earth element (REE) data, collected as part of the litho geochemistry analysis, are plotted for all samples (Figure 14). The chondrite-normalized pattern of the three main units (biotite granodiorite-tonalite, biotite tonalite, and feldspar-phyric biotite granodiorite-tonalite) are steeply fractionated [average (La/Yb)₃₀ = 62.5; median (La/Yb)₃₀ = 73.2] with significant depletion of heavy rare-earth elements [HREE; average (Gd/Er)₃₀ = 3.3, median (Gd/Er)₃₀ = 3.6]. REE patterns of all samples lack Eu anomaly (average Eu/Eu* = 1.10, calculation after Taylor and McLennan, 1985).

IG_BH04 samples REE composition is similar to other Neoproterozoic low-HREE granitoids of the tonalite-trondhjemite-granodiorite (TTG) suite, which carry a basaltic crust signature (Halla, 2018 and references therein). The origin of low-HREE TTGs has been linked to high-pressure melting of the deep lower part of oceanic crust during subduction (Halla et al., 2009). Notable depletion of HREE reflects retention in residual garnets during partial melting of source basalts (Halla et al., 2009).

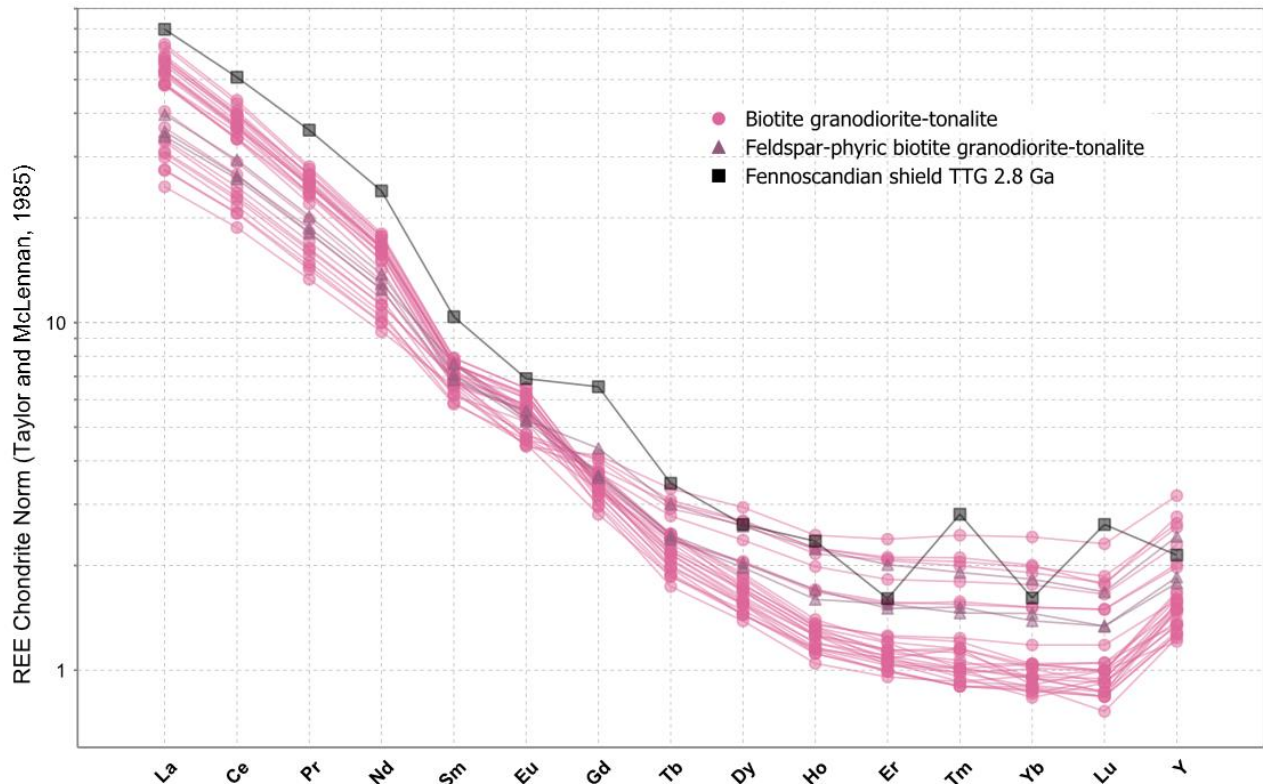


Figure 14: Chondrite-normalized rare-earth element (REE) plot (after Taylor and McLennan, 1985) of rock types from IG_BH04 and a representative average of 2.8 Ga low-heavy REE (HREE) tonalite-trondhjemite-granodiorite (TTG) from the Fennoscandian shield (black squares; Halla, 2018). Y-axis shows concentrations (expressed as logarithm to the base 10 of the value) of REE (x-axis, by atomic number) in IG_BH04 samples normalized to a reference Chondrite standard. REE patterns of biotite granodiorite-tonalite and feldspar-phyrlic biotite granodiorite-tonalite demonstrate steep fractionation and significant depletion of HREE.

Summary of geophysical characteristics of the identified rock types

A suite of geophysical logs, including natural gamma, spectral gamma, gamma-gamma density and neutron are widely used both for identifying rock types and delineating contacts (e.g., Keys, 1997). Such subtle boundaries could reflect sharp or gradational changes in mineralogical composition, such that any variability not observed in the initial stage of geological core logging could be identified by assessment in comparison with these geophysical logs (Figure 15 and Figure 16). The discussion below describes each of these geophysical logs to characterize the bedrock, in general, and applies this information to evaluate the specific rock types encountered in the borehole. A summary table of mean geophysical responses for each logged rock type is included in Table 4.

Table 4: Mean geophysical response values for each logged rock type.

Rock Type (N=number of points)	Natural Gamma (cps)	Neutron* (cps)	Density** (g/cm ³)	K (cps)	Th (cps)	U (cps)
<i>Amphibolite (N=204)</i>	97.92	8069.76	2.81	0.54	0.04	0.14
<i>Aplite dyke (N=1)</i>	117.90	9706.07	2.64	0.80	0.02	0.18
<i>Biotite granodiorite-tonalite (N=15096)</i>	73.88	9493.54	2.66	0.53	0.03	0.14
<i>Biotite rich tonalite (N=451)</i>	70.69	9533.08	2.67	0.58	0.03	0.16
<i>Feldspar-phyric tonalite dyke (N=39)</i>	63.83	9338.13	2.69	0.44	0.04	0.13
<i>Feldspar-phyric biotitegranodiorite-tonalite (N=2193)</i>	55.57	9451.58	2.67	0.46	0.02	0.09
<i>Quartz dyke (N=6)</i>	91.64	8532.38	2.76	0.36	0.04	0.09

* long spacing neutron sensor values are presented.

** mean gamma-gamma density values, from near and far measurements, are presented.

The natural gamma log quantifies the amount of radioactive isotopes occurring naturally within the bedrock. However, it does not identify the radioisotopes responsible. Results from the spectral gamma log can be useful to differentiate the relative amount of potassium, uranium and thorium (herein presented in counts per second, cps). Although data from natural gamma and spectral gamma logs do not correlate directly to specific rock types, their relative variabilities along the length of the borehole are used to assess mineralogical variation that indicate the change from one rock type to the next.

Data measured from both the gamma-gamma density and neutron logs were used to quantify petrophysical properties of the bedrock (e.g., bulk rock density), and were correlated to specific rock types. Measurement of these logs are, however, sensitive to variations in pore space in the bedrock. The gamma-gamma log measures the backscatter and attenuation of gamma photons emitted at a near and far sensors from the logging gamma source where the measured response is converted to bulk density through calibration prior to recording data.

The neutron log uses a neutron source and detector to measure the relative neutron counts in the bedrock along the borehole wall. Most neutron interactions can be inversely related to hydrogen ion concentrations in the bedrock, such that responses can be generally related to water present within the pores in the bedrock (e.g., Daniels et al., 1984; Keys, 1997). Considering the generally intact state of crystalline rocks in BH04 it can be inferred that neutron counts are largely reflect the relative changes in bedrock mineralogy, primarily the presence of hydrous minerals (e.g., micas and amphiboles).

Electrical resistivity, single point resistance, and induction logs can be used as a diagnostic tool to interpret rock types and contacts; however, in this borehole there is no indication of changes associated with varying rock types. Evidence suggests that discrete variations in electrical resistivity or single point resistance may be largely correlated to the presence of fractures (e.g., fracture frequency) and particularly fractures with measured geological aperture or secondary porosity (e.g., fracture porosity).

Description of borehole geophysical data acquisition and processing are detailed in Golder (2022). For this report, the data are analyzed at a uniform spacing of 5 cm along the length of the borehole

from bottom of casing to end of borehole. Continuously measured natural gamma, spectral gamma, neutron (long-spacing sensor), and density responses are presented in Figure 7 and were used to highlight variations in physical bedrock properties along the borehole. By comparing the laboratory reported wet density values from 40 samples to the continuous geophysical density logs, it was determined that the geophysical logs, on average, overestimated the density values for the borehole by 3.8 percent. A correction factor was determined by averaging the differences between each laboratory measurement and the field measurement at the corresponding position, for both the near and far density logs (see Appendix C). The geophysical density logs were corrected using the correction factor to reduce the geophysical log values (i.e., $DENSITY_{corrected} = DENSITY_{measured} / 1.038$), making the profile consistent with the measured laboratory values. A similar correction factor has been applied to the geophysical logs for boreholes IG_BH01, IG_BH02 and IG_BH03, each of which required a correction factor of approximately 3 to 5 percent. For this analysis, a mean density profile was calculated based on the average of the corrected near and far density values along the length of the borehole.

The biotite granodiorite-tonalite phase represents the majority of the measured geophysical response values (see Figure 7 and Table 4) and can be attributed as the base-line values for the bedrock. Any deviations away from this response tend to be associated with various factors, including changes in rock type and associated mineralogy, presence of fractures and associated infillings, and/or presence of alteration types and associated intensities.

The distributions of natural gamma, density, and neutron responses present observable differences in the geophysical responses between each rock type. As shown Figure 15, a suite of felsic dykes (aplite, feldspar-phyric tonalite) present a subtle increase in natural gamma relative to the biotite granodiorite-tonalite. Conversely, the amphibolite, feldspar-phyric tonalite dykes, aphanitic tonalite dykes, and quartz dykes present a slight reduction in natural gamma response. Overall, natural gamma, neutron, and density distributions shown in Figure 15 display considerable similarities between all felsic rocks, with the exception of the quartz dykes. The quartz dykes show a slight reduction in measured natural gamma radiation and a significant reduction in neutron counts with respect to the other felsic rock types (Table 4 and Figure 15).

The amphibolite occurrences in the borehole present a characteristic reduction in neutron counts and an increase in bulk density relative to the biotite granodiorite-tonalite. The increased bulk density of amphibolites can be directly related to the presence of tremolite-actinolite which is a relatively dense mineral, especially in comparison to the main mineral phases comprising the felsic units (i.e., plagioclase, alkali feldspar, and quartz). The reduced neutron counts of the amphibolites can possibly be associated with an increase in apparent primary porosity. However, it is more likely related to secondary (e.g., fracture) porosity or the hydrous nature of their mineral assemblage (e.g., chlorite, amphibole).

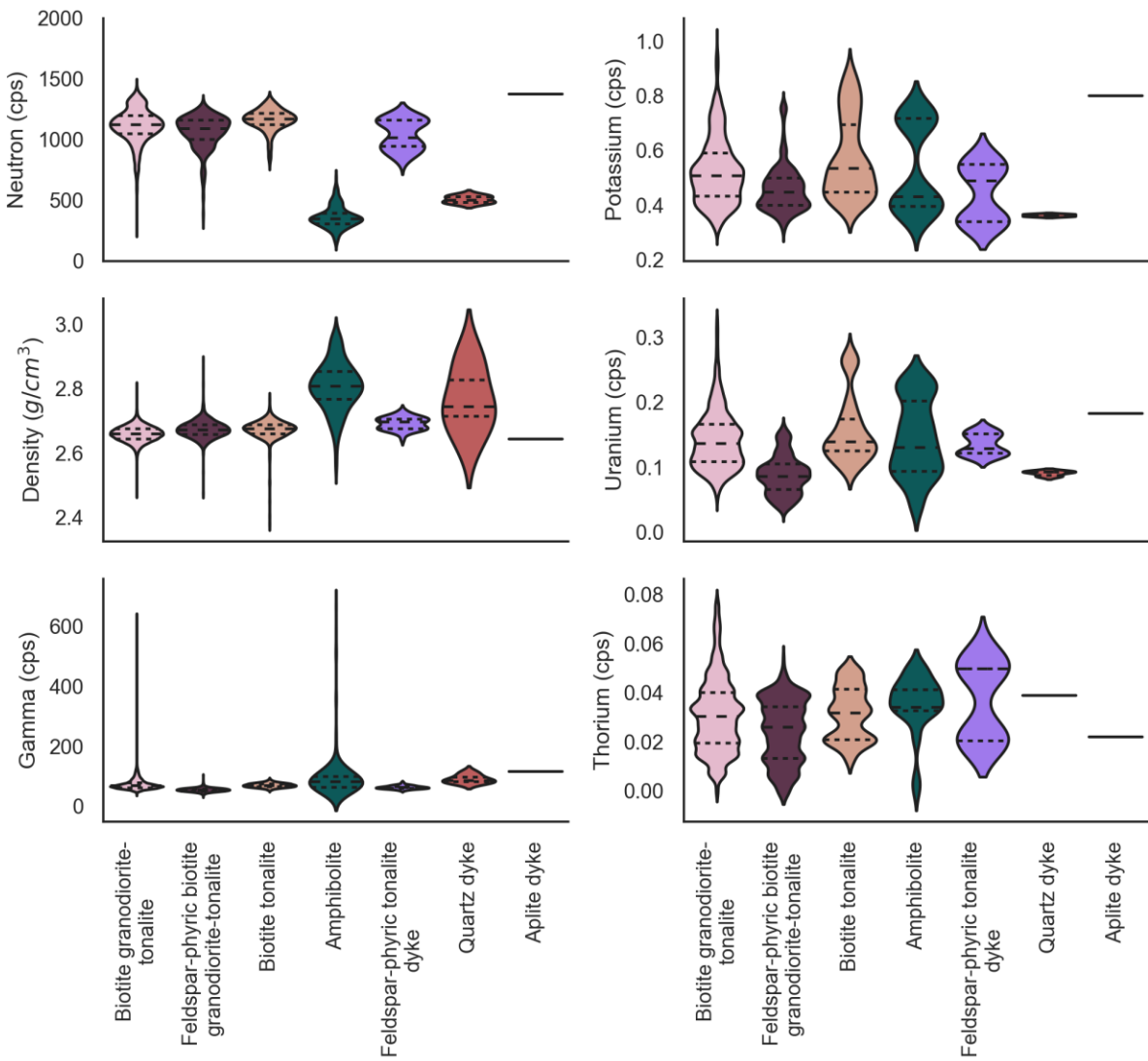


Figure 15: Violin plots show the distribution of geophysical log responses associated with the logged rock types. Each violin shows the distribution of the data values with the median (thick dashed line), and quartiles (thin dashed lines) marked. Rock types are ordered based on total data counts from left to right in each graph.

The distribution of neutron, density, natural gamma and potassium values are presented in Figure 15 and Figure 16 showing the cross-correlation between the selected geophysical log data and corresponding rock types. Scattered data points are plotted for the entire length of the borehole at 5 cm intervals. The larger data points represent mean centroid values of the geophysical responses and the error bars represent the standard deviation.

Overall, the distributions of biotite granodiorite-tonalite, biotite tonalite, and feldspar-phyric tonalite dykes largely overlap making distinguishing between them using geophysical comparison plots alone difficult. However, the quartz dykes are characterized by a reduced neutron count and a slight increase in bulk density values which is apparent in Figure 16. In addition, the amphibolites are uniquely characterized by low neutron counts, and high bulk densities and can be distinguished from the other felsic units in all cross-plots (Figure 15 and Figure 16). Density values for the amphibolites typically exceed 2.75 g/cm³ with a mean of 2.81 g/cm³.

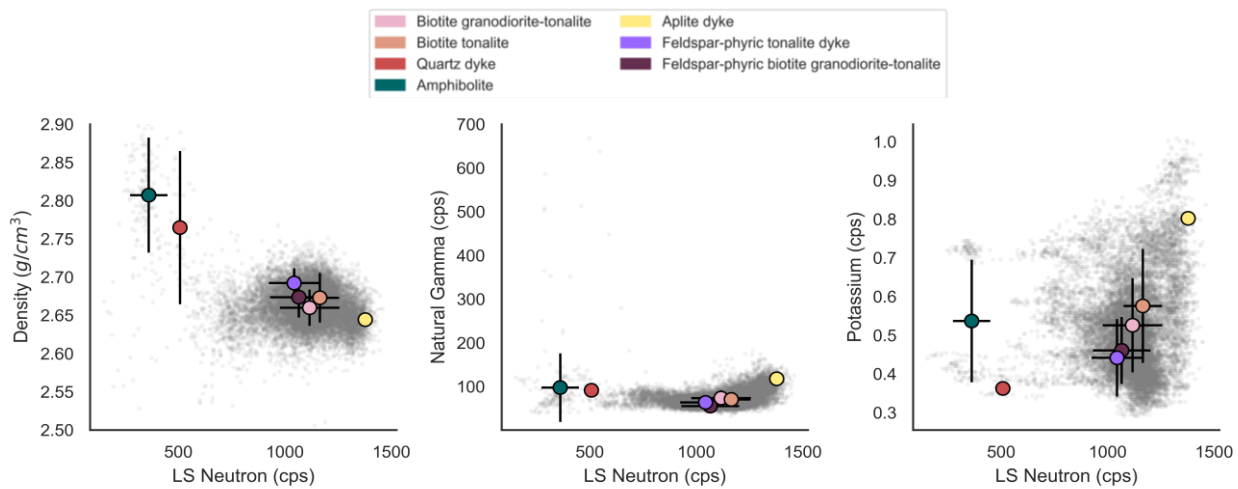


Figure 16: Cross plots showing correlations between neutron, density, natural gamma and potassium count values of all rock types encountered in IG_BH04. Colored points represent mean values of the geophysical responses and the error bars represent standard deviation

3.2.2 Alteration Interpretation

Eight alteration types were logged in IG_BH04 (Table 5 and Figure 17). The alteration types logged in order of prevalence were: potassic alteration, chloritization, hematization, silicification, carbonatization, bleaching, sericitization and albitization. The distribution of each alteration type is shown in the final alteration log (Figure 17). Descriptions of each alteration type are included in Table 5, and hand sample and thin section examples are shown in Figure 18. Detailed descriptions of alteration types observed during geological core logging are also included in the IG_BH04 WP03 report (Wood, 2021a).

Based on the field-level interpretation, most of the recovered core (894.65 m) shows little to no signs of alteration (unaltered or A1 to slightly altered or A2). In total, 523.31 m or 52% of the core is altered to varying degrees. Approximately 40% (402.50 m) of the recovered core is slightly altered (A2), with the alteration concentrated on fractured surfaces and adjacent to infilled fractures. Up to 11% of the recovered drill core is moderately altered (A3), and 1% of the recovered drill core is designated as highly altered (A4). There were no intervals of completely altered rock (A5).

Note that weathering and alteration described herein are based on the initial field-level observations during core logging. The petrographic and lithogeochemical analyses of the limited sample set (n=30) indicated the presence of minimal alteration, primarily associated with sericitization of plagioclase, secondary alkali feldspar + calcite + epidote in sparse healed fractures and chloritization of biotite. In this initial sample set, no petrographic evidence for potassic alteration

was identified in the intervals originally identified as indicative of potassic alteration during core logging. Upon detailed petrographic analysis, the characteristic pink colour of feldspars associated with potassic alteration was re-interpreted as primary finely dispersed hematite.

Table 5: Summary of alteration assemblages observed in IG_BH04 during geological core logging. Note that because multiple alteration assemblages could be logged in the same interval, the sum of total alteration logged is greater than the length of the borehole.

Alteration Type	Total length (m) of logged core	Position along Borehole Association	Hand Sample Description	Associated secondary alterations
Potassic	331.52 m	Total of 84 occurrences, Between 86m and 589 m.	Pink colour; individual occurrences range from hairline to 1mm fracture infilling, mostly patchy, appearing pervasive in some zones. Note that upon detailed petrographic analysis intervals interpreted as potassic alteration were re-interpreted as hematization.	All
Hematization	75.57 m	Total of 19 occurrences, mainly in the upper 75 m	Rusty red and brown staining or coating around mineral grains.	All but sericitization
Chloritization	274.71 m	Total of 77 occurrences throughout core length.	Blue-green to dark-green minerals.	Bleaching, chloritization, potassic, silicification
Silicification	46.71 m	Sporadically between 350 m and 890 m. Total of 66 occurrences.	Light to medium grey discoloration, increase in rock strength and reduced clarity of texture. Hairline infilling to 2.2 m intervals.	Potassic, carbonatization, sericitization, silicification, hematization
Carbonatization	37.52 m	Total of 15 occurrences sporadically throughout the core.	White infilling distinguished from silicification by the hardness of minerals and effervescence when hydrochloric is used.	Chloritization, silicification, hematization
Bleaching	31.38 m	Mainly between 745m and 900 m. Total of 20 occurrences.	Off-white discoloration.	Chloritization (as primary alteration type)
Albitization	1.94 m	Total of 4 occurrences.	White mineral grains giving impression of replacement plagioclase.	None observed.
Sericitization	7.69 m	Total of 3 occurrences, mainly 900-910 m interval.	White patches characterized by fine white mica.	Potassic, carbonatization, hematization

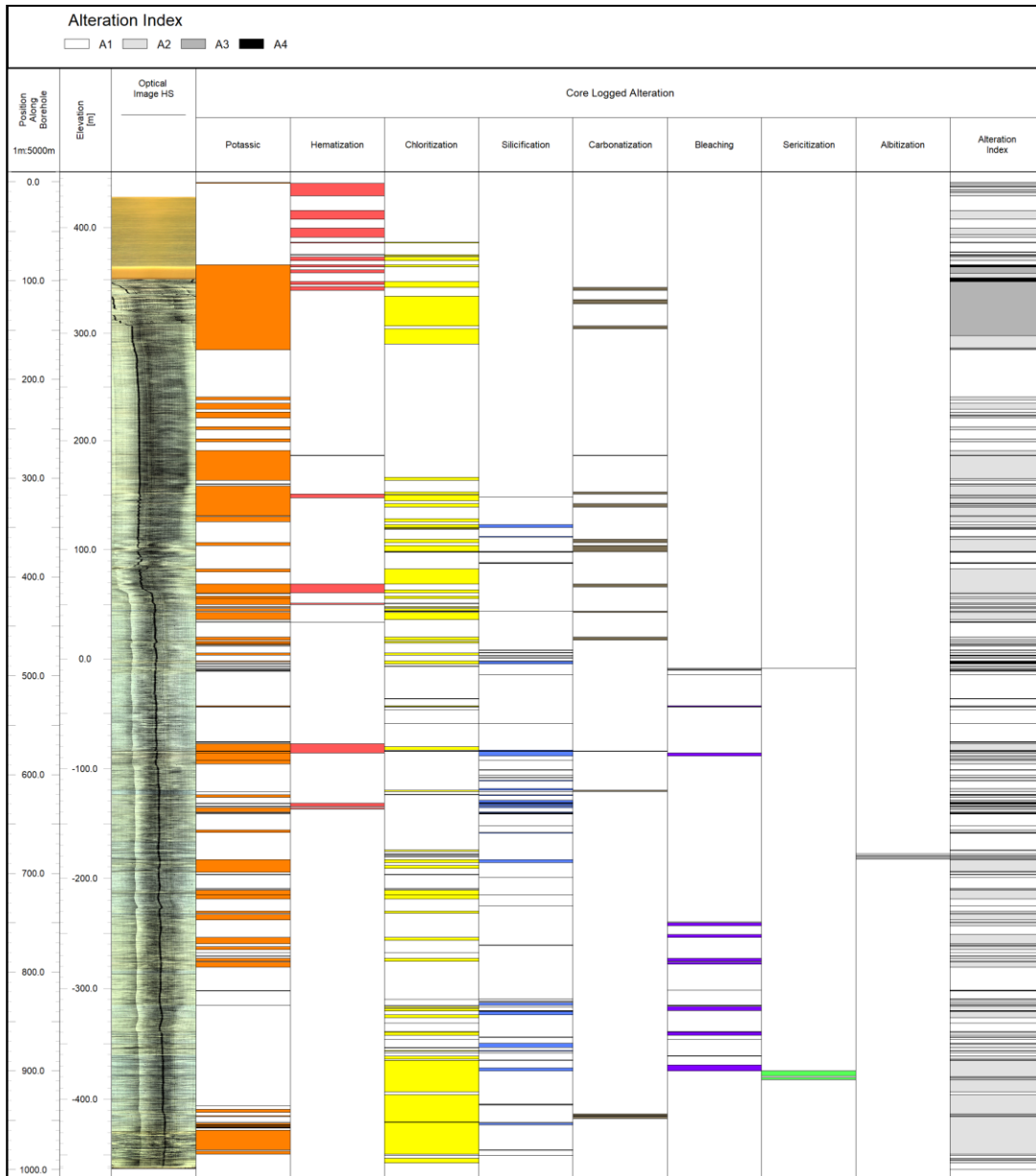


Figure 17: Alteration types and distribution along the borehole based on geological core logging and analysis of the optical televiewer log resulting in a final alteration log. A2 indicates intervals with slight alteration, A3 indicates intervals with moderate alteration, and A4 indicates intervals where alteration is pervasive along the borehole length.

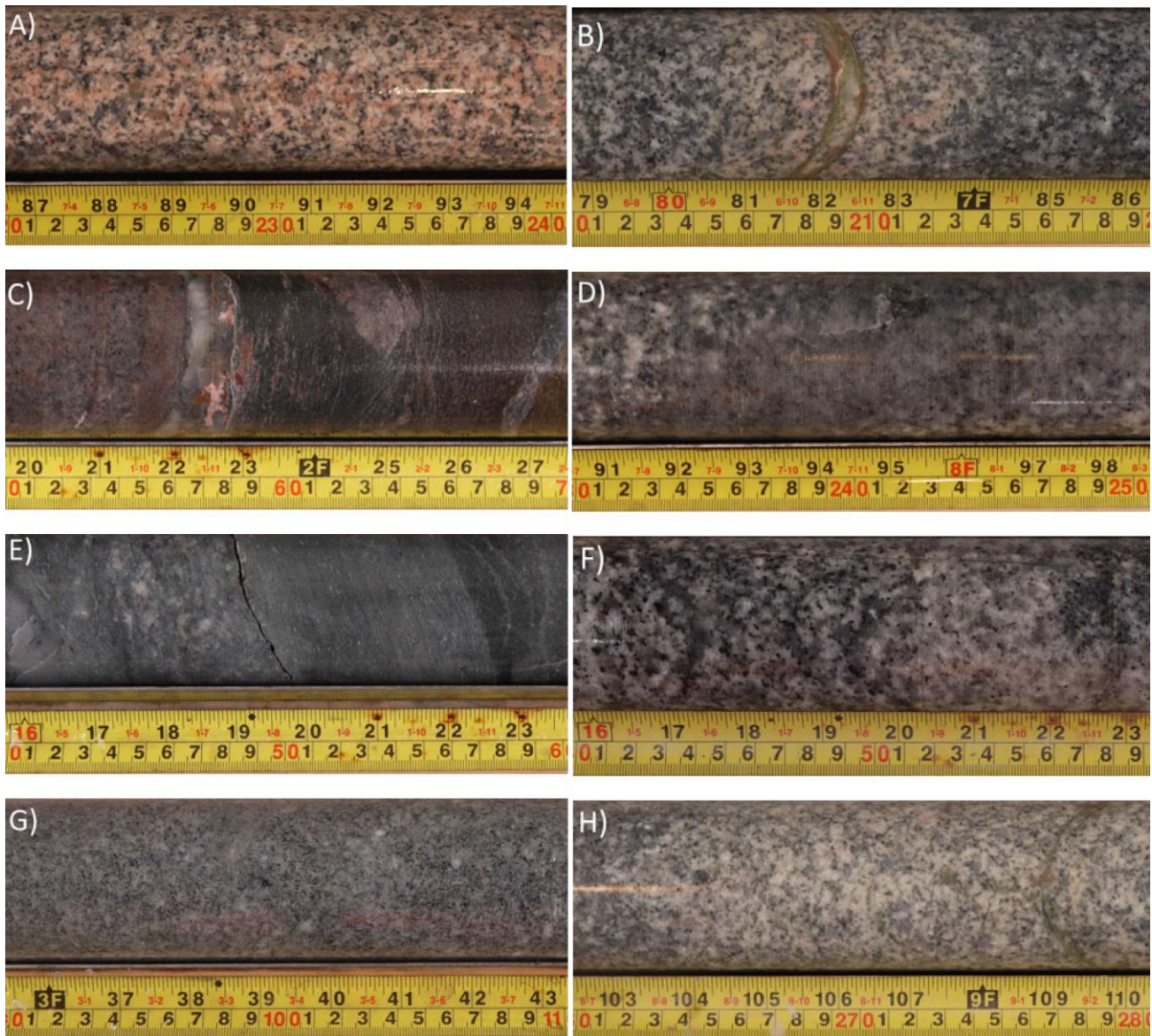


Figure 18: Common alteration assemblages logged in IG_BH04. A) Potassic alteration: Pink to orange discoloration, halos around quartz and feldspar crystals, interpreted as formation of secondary K-feldspar. **B) Chloritization:** Core photo displays epidote/chlorite fracture infill, with minor iron oxide (hematite), and weak bleaching around the fractures in tonalite. **C) Hematization:** Photo shows a contact between tonalite and mafic/amphibolite unit; on the left side of the photo hematite alteration is visible in tonalite as a reddish / rusty discoloration. The mafic unit displays chlorite alteration; the chlorite is partially to completely replacing biotite (field-level interpretation). **D) Silicification:** Core photo displays light to medium grey discoloration. **E) Carbonatization:** Core photo displays the contact between a tonalite and an amphibolite. The foliated, light grey, amphibolite displays pervasive carbonate alteration. **F) Bleaching:** Note a patch exhibiting apparent whitening (~51-58cm). **G) Sericitization:** Note white alteration patches reflecting the presence of fine white mica. **H) Albitization:** White phenocrysts were interpreted as partial to complete replacement of original plagioclase.

3.2.3 Rock Unit Classification

Rock units (RU) have been defined primarily on the basis of dominant rock types encountered within the borehole and the degree of secondary rock types encountered in the interval. The core logged rock types, combined with key continuous geophysical datasets, were used to distinguish distinct rock types within each RU and define the top and bottom interval positions. Using the available datasets, four RUs are defined within the borehole (Figure 19).

Rock Unit 1 (RU1) extends from the top of bedrock (0.67 m) to a position along borehole of 569.3 m. This interval predominantly consists of biotite granodiorite-tonalite (563.26 m, 99.11 % of the interval), with a single occurrence of feldspar-phyric tonalite dyke and a short interval of biotite tonalite making up the remaining 5.04 m. The feldspar-phyric tonalite dyke accounts for 1.0 m of logged core and the biotite tonalite accounts for 3.87 m of the rock unit interval. The feldspar-phyric tonalite dyke logged at 434.78 m to 435.74 m is the first occurrence of a subordinate rock type in the borehole. Observed alteration associated with the dyke was classified as low intensity carbonatization within the dyke, and weak amount of potassic and chloritization observed on the biotite granodiorite-tonalite of the adjacent rock mass. Throughout RU1, the biotite granodiorite-tonalite is massive, light grey to white in colour, and predominantly medium-grained. The majority of the alteration observed in this interval consists of potassic alteration and chloritization, with lesser amounts of hematization, silicification and carbonatization. With the exception of the upper ~100 m of the borehole, where casing is installed, the density, gamma and neutron logs exhibit relatively uniform profiles through this unit.

Rock Unit 2 (RU2) is 52.9 m long extending from 569.3 m to 622.2m along the borehole and was primarily defined based on the presence of amphibolite and an alteration zone in the adjacent biotite granodiorite-tonalite. This RU is composed primarily of the medium-grained, massive, biotite granodiorite-tonalite phase making up 90.71 % of the interval (47.98 m). In addition to the biotite granodiorite-tonalite, three amphibolites make up the remaining 9.29 % of the interval. The first zone logged as amphibolite occurs from 575.78 m to 576.34 m and presents contact orientations that are moderately dipping towards the NNW. The amphibolite unit was logged as highly altered dominated by hematization, chloritization, and carbonatization. Geophysical logs present an increase in natural gamma ray and increase in gamma-gamma density near the upper contact and a strong reduction in overall neutron log counts in the unit. Two additional amphibolites are logged in proximity to each other at 616.13 m to 620.64 m. The two amphibolites are separated by 0.16 m of biotite granodiorite-tonalite. These amphibolites are weakly altered, and where present, the alteration was identified as chloritization and carbonatization. The geophysical logs for these units display an increase in natural gamma ray at the top and bottom contacts, presumably associated with a contact alteration along the margin, and present a strong increase in gamma-gamma density and a strong reduction in overall neutron log counts. Overall, these geophysical log responses are broadly consistent with amphibolites logged elsewhere in the Revell batholith. Overall, the amphibolite contacts show similar geometry: gently to moderately inclined and dipping north-northwest, with logged foliation in the same orientation. The differentiating feature of this RU is the presence of the discrete amphibolite units, which make this interval a well-defined marker that can be observed in other boreholes within the Revell batholith. Overall, the amphibolites are dark green to grey in colour, fine-grained, and range from massive to strongly foliated. Alteration in this unit mostly occurs in proximity to amphibolites and is dominated by "potassic" alteration, hematization, chloritization, silicification, and hematization.

Rock Unit 3 (RU3) is 260.2 m long and extends from 623.3 m to 884.4 m along borehole. This interval predominantly consists of a mix of biotite granodiorite-tonalite and biotite tonalite as the main phase of bedrock (240.36 m, 99.57% of the interval), with few occurrences of feldspar-phyric tonalite, and aplite comprising the remaining 0.43 % of the interval length. The biotite tonalite units tend to occur most frequency towards the bottom of the RU interval and likely correspond to primary fragmentation of the magma during emplacement. Compositionally, the biotite granodiorite-tonalite and the biotite tonalite are similar, with the former containing slightly higher amounts of K-feldspar. Similar to the other defined rock units, the main biotite granodiorite-tonalite is predominantly medium-grained and massive. This unit has well-distributed potassic alteration, chloritization and silicification. Geophysical logs present a uniform natural gamma log response over the upper 120 m of the interval, followed by an abrupt increase, and variably natured, natural gamma for the remainder of the RU interval (from ~748 m to 884.4 m). The bottom of this RU3

domain is in contact with an appreciable thickness of a late feldspar-phyric granodiorite-tonalite phase of the batholith. Near the base of the RU3 interval, a few feldspar-phyric granodiorite-tonalite dykes are logged, suggesting the feldspar-phyric granodiorite-tonalite phase intruded into the biotite granodiorite-tonalite. It is likely the fluid migration as a result of this late intrusive phase may have

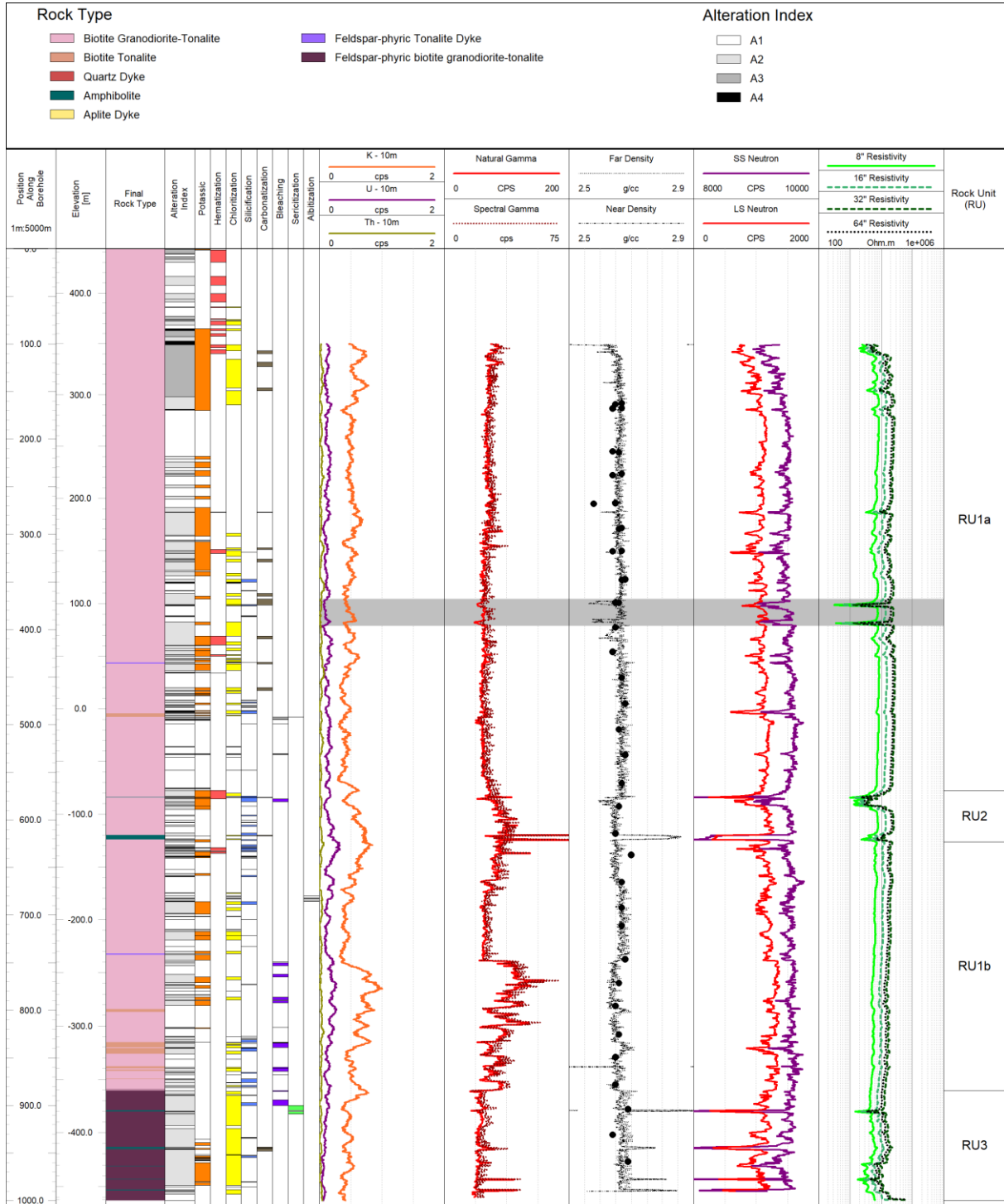


Figure 19: Summary of final logged lithology, alteration and key geophysical logs presented alongside interpreted rock units for IG_BH04. Due to the low spectral gamma counts, K, U and Th were evaluated using a 10 m window, resulting in a smoothing of their profiles.

led to contact alteration within the biotite granodiorite-tonalite and biotite tonalite at the base of RU3, and may have resulted in an elevated natural gamma ray response. The shift in natural gamma log at 748 m also coincides with a subtle decrease in gamma-gamma density and increase in neutron response in the bottom part of this RU (note; an increase in neutron response would correspond to a decrease in neutron derived total porosity). Despite the subtle variability in geophysical logs, the overall observations from core indicate that the RU interval is largely consistent in rock type, mineralogy and grain size.

Lastly, Rock Unit 4 (RU4) includes the remaining 114.8 m of the borehole, extending from 884.4 m to bottom of hole at 1000.2 m. This unique interval to this borehole, and also unique to other boreholes in the Revell batholith, is primarily composed of feldspar-phyric granodiorite-tonalite unit as the main phase of bedrock (109.05 m, 94.99 % of the interval). As noted above, this rock unit has similar granodioritic-tonalitic composition as the main biotite granodiorite-tonalite unit, and visually distinct appearance (porphyritic texture with larger feldspars in groundmass of finer quartz and biotite). The feldspar-phyric granodiorite-tonalite exhibits nearly identical geophysical log responses as these other two rock types. Alteration logged within the feldspar-phyric granodiorite-tonalite unit is predominantly chloritization, which was observed on more than 85% of this RU interval. Lesser amounts of potassic alteration, silicification, carbonatization, sericitization, and bleaching are also observed within this RU interval. In addition to the feldspar-phyric biotite granodiorite-tonalite unit, seven amphibolites were logged with varying thickness from 0.09 to 1.88 m, making up 4.76 % or 5.46 m of the interval. Overall, the amphibolites are dark green to grey in colour, fine-grained and range from massive to strongly foliated. In general, the amphibolite occurrences tend to be uniformly spaced in this RU, where sometimes when amphibolites occur they tend to be in clusters of two or three thin units. Although not always, the amphibolites commonly show an increase in natural gamma response, as well as the indicative increase in gamma-gamma density and reduction in neutron counts.

Table 6 presents a summary of the final RU interpretations, classified according to the dominant rock type encountered therein. The final classification based both on the distribution of the dominant rock types identified and catalogued in the final lithology log, and summarized in the RU descriptions above, suggest that the RUs can be classified in three dominant domains, including: (1) biotite granodiorite-tonalite, (2) biotite granodiorite-tonalite with amphibolite and (3) feldspar-phyric biotite granodiorite-tonalite with amphibolite. Similarities observed between each of the RU descriptions, mainly dominant rock type, allow the RU intervals to be classified into common rock units. Rock units RU1 and RU3, are dominated by biotite granodiorite-tonalite, exhibit similar geophysical signatures, and are devoid of amphibolites. These two rock units are reclassified as RU1a and RU1b. RU2 represents an interval dominated by biotite granodiorite-tonalite with the presence of amphibolite units, and RU3 represents an interval dominated by feldspar-phyric biotite granodiorite-tonalite with the presence of amphibolite units. Based on the presence of amphibolites, the RU2 and RU3 units could be classified as common rock units. However, the differences between the dominant bedrock types allow for these units to remain distinct.

Table 6: Summary of Classified Rock Units

Positional Range (m)	RU#	Dominant Rock Type	Classified RU
0.67 – 569.3 m	RU1	Biotite granodiorite-tonalite	RU1a
569.3 m to 623.2 m	RU2	Biotite granodiorite-tonalite, with amphibolite	RU2
623.2 m – 884.4 m	RU3	Biotite granodiorite-tonalite	RU1b
884.4 m – 1000.2 m	RU3	Feldspar-phyric biotite granodiorite-tonalite, with amphibolite	RU3

One uncertainty associated with this initial rock unit model is the location of interpreted rock unit boundaries along the borehole. Three of the rock units are predominantly composed of biotite granodiorite-tonalite. Consequently, there is no clear physical boundary that can be used to differentiate them. As described above, the boundaries are largely based on occurrences of amphibolite along the length of the borehole. As a result, these rock unit boundaries have a fair amount of subjectivity embedded in their locations. Despite this uncertainty, it is likely that these rock unit subdivisions adequately parse the borehole into domains that capture the general changes in the rock types that may be important in characterizing the geosphere. It will be important to evaluate whether additional geoscientific information from the other boreholes will fit within this rock unit framework or if a different picture will emerge.

3.2.4 Structural Interpretation

A description and interpretation of bedrock structural features measured along the borehole are presented in this section. Structural measurements include both geological and geotechnical characteristics captured during geological core logging and geophysical televiewer logging, integrated together into a final structure log. The final integrated structure log contains 3061 natural features (Table 7). This total includes 47 geological contacts, and 3014 additional planar structures. Of the total number of natural planar features, 1620 were logged and observed only during geological core logging, 699 structures were logged both in geological core logging and televiewer logging, and 275 structures were logged and observed only by televiewer. An additional 1692 non-natural mechanical breaks were recorded during geological core logging which have already been separated from the dataset presented below.

Table 7: Summary of structures observed in the borehole.

Structure Type	Number of Oriented Structure			Un-oriented Occurrences (Core Logged Only)	Total Structures Logged
	Core Logged Only	Both (Core and Televiewer)	Televiewer Logged Only		
Joint (JN)	1363	592	207	425	2587
Vein (VN)	194	55	51	31*	331
Fault (FLT)	6	0	2	0	8
Shear Zones (SHR/SHRD)	16	6	4	6	32
Contact (CO)	7	37	0	3	47
Igneous Primary Structure (IPS)	27	7	11	0	45
Foliation (FO)	7	1	0	2	10
Broken Core Zone (BCZ)	0	1	0	0	1
Total	1620	699	275	467	3061

**Includes 2 VN identified only in Televiewer and 5 VN identified in Both Core and Televiewer but not confidently oriented.*

During geological core logging, structures were oriented relative to an arbitrary reference line drawn along the length of the axis of each core run. The methodology for assigning true dip and dip

direction to each logged structure, integrating the geological core logging information with the orientation information extracted from the televiewer log datasets, is presented in Appendix D. During this process of structure integration, 2594 (85 %) of the planar features (44 lithological

contacts and 2550 other planar structures) were oriented and assigned true dip and dip direction. The remaining 467 un-oriented structures, primarily joints, could not be assigned a true dip or dip direction as a result of being located within sections of the core that could not be corrected with the televiewer information. Oriented structural data are plotted by structure type and shown on equal area, lower-hemisphere stereographic projections (stereonet) throughout this section.

Borehole trajectory will directly influence the under-representation of certain orientations of planar structures (e.g., Terzaghi, 1965). IG_BH04, which was drilled at an inclination of -70° towards an azimuth of 110° , will mostly under-represent vertical structures that strike NW-SE and structures that strike NE-SW and dip parallel to the borehole plunge. To acknowledge this bias and begin to explore the implications of it, the presentation below includes Terzaghi-weighted contoured pole densities along with the unweighted data for all planar structures except for oriented lithological contacts. The legend associated with each of the weighted stereonet indicates the number of features expected based on the Terzaghi weighting. The minimum bias angle applied for this analysis, using the software DIPS© (Version 7) by Rocscience, is 15° , giving a maximum weight of 3.86. A summary of orientation information for all 2550 naturally occurring, oriented, planar structures (excluding geological contacts) is presented in Figure 20. In comparing the unweighted and Terzaghi-weighted contours (Figure 21), it is clear that the latter emphasizes the pole clusters of steeper dipping structures oriented at a low angle to the core axis and de-emphasizes the gently dipping structures oriented at a high angle to the core axis.

More recently, advanced procedures for addressing orientation bias have been reported in the literature (e.g., Davy et al., 2006). However, such alternative approaches require not yet available information such as fracture size-distribution for each orientation set. The use of such methods will be made possible, and justified, as additional borehole and surface structural information become available.

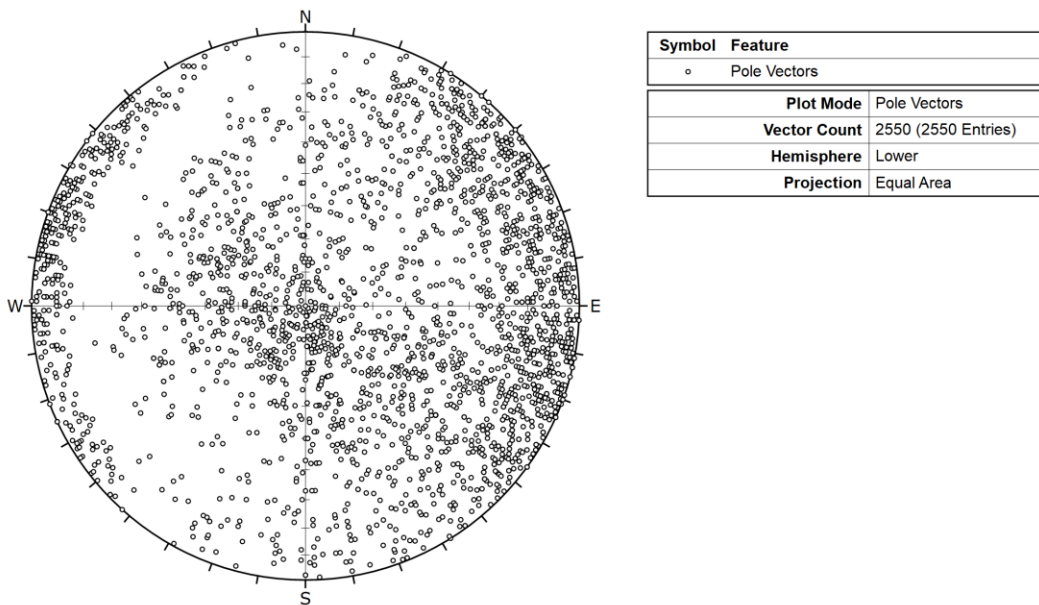
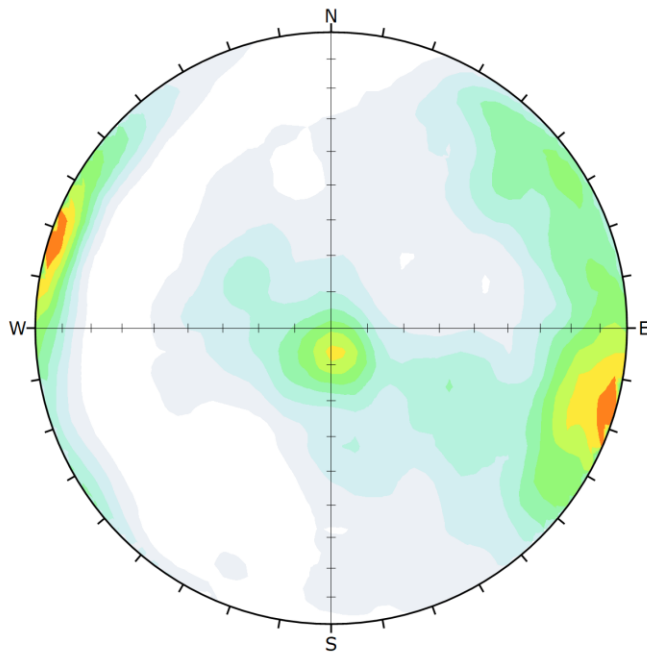
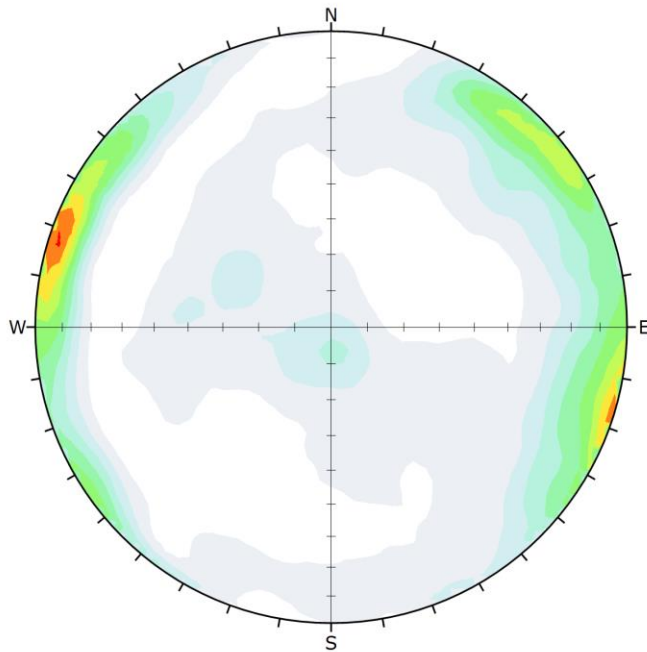


Figure 20: Equal Area Lower Hemisphere Projection (stereonet) showing poles to planar structural measurements, unweighted (n = 2550).



Color	Density Concentrations	
	0.00 - 0.45	
	0.45 - 0.90	
	0.90 - 1.35	
	1.35 - 1.80	
	1.80 - 2.25	
	2.25 - 2.70	
	2.70 - 3.15	
	3.15 - 3.60	
	3.60 - 4.05	
	4.05 - 4.50	
Contour Data		Pole Vectors
Maximum Density		4.05%
Contour Distribution		Fisher
Counting Circle Size		1.0%
Plot Mode		Pole Vectors
Vector Count		2550 (2550 Entries)
Hemisphere		Lower
Projection		Equal Area



Color	Density Concentrations	
	0.00 - 0.55	
	0.55 - 1.10	
	1.10 - 1.65	
	1.65 - 2.20	
	2.20 - 2.75	
	2.75 - 3.30	
	3.30 - 3.85	
	3.85 - 4.40	
	4.40 - 4.95	
	4.95 - 5.50	
Contour Data		Pole Vectors
Maximum Density		5.03%
Contour Distribution		Fisher
Counting Circle Size		1.0%
Plot Mode		Pole Vectors
Vector Count (Weighted)		5066 (2550 Entries)
Terzaghi Weighting		Minimum Bias Angle 15°
Hemisphere		Lower
Projection		Equal Area

Figure 21: Equal Area Lower Hemisphere Projections (stereonets) showing a summary of the poles for planar structural measurements. Top: all data – contours, unweighted (n = 2550). Bottom: all data – contours, Terzaghi-weighted (n = 5066).

3.2.4.1 Structures

The structural information presented below includes discussion of features logged as igneous primary structures, contacts, ductile structures, brittle structures (including joints, veins and faults), and linear structures.

Igneous Primary Structures

Igneous primary structures (IPS) include features interpreted to have originated with the formation or emplacement of the igneous rock, including igneous flow foliation and igneous layering. For IG_BH04, a total of 45 igneous primary structures were identified. These features are generally characterized by sharp to gradational changes in grain size or concentration of the main rock-forming minerals in the granodiorite-tonalite bedrock, including biotite, quartz, or plagioclase. All occurrences were intact in the core and all occurrences were successfully oriented. The thicknesses of the igneous primary structures range from mm-scale to a maximum of 43 cm. One example of igneous primary layering, identified by an interval of core with varying biotite content, is shown in Figure 22a. Some of the igneous primary structures identified may instead be mafic schlieren. The true nature of all features logged as igneous primary structures will continue to be assessed as additional information becomes available. Figure 23 presents the stereographic projection of all igneous primary structures. The majority of poles to igneous primary structures define planes that dip gently towards the east and north.

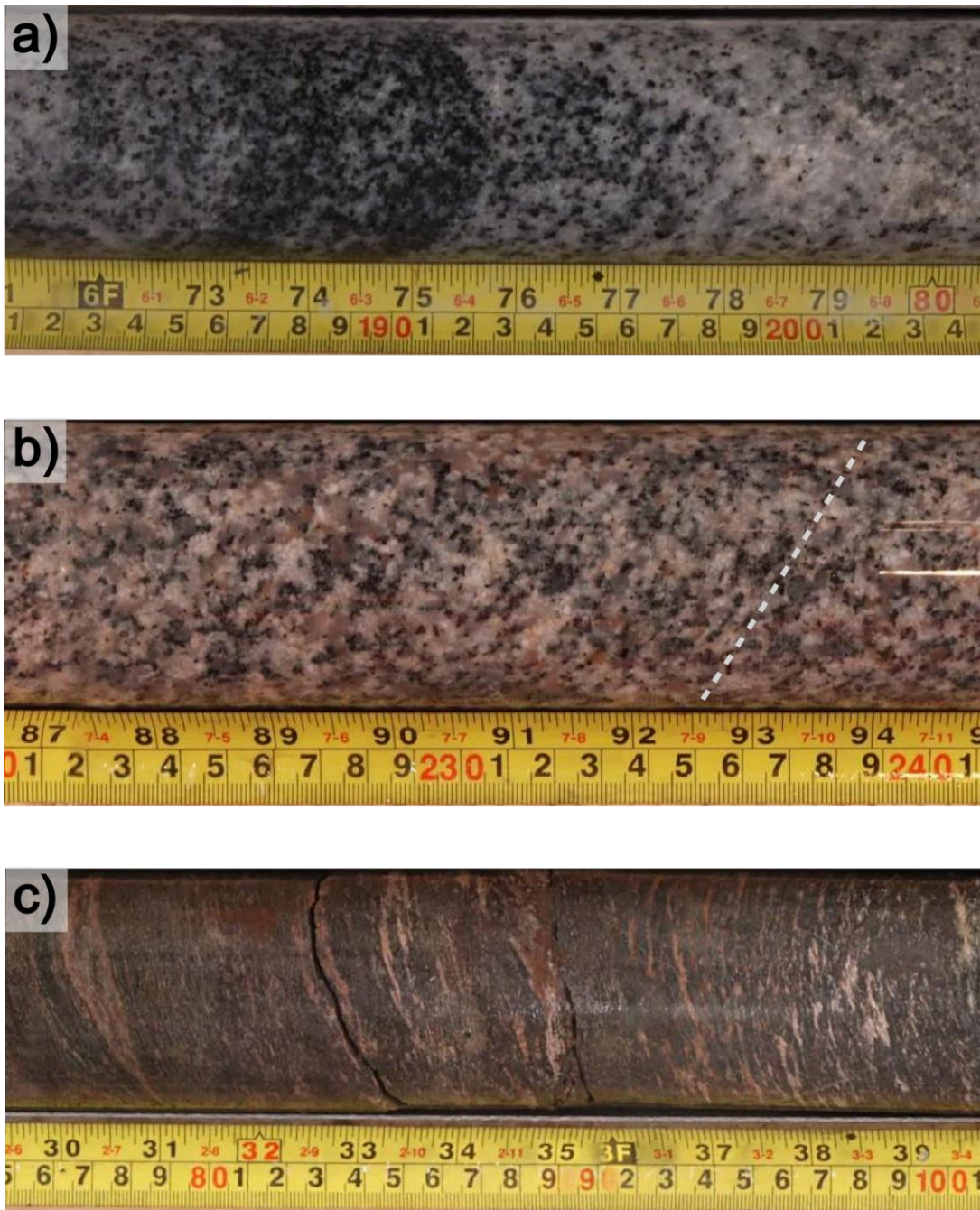


Figure 22: Examples of primary igneous and ductile structures. a) Subtle variation in biotite content (from left to right) defining a primary igneous layering, in biotite granodiorite-tonalite (770 m along borehole). b) Weak foliation defined by alignment of biot

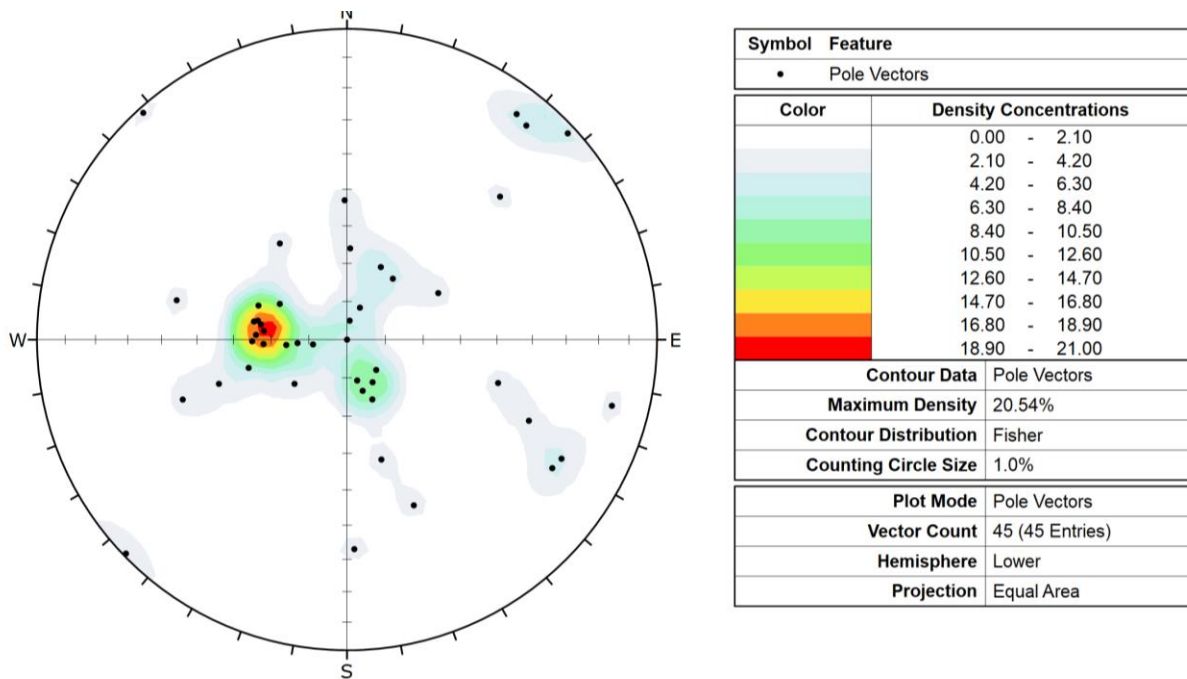


Figure 23: Stereonet showing poles and unweighted contours for Igneous Primary Structures (IPS; n = 45).

Contacts

Top and bottom contact (CO) orientations were logged for each change in rock type wherever the boundary was sharp enough to confidently identify a contact plane. The majority of the logged contacts represent boundaries between occurrences of biotite granodiorite-tonalite and other rock types. Thirty-eight of the logged contacts were identified as sharp and the remaining eight were identified as gradational. The gradational occurrences were primarily identified where biotite granodiorite-tonalite transitioned to biotite tonalite.

Out of a total of 47 logged contacts, 44 of these could be confidently oriented. In the other three occurrences, a single plane could not be defined due to the gradational nature of the contact between biotite granodiorite-tonalite and biotite tonalite. The poles to the planes defining all oriented geological contacts are shown in Figure 24. Overall, there is a very large spread in the data, with the majority of poles (20/44; 45 %) plotting in the southeastern quadrant of the lower hemisphere projection.

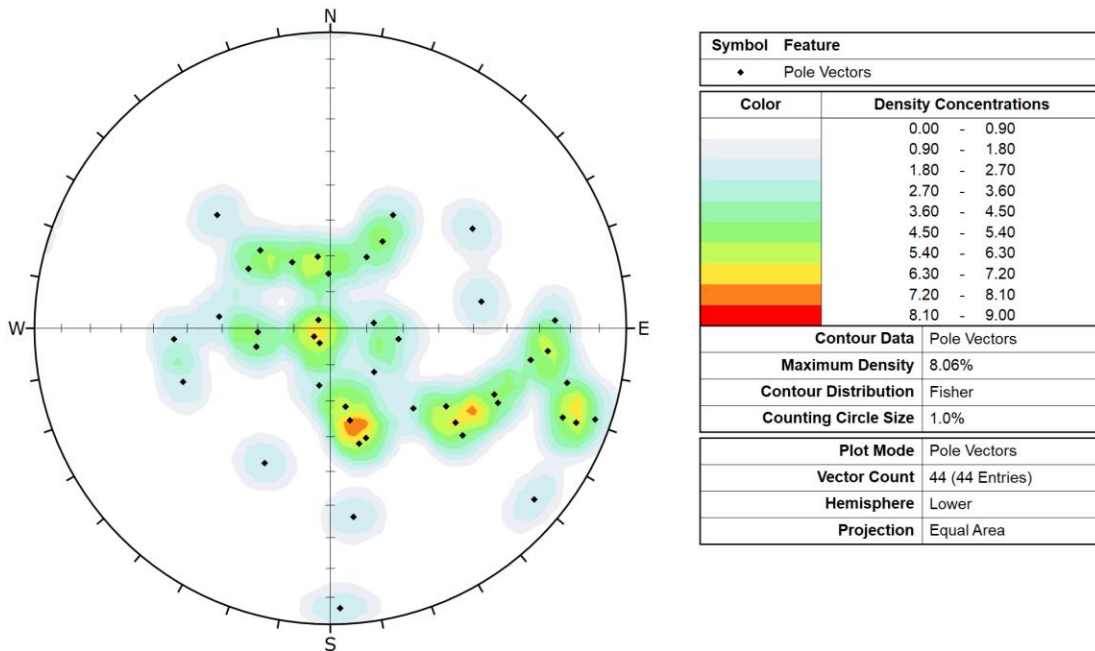


Figure 24: Stereonet showing poles and unweighted contours for all oriented geological contacts (n = 44).

Twenty amphibolite contacts (ten occurrences) were successfully oriented (Figure 25), including three instances logged as broken. The majority of the poles to amphibolite contacts plot in the southeast quadrant of the stereonet indicating gently to steeply inclined contacts that dip northwest. The amphibolite occurrences generally exhibit evidence of penetrative ductile to brittle-ductile deformation obscuring any indication of their primary relationship with the surrounding bedrock. The deformation manifests as cm- to dm-scale localized shear zones (Figure 22c) that are developed within the amphibolite occurrences as well as along, and sub-parallel to, their contacts.

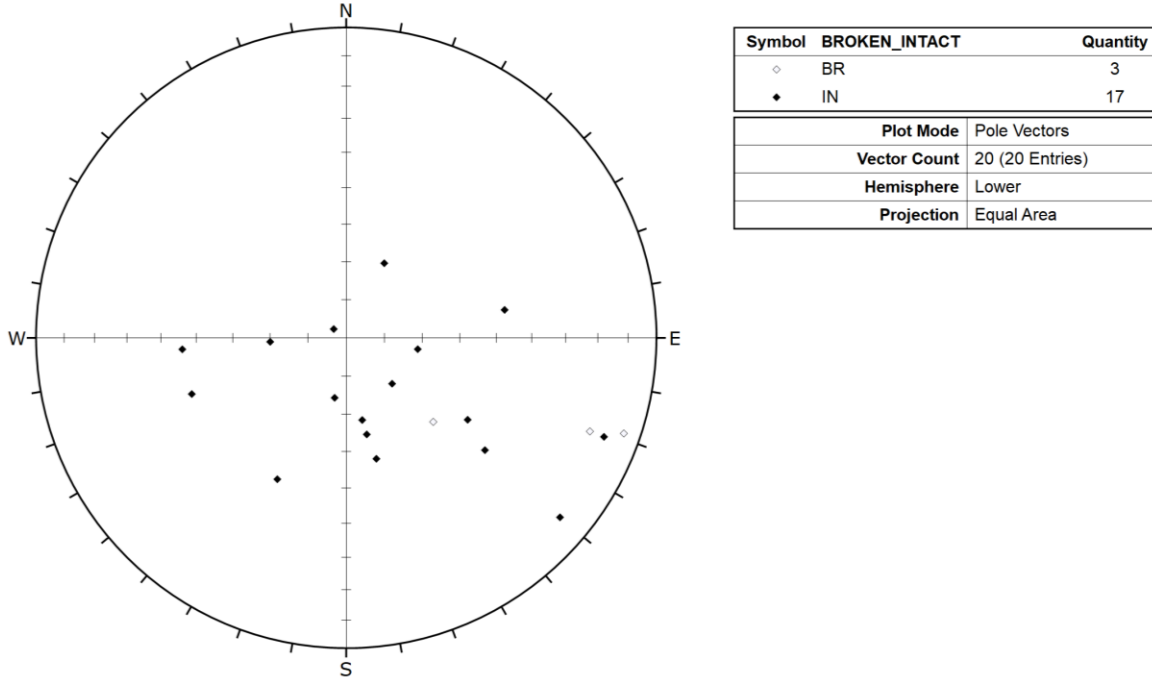


Figure 25: Stereonet showing poles for amphibolite contacts (n = 20). Open symbols identify broken contacts (BR) and filled symbols identify intact contacts (IN).

The poles to the contact orientations for five distinct felsic rock phases are shown in Figure 26. This includes aplite dykes, felspar-phyric tonalite dykes and quartz dykes, as well as occurrences of biotite tonalite and feldspar-phyric granodiorite-tonalite. Poles to aplite dyke contacts (n = 2), identified by green diamonds, define one occurrence with parallel top and bottom contacts that are moderately inclined and dip west. Both aplite dyke contacts were logged as gradational and intact. Poles to feldspar-phyric tonalite dyke contacts (n = 4), identified by dark purple diamonds, define two occurrences, including one with contacts that are moderately inclined and dip west-northwest and one with contacts that are gently inclined and dip east. All feldspar-phyric tonalite dyke contacts were logged as sharp and intact. Poles to quartz dyke contacts (n = 2), identified by blue diamonds, define one occurrence with parallel top and bottom contacts that are moderately inclined and dip east. Both quartz dyke contacts were logged as sharp and intact. Poles to biotite tonalite occurrences (n = 13), identified by red diamonds, are steeply to gently inclined and primarily dip north, northwest, or southwest. The majority of biotite tonalite contacts were logged as sharp, and all were logged as intact. Poles to feldspar-phyric granodiorite-tonalite occurrences (n = 17), identified by light purple diamonds, are steeply to gently inclined and primarily dip northwest or southeast. All feldspar-phyric tonalite dyke contacts were logged as sharp and intact, except for two contacts logged as sharp and broken adjacent to amphibolite occurrences.

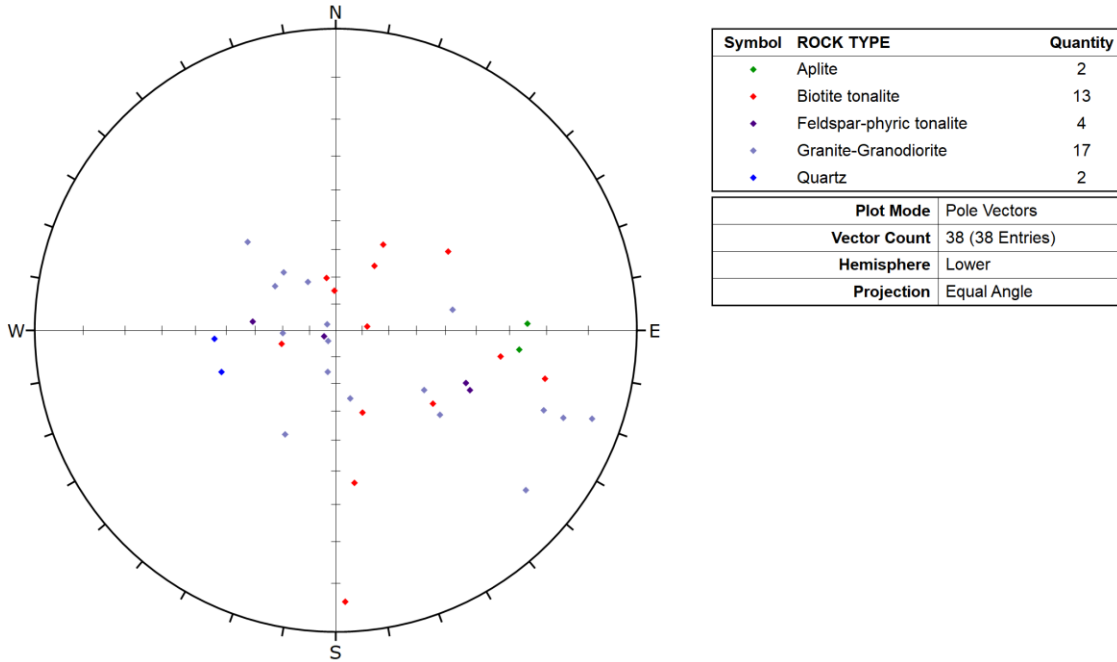


Figure 26: Stereonet showing the distribution of poles to contacts for felsic rock occurrences, including aplite (n = 2), feldspar-phyrlic tonalite (n= 4) and quartz (n = 2) dykes, and biotite tonalite (n = 13) and feldspar-phyrlic biotite granodiorite-ton

Ductile Structures

Ductile structures identified in IG_BH04 include foliation (FO) and both ductile shear zones (SHR) and brittle-ductile shear zones (SHRD). Stick plots indicating the distribution of the ductile structures are included in Figure 27. Figure 27 also includes the overall per metre fracture frequency and stick plots for all brittle structures logged in the borehole. The brittle structures will be described in detail after presentation of the ductile structures.

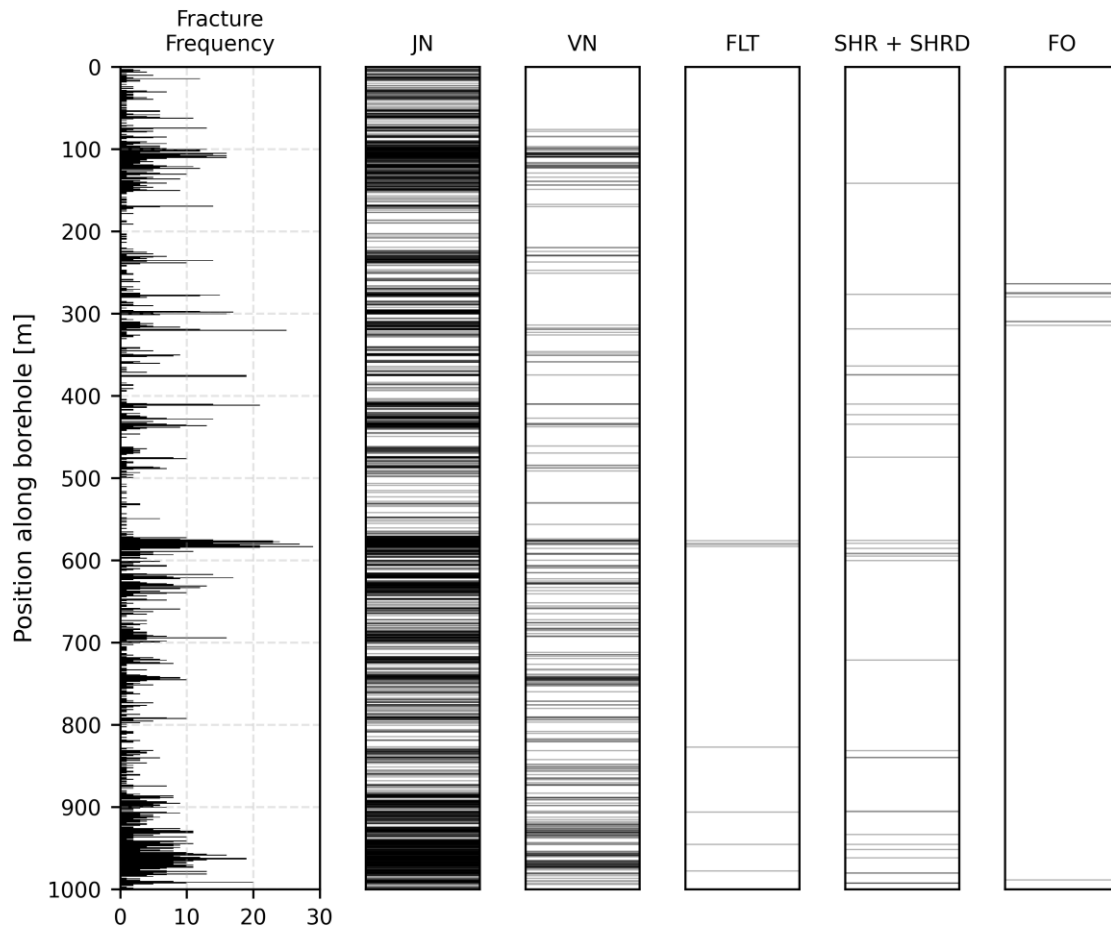


Figure 27: Summary log showing the frequency per metre of brittle structures (left) in comparison to stick plots that show the distribution of all brittle structures (Joints – JN, Veins – VN and Faults - FLT) and all ductile structures (Shear Zones – SHR and Foliation – FO).

Foliation was logged where preferential orientation of mineral grains was observed. A total of 10 foliation occurrences were recorded. These occurrences are clustered around 300 m along the length of the borehole within biotite granodiorite-tonalite (Figure 27). In all occurrences foliation is identified as weak and defined by the alignment of biotite. An example of weak foliation in biotite granodiorite-tonalite is shown in Figure 22b.

Figure 28 presents the stereonet of foliation orientations. Eight of ten foliation occurrences were successfully oriented. Poles to the foliation planes are moderately to steeply inclined and dip northwest or southwest, or moderately to gently inclined and dip east.

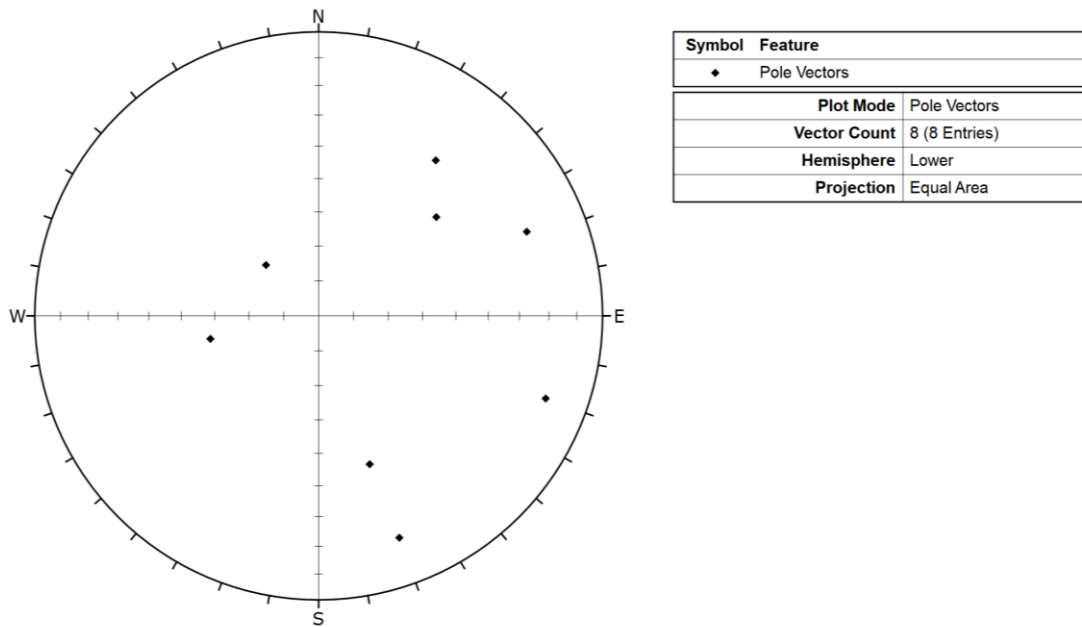


Figure 28: Stereonets showing orientation information for Foliation (FO). All data – poles, unweighted (n = 8).

A total of 32 shear zones were logged in IG_BH04. These structures were initially identified during geological core logging as either ductile shear zones (SHR) or brittle-ductile shear zones (SHRD). In the assessment of the entire shear zone dataset, it was determined that all occurrences more likely represent a continuum of ductile to brittle deformation. Therefore, the presentation herein integrates all occurrences simply as a single ductile shear zone dataset (SHR + SHRD). A shear zone example is shown in Figure 22c.

Sixteen (50 %) of the shear zones were identified in geological core logging only. In addition, six shear zones were identified in both geological core logging and televiewer logs, and four were identified only in televiewer logs. Shear zones range in width (length along borehole) from one to 54 cm. The most common mineral phase associated with shear zones is quartz, with lesser associations of chlorite, epidote, hematite and amphibole.

The shear zones are most commonly observed along the contacts of, or within, amphibolite occurrences. The stick plot of shear zone occurrences highlights the observation that they are identified along the length of the borehole below approximately 150 m along the borehole, and their distribution is commonly coincident with peaks in the fracture frequency (Figure 27). Figure 29 presents the unweighted and weighted stereonet for all oriented shear zones. Twenty-six (81 %) of the shear zones were successfully oriented. Poles to oriented shear zones in the unweighted dataset are predominantly distributed throughout the southeast quadrant of the lower hemisphere projection, defining subhorizontal to steeply inclined shear zones that dip northwest. The Terzaghi weighted dataset emphasizes a small cluster of steeply inclined shear zones that dip north.

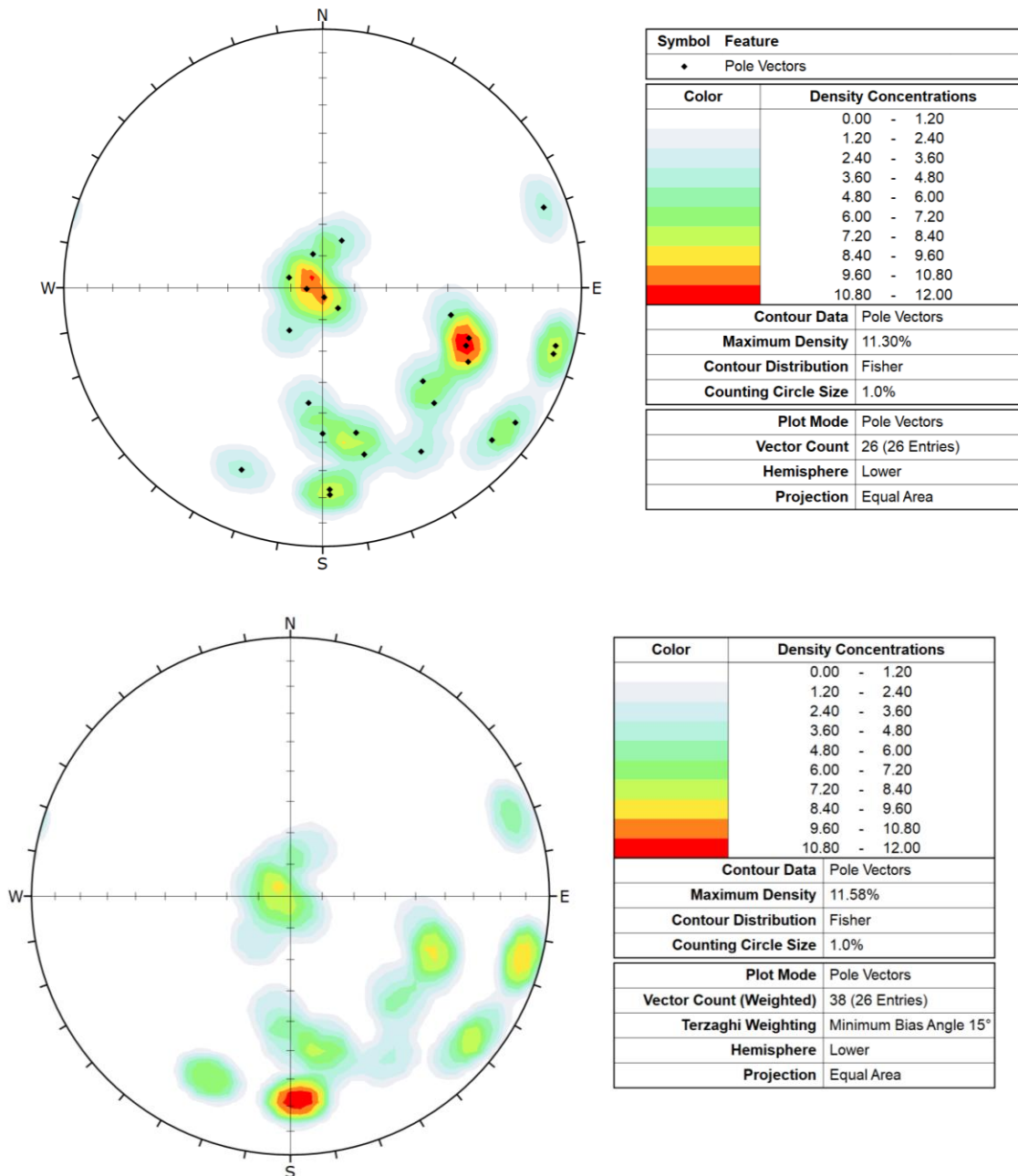


Figure 29: Stereonets showing orientation information for Shear Zones. Top: All data – poles and contours, unweighted (n = 26). Bottom: All Shear Zone data, Terzaghi-weighted contours (n = 38).

Brittle Structures

This section describes the brittle structures, including all joints (JN), veins (VN), and faults (FLT), representing the group of features collectively identified as fractures. A summary of the per metre fracture frequency for all brittle structures, as well as stick plots detailing their distribution in the borehole, is included in Figure 27. Typical examples of brittle structures identified in the borehole are included in Figure 30.

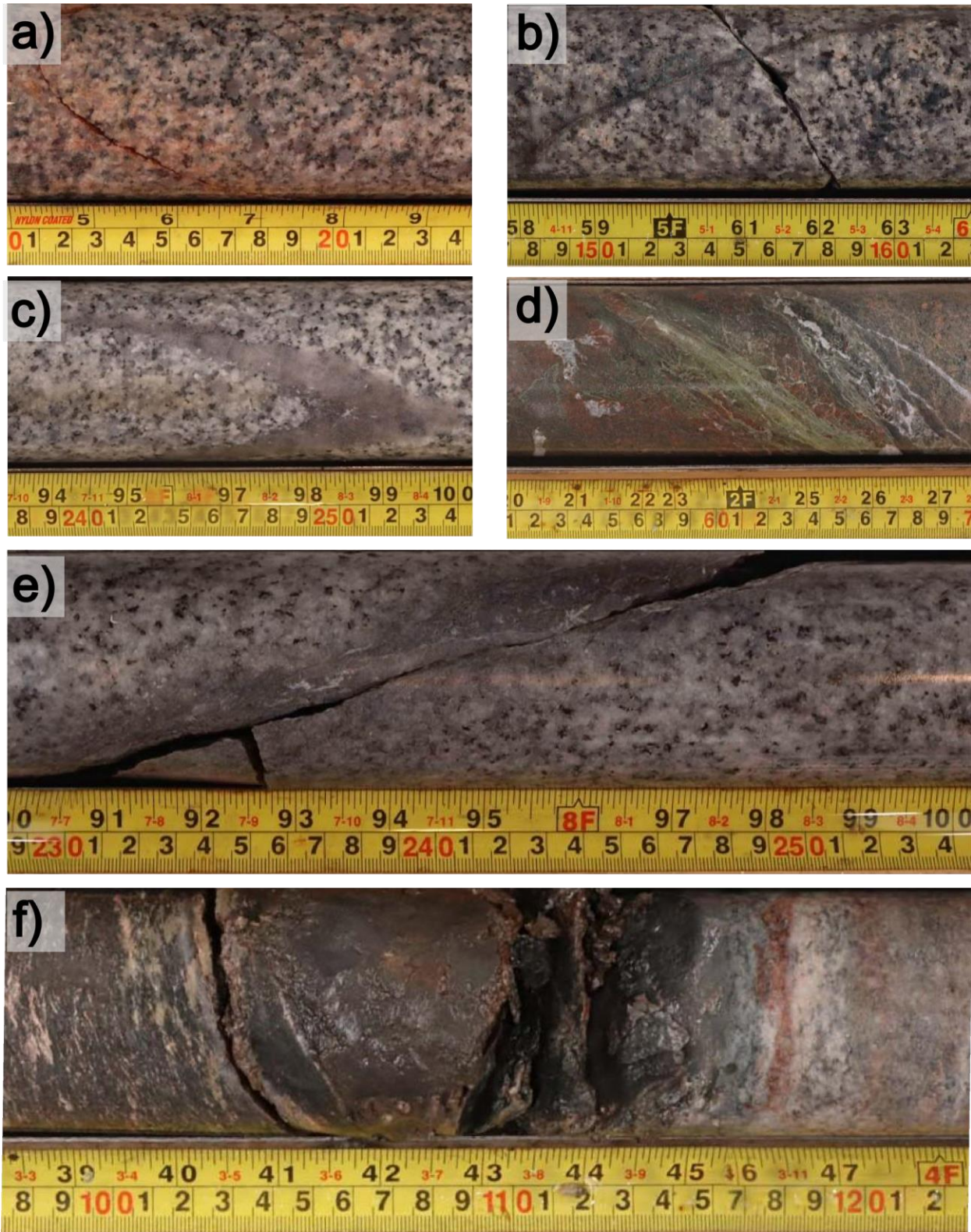


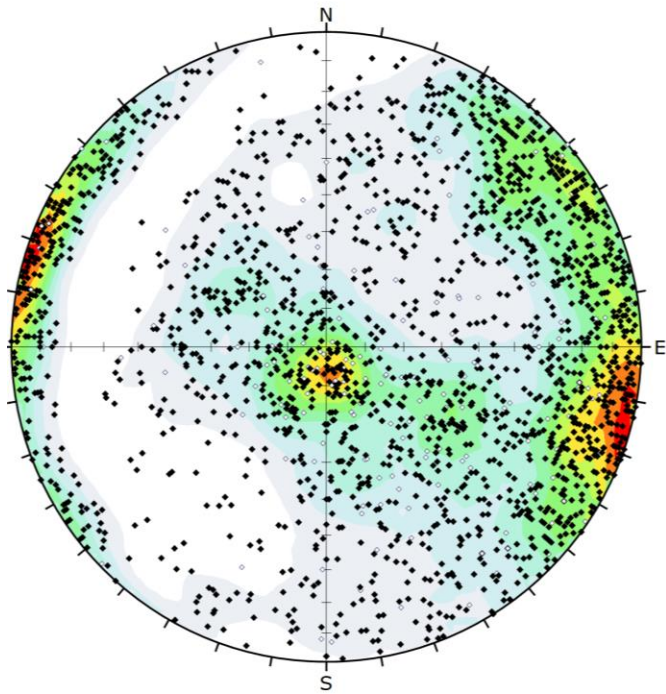
Figure 30: Examples of brittle structure. a) Broken hairline joint with iron stain and hematite alteration, in biotite granodiorite-tonalite (278 m). b) Broken joint with no surface alteration cross-cutting intact joint, in biotite granodiorite-tonalite (172 m). Note that mm-scale geological aperture logged for broken joint was reduced to 0 mm based on televiewer interpretation. c) Intact mm-scale quartz-filled vein, in biotite granodiorite tonalite (593 m). d) Intact hairline to mm-scale epidote and calcite-filled veins surrounded by hematite alteration, in feldspar-

phyric biotite granodiorite-tonalite (946 m). e) Broken fault plane with quartz infill, in biotite granodiorite-tonalite (827 m). f) Soft-gouge-filled fault zone at sheared and altered contact between amphibolite (left) and biotite granodiorite-tonalite (right; 579 m).

A total of 2587 joints were logged in IG_BH04. They are distributed along the entire length of the borehole and since they dominate the total brittle structure dataset the peaks in the per metre fracture frequency correlate well with the clusters evident in the stick plot of all joints (Figure 27). A total of 242 of the 2587 joints (9 %), were logged as broken, while the remaining 2345 (91 %) were logged as intact or partially intact. A total of 2361 joints (91 %) logged joints exhibit no measurable geological aperture, meaning that any natural aperture, if present, was too small to identify visually (sub-mm scale). In the remaining occurrences, mm to cm-scale geological apertures (maximum of 10 mm) were identified through analysis of the core and televiewer data. Where joints were logged as broken during geological core logging, and did not exhibit any geological aperture, the adjacent broken core pieces were able to be fit back together without any visual evidence of an opening along the fracture plane. In these instances, it is possible that the break was mechanically induced as a result of the drilling process along a joint that was otherwise intact *in situ*.

Joint surfaces were logged as clean, with no associated mineral infill, in 689 occurrences (27 %), while the remaining 1898 (73 %) included observation of staining, slight alteration, or coating with a mineral infill. The most common secondary mineral phases associated with joints were quartz, chlorite, calcite, iron oxide (hematite) and epidote. Typical examples of joints are shown in Figure 30, including, a hairline broken joint with iron stain on the fracture surface and an alteration halo of hematization (Figure 30a), and a broken joint with no discernible surface alteration (Figure 30b). The latter broken joint was originally logged with a mm-scale geological aperture but during interpretation of the televiewer data it was determined that there was no aperture *in situ*.

The majority of identified joints were logged in geological core logging only (1788; 69 %) or both geological and televiewer logs (592; 23 %). The remaining 207 joints (8 %) were identified in televiewer logs only. Through the integration process, 2162 of 2587 (84 %) joints were successfully oriented. Figure 31 presents the unweighted and weighted stereonet for all oriented joints. The unweighted stereonet emphasizes one prominent pole cluster of vertical joints striking north-northeast and another cluster of subhorizontal joints. A less prominent pole cluster define steeply inclined joints that dip southwest. This latter, less prominent pole cluster is emphasized slightly in the Terzaghi-weighted joint dataset, while two more prominent pole clusters are de-emphasized, especially the subhorizontal one.

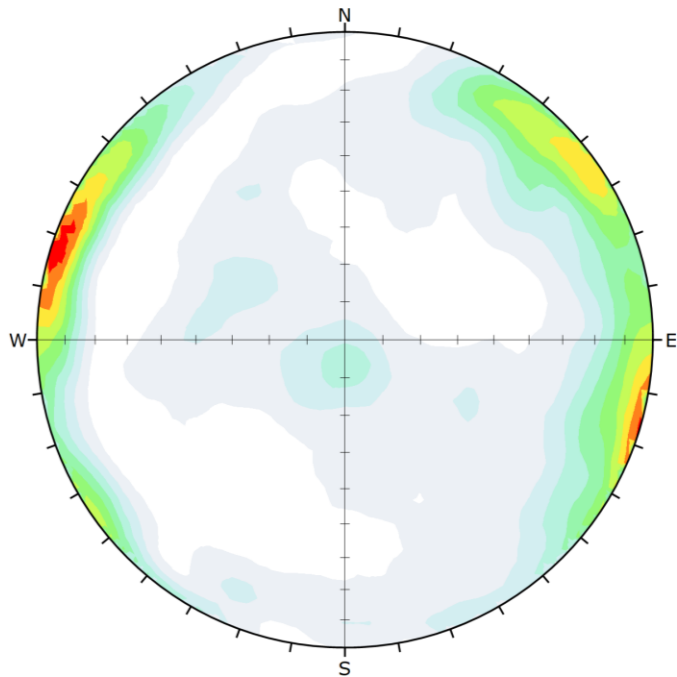


Symbol	STRUCT-BR_IN	Quantity
○	BR	172
●	PIN/IN	1990

Color	Density Concentrations
	0.00 - 0.40
	0.40 - 0.80
	0.80 - 1.20
	1.20 - 1.60
	1.60 - 2.00
	2.00 - 2.40
	2.40 - 2.80
	2.80 - 3.20
	3.20 - 3.60
	3.60 - 4.00

Contour Data	Pole Vectors
Maximum Density	3.94%
Contour Distribution	Fisher
Counting Circle Size	1.0%

Plot Mode	Pole Vectors
Vector Count	2162 (2162 Entries)
Hemisphere	Lower
Projection	Equal Area



Color	Density Concentrations
	0.00 - 0.50
	0.50 - 1.00
	1.00 - 1.50
	1.50 - 2.00
	2.00 - 2.50
	2.50 - 3.00
	3.00 - 3.50
	3.50 - 4.00
	4.00 - 4.50
	4.50 - 5.00

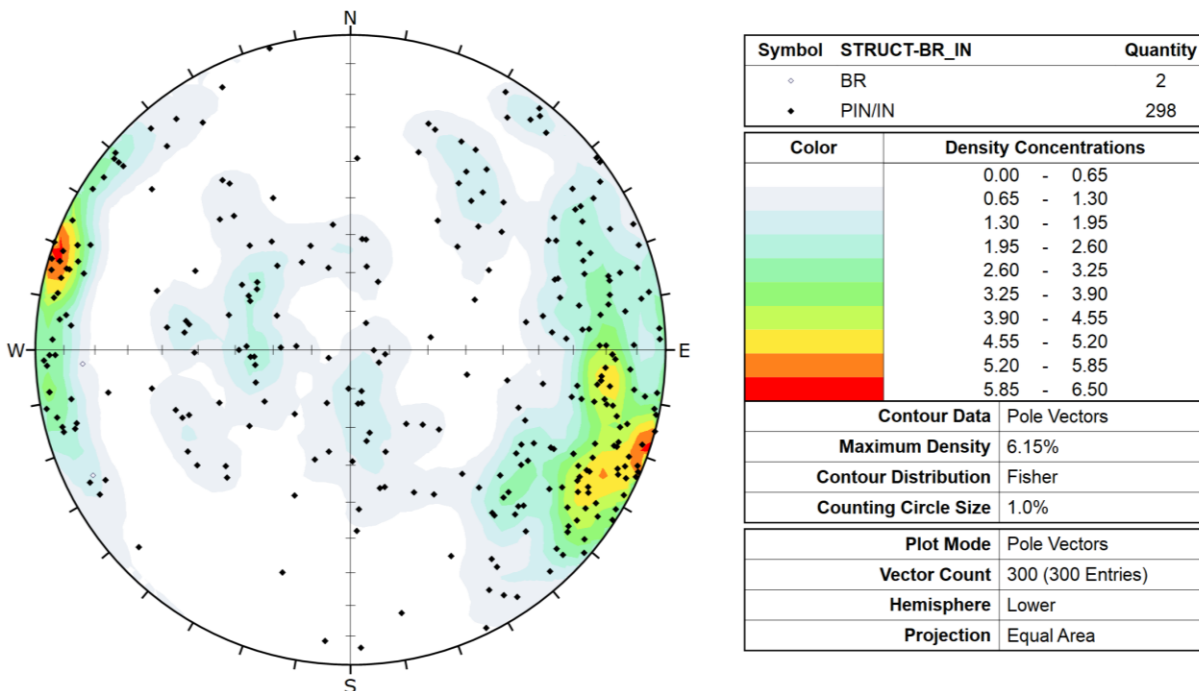
Contour Data	Pole Vectors
Maximum Density	4.82%
Contour Distribution	Fisher
Counting Circle Size	1.0%

Plot Mode	Pole Vectors
Vector Count (Weighted)	4318 (2162 Entries)
Terzaghi Weighting	Minimum Bias Angle 15°
Hemisphere	Lower
Projection	Equal Area

Figure 31: Stereonets showing orientation information for Joints (JN). Top: All data – poles and contours, unweighted (n = 2162). Open symbols identify broken Joints (JN-BR) and filled symbols identify partially intact/intact Joints (JN-PIN/IN). Bottom: All Joint data, Terzaghi-weighted contours (n = 4318).

A total of 331 veins were logged in IG_BH04. They are distributed along the majority of the length of the borehole except the upper approximately 75 m (Figure 27). The stick plot of vein occurrences highlights the observation that their distribution is generally coincident with peaks in the fracture frequency along the borehole, with distinct higher density intervals around 100 m, 575 m, 750 m, and between 950 and 975 m along the length of the borehole. A total of 278 veins (85 %) were identified in geological core logging. The majority of the veins (328; 99 %) were logged as intact or partially intact and the remaining three vein occurrences were logged as broken. 145 vein occurrences (52 %) were confidently associated with mineral phases. In the remaining 133 core logged vein occurrences, as well as in 53 televiewer only logged vein occurrences, an infilling mineral was not identified with certainty. The main mineral infilling phases identified include, quartz in 82 veins (25 %; Figure 30c), followed by chlorite in 37 veins (11 %), and epidote in 29 veins (9 %; Figure 30d). In addition, a 'granitic' assemblage of alkali feldspar +/- plagioclase +/- quartz with lesser biotite was identified in 13 veins (4 %), and calcite in 11 veins (3 %; Figure 30d). In addition, pyrite was identified in two veins (<1 %). Logged vein thicknesses range between hairline (sub-mm) and 5 cm.

A total of 300 of the 331 veins (91 %) were successfully oriented. Figure 32 presents the unweighted and weighted stereonet for all oriented veins. One main pole cluster crosses the perimeter of the stereonet and corresponds to vertically-oriented veins that strike north-northeast. Lesser pole clusters indicate gently to moderately inclined veins that dip east and north, and moderately to steeply-inclined veins that dip southwest. In the Terzaghi-weighted dataset, the dominant pole cluster migrates away from the perimeter to define a set of steeply inclined veins that dip east-southeast.



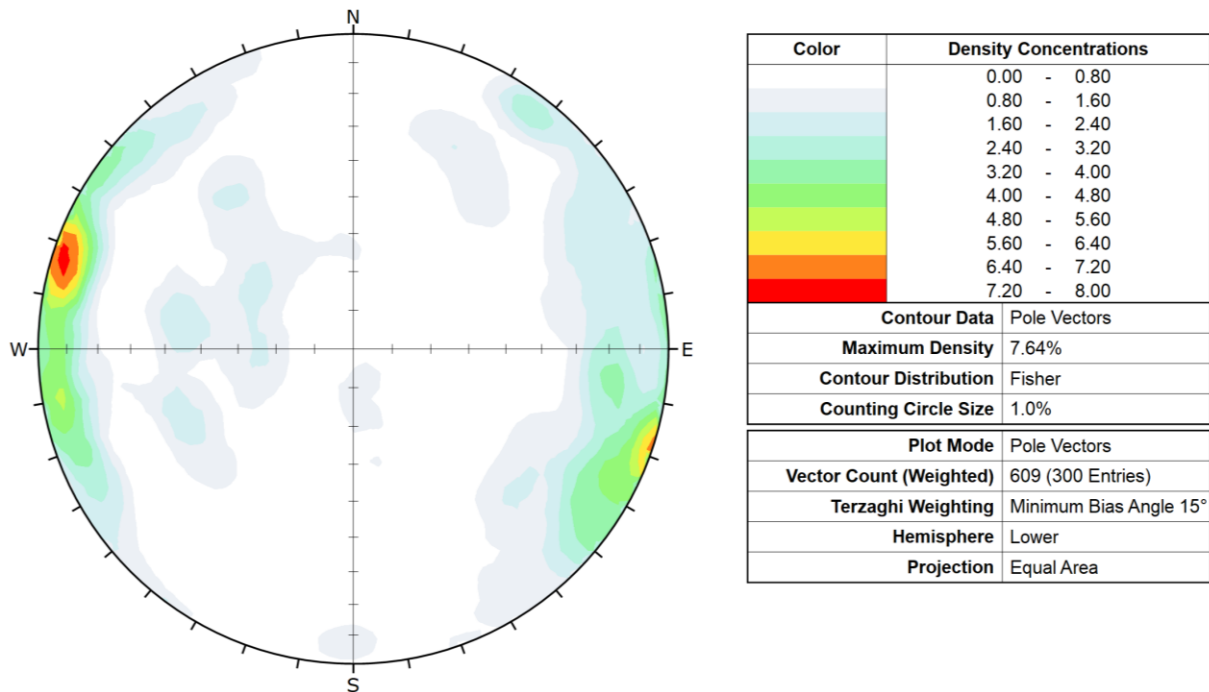


Figure 32: Stereonets showing orientation information for all Veins (VN). Top: All data – poles and contours, unweighted (n = 300). Open symbols identify broken Veins (BR) and filled symbols identify partially intact/intact Veins (PIN/IN). Bottom: All Vein data, Terzaghi-weighted contours (n = 609).

Faults include features interpreted to have resulted from brittle deformation and exhibit some evidence of displacement. A total of 8 faults were logged in IG_BH04. The stick plot highlights the observation that faults primarily cluster at approximately 575 m, and with a few additional occurrences in the lower 200 m of the borehole (Figure 27). Logged fault thickness ranges from less than one cm to 10 cm. Geological aperture ranges between zero and 2 cm. Examples of faults encountered in IG_BH04 are shown in Figure 30, including a mm-scale, quartz-filled, discrete fault plane (Figure 30e), and a cm-scale fault zone exhibiting the presence of broken rock and soft clay gouge (Figure 30f). The most common secondary mineral phases identified were the aforementioned clay gouge or broken rock in four faults (50 %), chlorite in three faults (38 %), quartz in two occurrences (25 %), epidote with calcite in one occurrence (13 %) and iron oxide stain in one fault (13 %).

A total of six faults were observed only in geological core logging (75 %) and the remaining two (25 %) were observed only in televiewer. Two of the eight faults, both identified in core logging, were identified as intact. The remaining logged faults were identified as broken. One additional feature, a six cm wide broken core zone with secondary iron stain and calcite infill intersected at 277 metres along the borehole, was identified in both core logging and televiewer logging, and is included in the presentation of oriented faults.

Figure 33 presents the unweighted stereonet for all eight oriented faults and the single broken core zone. Poles to the two faults logged as intact are both steeply-inclined and dip to the northeast and northwest. The rest of the faults, logged as broken, are predominantly moderately inclined and dip northwest to north. One additional broken fault is sub-horizontal. The broken core zone is moderately inclined and dips west-northwest.

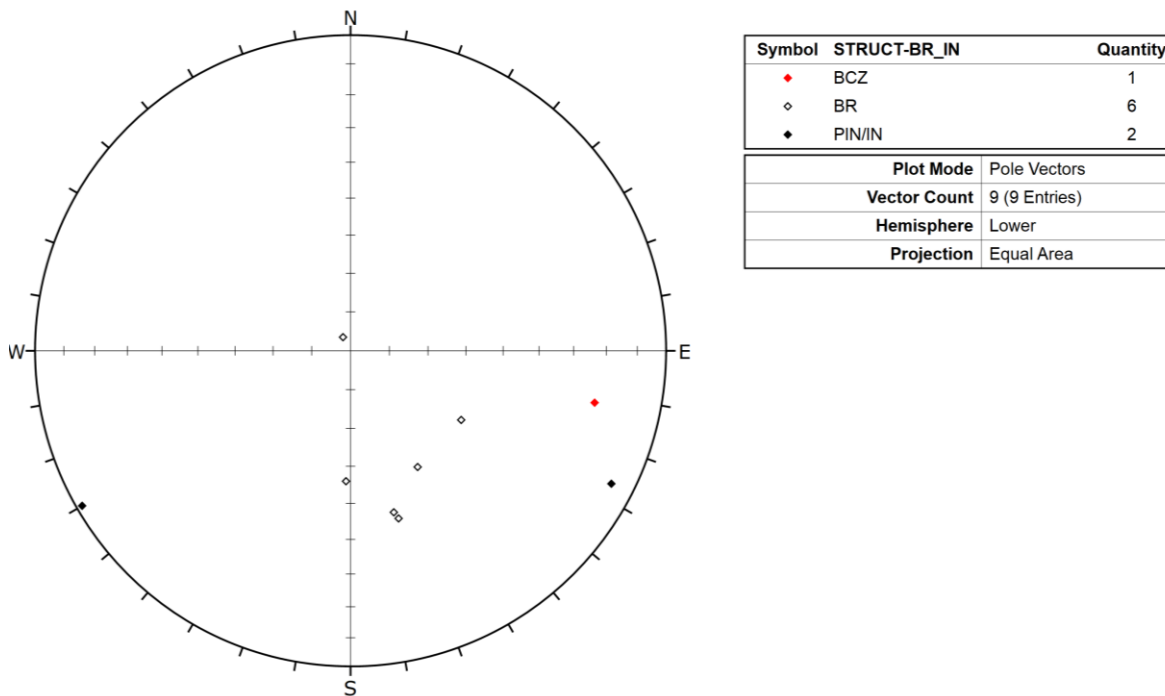


Figure 33: Stereonets showing orientation information for Faults (FLT; $n = 8$) and a Broken Core Zone (BCZ; $n = 1$). Open black symbols identify poles to broken Faults (BR) and filled black symbols identify poles to partially intact/intact Faults (PIN/IN). The red symbol identifies the pole to the Broken Core Zone.

Broken vs Intact or Partially Intact Structures

During the geological core logging, naturally occurring fractures were categorized as being broken (BR) when the core was physically broken into separate pieces at the location of the logged structure. Otherwise, they were categorized as intact (IN) or partially intact (PIN) where complete or partial cohesion was maintained along the logged structure. Of the 2468 oriented fractures, 180 (7 %) were logged as broken (Figure 36) and 2288 (93 %) were logged as intact or partially intact (Figure 34). This categorization is based on a visual assessment of core condition when the core is removed from the barrel and initially examined. As mentioned earlier in the discussion of joints, which includes the majority of broken fractures, most of the adjacent broken fracture planes could be physically fit back together with no visible geological aperture. Therefore, the broken characteristic alone does not imply any direct relationship to the potential for a fracture to be hydraulically conductive. This categorization also does not include any judgement on whether or not the drilling activity itself may have induced the break. The primary difference between the distribution of poles to fractures logged as broken versus intact (or partially intact), (comparing Figure 34 with Figure 35), is that broken structures tend to have gentler dips while intact structures tend to have subvertical dips.

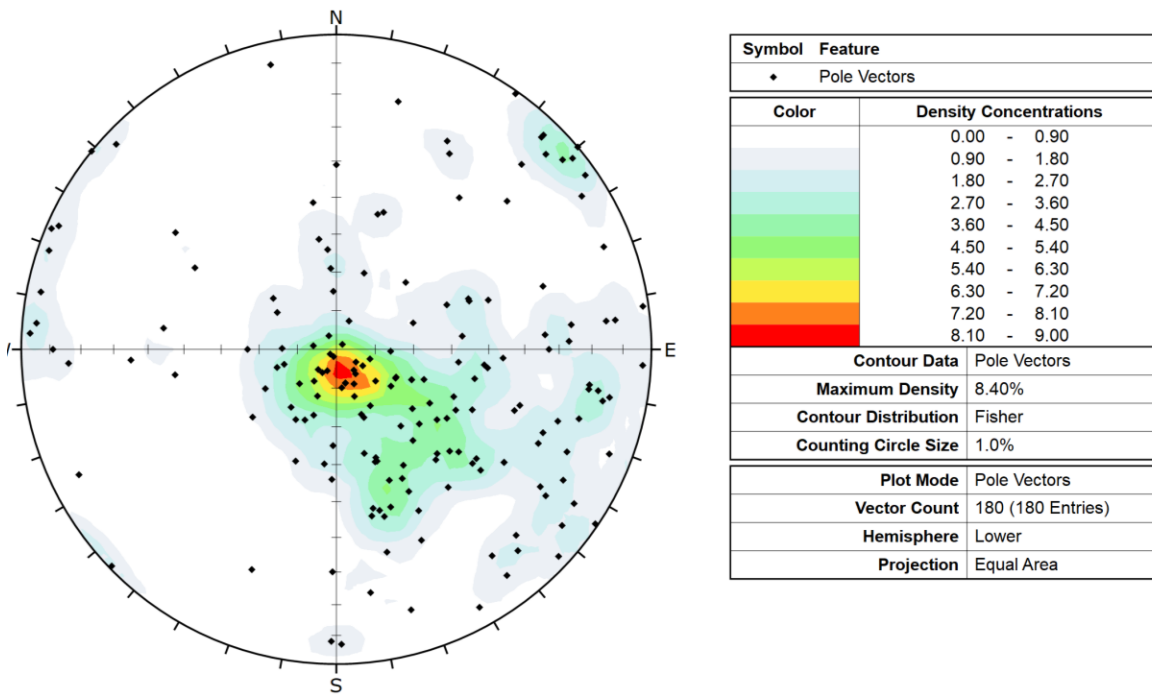


Figure 34: Stereonet plot showing poles to all fracture planes logged as broken during geological core logging, with unweighted contours (n = 180).

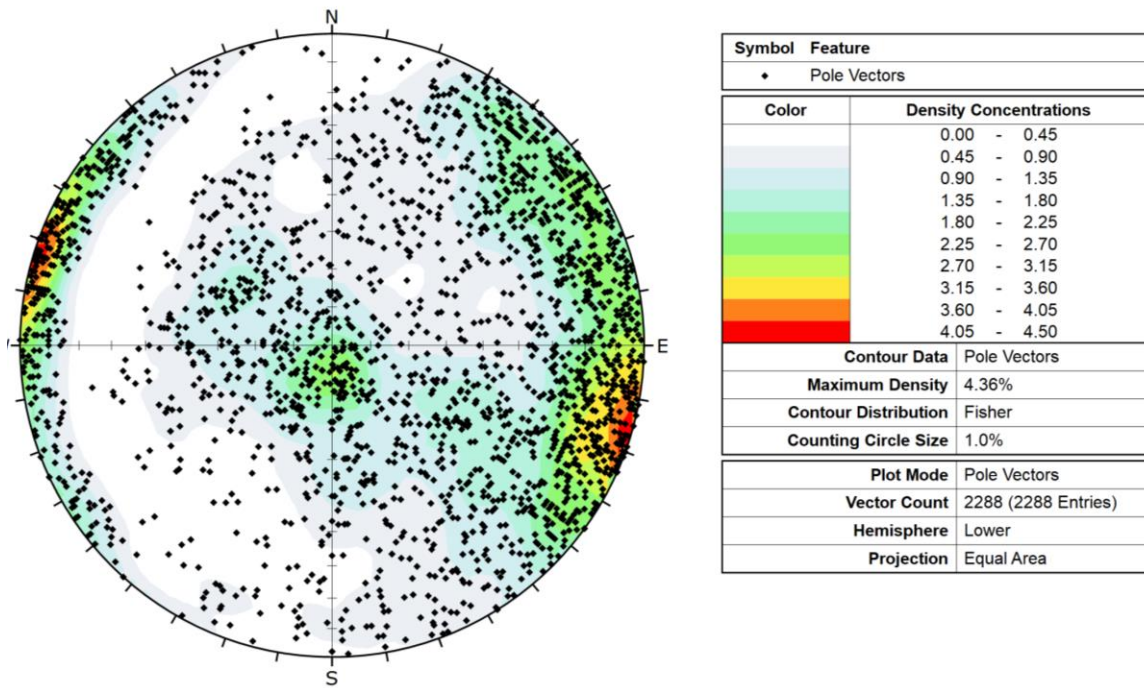


Figure 35: Stereonet plot showing poles to all fracture planes logged as intact or partially intact, with unweighted contours (n = 2288).

3.2.4.2 Interpreted Fracture Sets

Figure 36 presents the distribution of fracture poles and contoured stereographic distribution of poles to all logged fractures (joints, veins, faults, $n = 2468$) in order to assess for the presence of visible pole clusters that may define fracture sets in IG_BH04. These identified fracture sets can be compared with fracture sets identified in other boreholes, and also with surface mapped fracture and interpreted fracture (lineament) orientations, to provide guidance in developing three-dimensional fracture network models. Shear zones have not been included in this assessment.

Based on visual assessment of pole clusters and using a contour density cut-off of 1 % from the Terzaghi-weighted dataset as a guide, five clusters labelled (i) to (v) were initially identified in IG_BH04. Expert judgement was also employed to refine boundaries between pole clusters. These clusters are outlined on the stereonet of unweighted poles to all fractures (upper stereonet plot in Figure 36), and include:

- a pole cluster that overlaps the centre of the stereonet to define a subhorizontally-oriented to moderately inclined, east-southeast-dipping fracture set (Cluster i - red symbols in Figure 36 top stereonet);
- a pole cluster that defines a steeply inclined fracture set dipping east to southeast (Cluster ii - green symbols in Figure 36, top stereonet);
- a pole cluster that defines a steeply inclined fracture set dipping west to northwest (Cluster iii - orange symbols in Figure 36, top stereonet);
- a pole cluster that defines a steeply inclined fracture set dipping northeast (Cluster iv - blue symbols in Figure 36, top stereonet);
- a pole cluster that defines a steeply inclined fracture set dipping southwest (Cluster v - yellow symbols in Figure 36, top stereonet);

The remaining unclustered poles are not assigned to any particular possible fracture set and are therefore assigned to an additional random set.

The same five pole clusters are also outlined on the unweighted and Terzaghi-weighted contour plots (middle and bottom images in Figure 36, respectively). The Terzaghi-weighted plot de-emphasizes the shallower-dipping pole clusters and emphasizes the steeply inclined pole clusters. Notably, the Terzaghi-weighted contours, relative to the unweighted contours, also emphasize that the highest density regions of all pole clusters except (i) are adjacent to the perimeter of the stereonet, providing some indication that the steeply inclined and oppositely-dipping pole clusters, (ii and iii) and (iv and v), likely represent members of the same near-vertical to vertically-oriented fracture sets.

As a final interpretation of fracture sets for IG_BH04, pole cluster (i) is assigned to Fracture Set 1 defined by subhorizontally-oriented to moderately inclined, east-southeast-dipping fractures, pole clusters (ii) and (iii) are combined and assigned to Fracture Set 2 defined by near-vertical north-northeast-striking fractures, pole clusters (iv) and (v) are combined and assigned to Fracture Set 3 defined by near-vertical northwest-striking fractures. These final Fracture Set IDs are labelled on the unweighted and Terzaghi-weighted contour plots in Figure 36 and summarized in Table 8. It should be noted that there remains some uncertainty in the overall assignment of fracture sets because a large number of poles remain outside of any assigned fracture set regions.

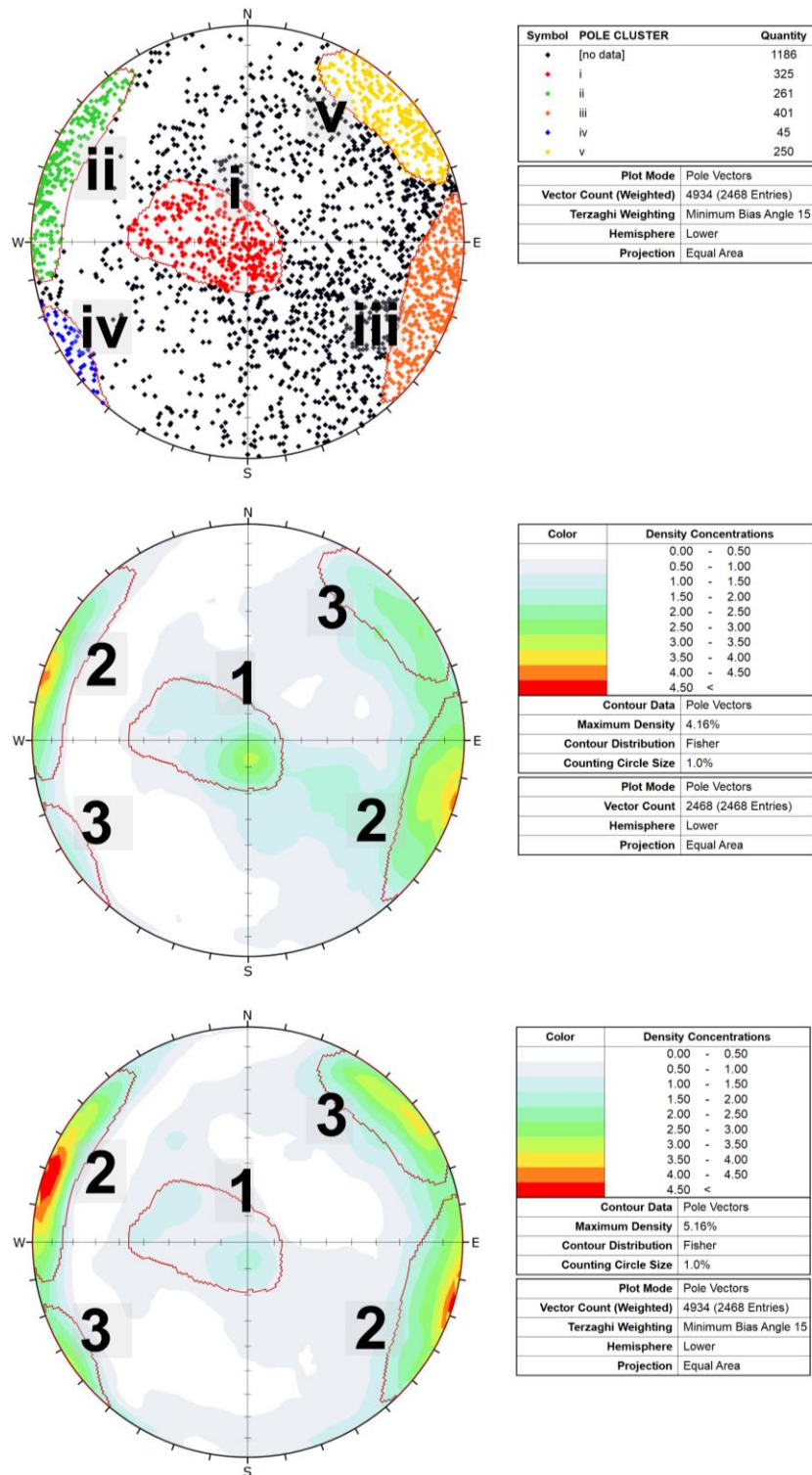


Figure 36: Stereonets of all oriented fractures, including all joints, veins and faults. Top: All fractures – poles, unweighted (n = 2468). Identified pole clusters are colour-coded to highlight their distribution. Middle: All fractures – contours (n = 2468), unweighted. Bottom: All fractures – contours, Terzaghi-weighted (n = 4934). Middle and bottom stereonet are overlain by final fracture set interpretation. See text and Table 9 for additional summary.

Table 8: Summary of interpreted fracture sets in the borehole. Presents the general description of the orientation with a mean dip and dip direction.

Fracture Set ID	Orientation	Mean Dip / Dip Direction	Fracture Count
1	Subhorizontal to moderately inclined set, dipping east-southeast	10 / 096	325
2	Near-vertical set, striking north-northeast	87 / 108	661
3	Near-vertical set, striking northwest	86 / 233	295

Regarding the relationship between fracture sets and ductile structures, only a limited number of foliation measurements were made in IG_BH04 and so no meaningful correlation is suggested. Shear zones range between subhorizontal, and overlapping with Fracture Set 1, to steeply inclined, and broadly northwest-dipping, and partially overlapping with Fracture Set 2 (Figure 33). The similarity of orientation between the brittle fracture sets and the ductile structures suggests that pre-existing ductile fabrics exerted some control on the development of brittle structures in the rock mass, in particular Fracture Set 1.

Regarding the relationship between fracture sets and types of brittle structures, the large number of joints relative to veins and faults is consistent with the presence of joints in all three identified fracture sets. Poles to veins cluster prominently in the same orientation as Fracture Set 2, and less so in relation to Fracture Set 1 and Fracture Set 3. In the Terzaghi-weighted vein dataset the relationship to Fracture Set 1 is further reduced, while the relationship to Fracture Set 3 is slightly enhanced (Figure 36). Poles to logged faults, as shown in Figure 33, overlap in distribution with Fracture Sets 1 and 2, and also fall outside of any defined Fracture Set cluster.

Stick plots of the distribution of each fracture assigned to a fracture set, as well as unassigned random fractures, are plotted adjacent to the per metre fracture frequency of IG_BH04 (Figure 37). This presentation aids in assessing the degree of clustering evident by fracture set. Set 1 fractures are distributed along the entire length of the borehole with clustering evident in the same locations as prominent peaks in the fracture frequency. There is a noticeable increase in number of Set 1 fractures from ground surface to approximately 150 m along the borehole, as well as the bottom 100 m of the borehole length. These increases in Set 1 fractures are broad and tend to be consistent with an overall increase in the fracture frequency data. A well defined increase in Set 1 fractures is also present between 575 m and 600 m depth along borehole, corresponding a discrete peak in the fracture frequency data. Set 2 fractures are irregularly distributed along the majority of the borehole, with slightly higher fracture frequency around 100 m, around 475 m, and from approximately 575 to 800 m along the borehole. There is also a noticeably higher frequency of Set 2 fractures below 900 m along the borehole. Set 3 fractures are relatively evenly distributed along the length of the borehole with the exception of a noticeable gap in frequency between approximately 150 and 300 m along the borehole. The unassigned random fractures (1413/2079; 68%) are present along the entire length of the borehole.

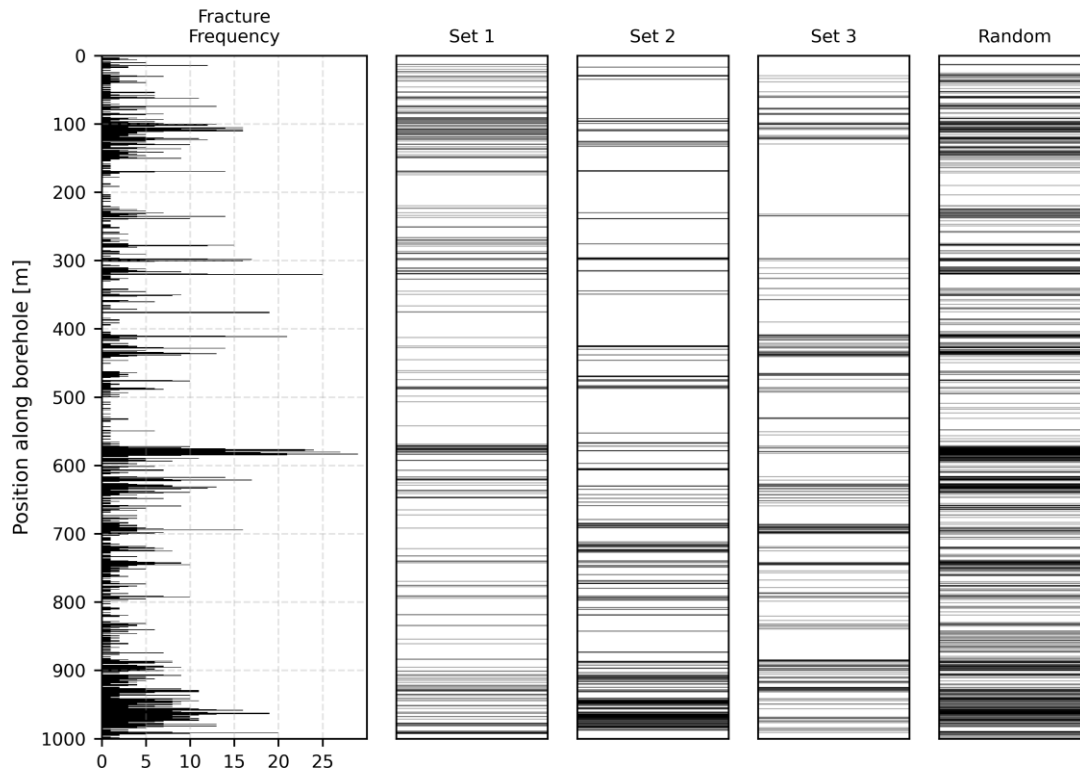


Figure 37: Summary log showing the frequency per metre of all brittle structures (left) in comparison to stick plots that show the distribution of all fractures assigned to defined fracture sets 1, 2, and 3, as well as unassigned random fractures. It is understood that there is some uncertainty in the present assessment, including based on the relatively large number of fractures remaining unassigned. The fracture set interpretation will continue to be refined as other boreholes are drilled in different directions.

3.2.4.3 Fracture Infill Minerals

Fracture infill, or secondary, minerals are observed in association with all fracture types in IG_BH04, and include surface staining or hairline infilling in joints, mineral lineations on fault surfaces and vein infilling. Of the 2468 oriented planar fractures, 1723 (70 %) were identified during geological core logging to host infilling minerals. The most prominent infill mineral phase identified in IG_BH04 is quartz, which occurs both as the sole mineral phase and in association with some occurrences of chlorite, iron oxide stain, calcite and epidote. The discussion below focuses on the orientation and distribution of these mineral phases. Stick plots of the distribution of each of these infill mineral types are plotted adjacent to the per metre fracture frequency of IG_BH04 in Figure 38.

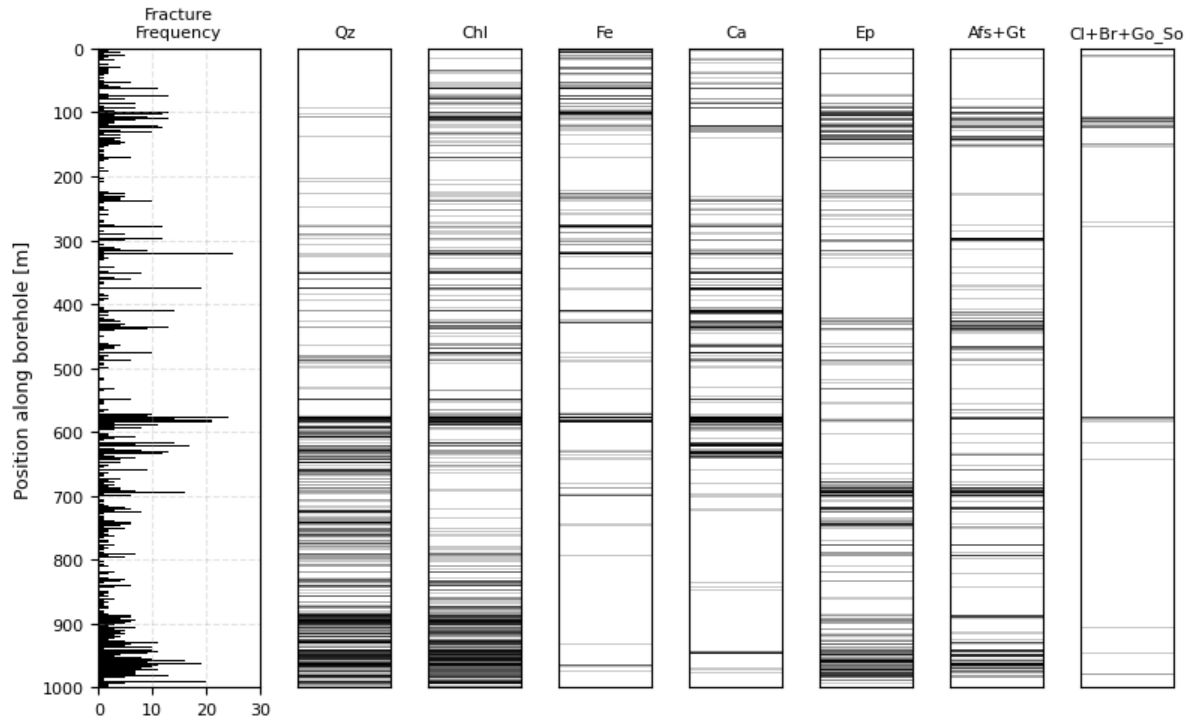


Figure 38: Summary log showing the frequency per metre (Fracture Freq.) of all brittle structures (left) in comparison to stick plots that show the distribution of the most common infill mineral phases including quartz (Qz), chlorite (Chl), iron oxide stain (Fe), calcite (Ca), epidote (Ep), a granitic (Gt) assemblage that includes some combination of alkali-feldspar (Afs) with quartz, plagioclase and biotite, and, fractures that exhibit either clay (Cl), broken rock (Br), or soft clay gouge (Go_So).

Quartz +/- chlorite, calcite, iron oxide stain, epidote, or rarely pyrite, was logged in 602 of the 2468 (24%) oriented fractures (Figure 39). One prominent pole cluster of quartz +/- accessory mineral-filled fractures falls within Fracture Set 2. To a lesser extent, Fracture Sets 1 and 3 are also evident in the quartz-filled fracture data set. Fractures with quartz +/- accessory mineral infill are distributed along the entire length of the borehole, except in the upper approximately 100 m. The frequency of quartz infill is significantly increased below approximately 575 m along borehole (Figure 38).

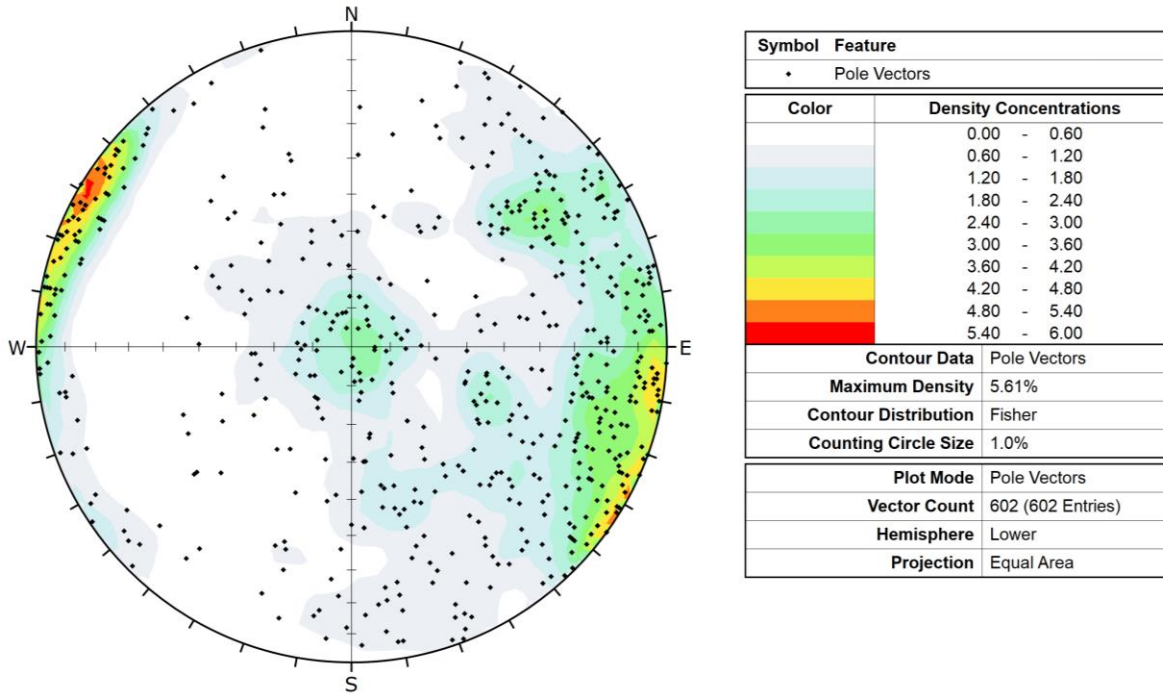


Figure 39: Stereonet plot showing poles to all fracture planes logged with quartz +/- chlorite, calcite, iron oxide stain, epidote, or rarely pyrite (n = 602).

Chlorite +/- calcite, epidote, quartz, iron oxide stain, or rarely pyrite is identified as an infill mineral phase in 590 of the 2468 (24 %) oriented fractures (Figure 40). Pole clusters of chlorite +/- accessory mineral-filled fractures fall within all three defined fracture sets. The distribution of chlorite-filled fractures is relatively consistent along the length of the borehole with slight increases in concentration at around 100 m, 575 m, and below 850 m (Figure 38).

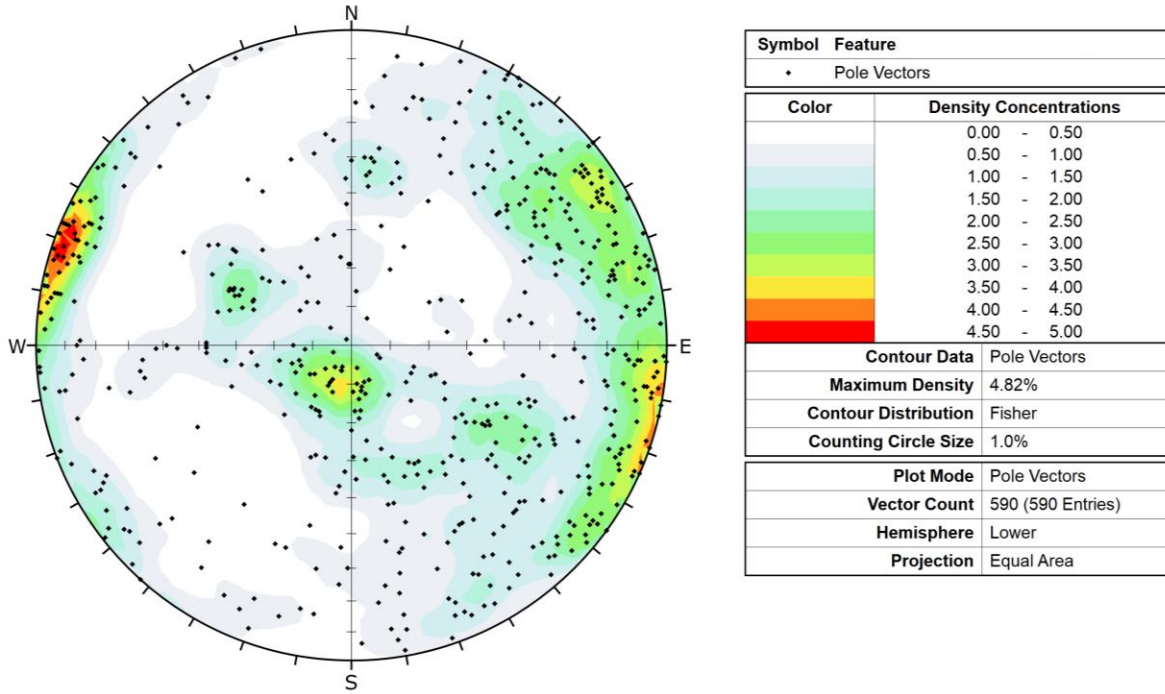


Figure 40: Stereonet plot showing poles to all fracture planes logged with chlorite (n = 590)

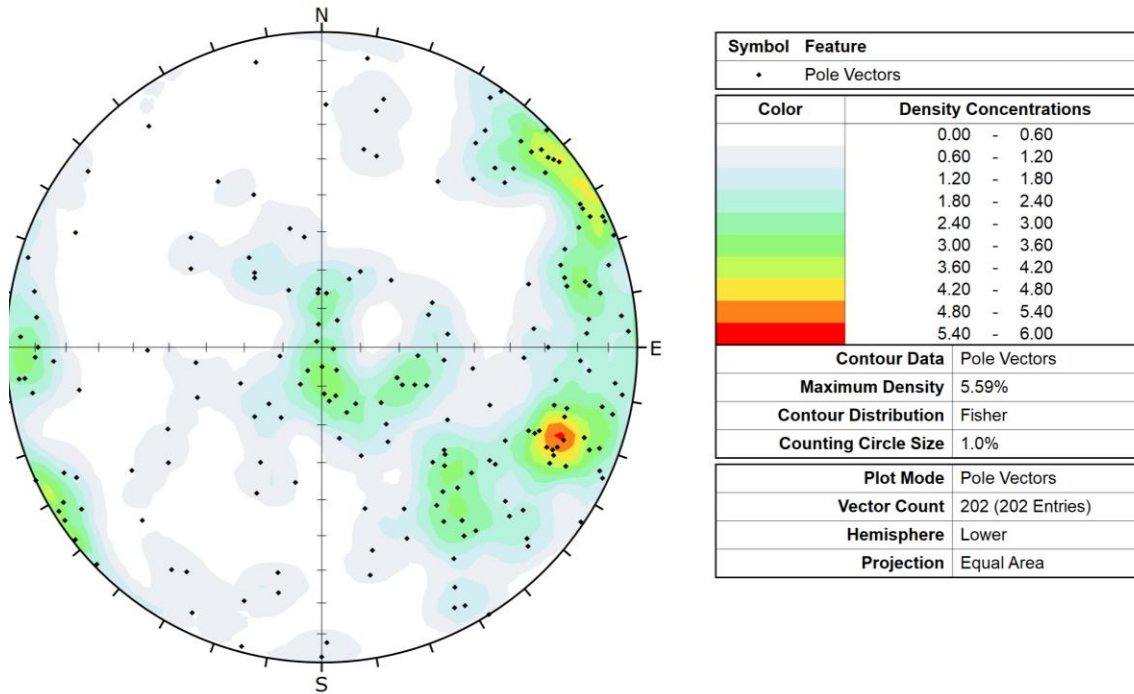


Figure 41: Stereonet plot showing poles to all fracture planes logged with iron staining (n = 202).

An iron oxide mineral, potentially hematite, is present primarily as a stain but locally as a much thicker fill on 434 of the 2079 (21 %) oriented fractures (Figure 41). The two most prominent pole clusters of iron oxide-filled fractures fall within Fracture Set 2 and Fracture Set 3, and a lesser pole cluster overlaps with the region of Fracture Set 1. The distribution of iron oxide-stained fractures is heterogeneous along the borehole with increased frequency in the upper 100 m, between 250 and 450 m, and around 575 m. Below 575m there is a marked decrease in frequency of iron oxide-filled fractures (Figure 38).

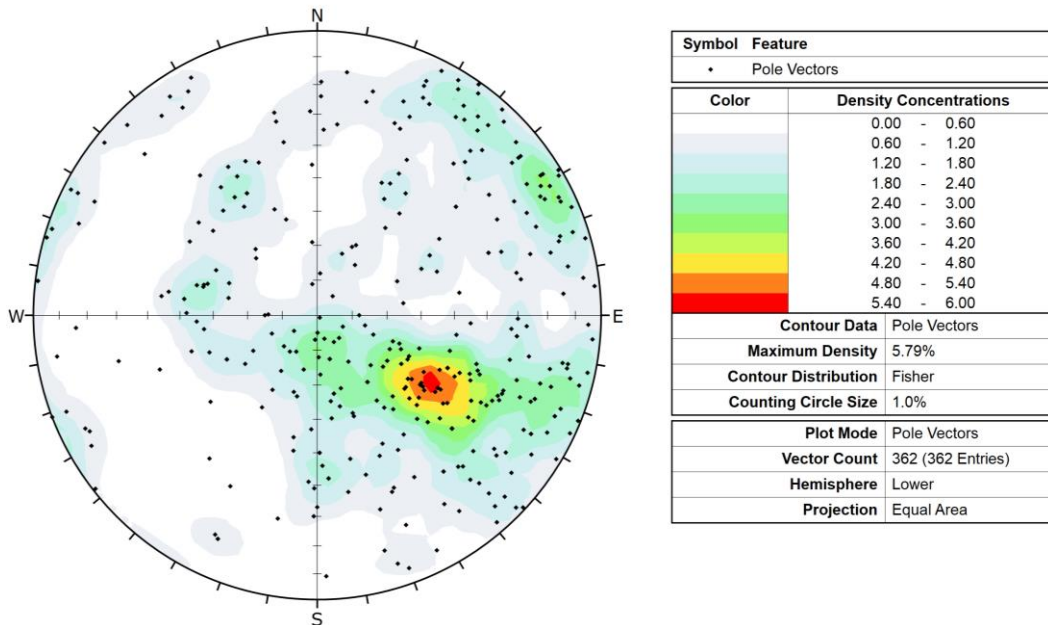


Figure 42: Stereonet plot showing poles to all fracture planes logged with calcite (n = 362).

Calcite is identified as a mineral infill phase on 362 of the 2468 (15 %) oriented fractures. The distribution of the poles to calcite-filled fractures exhibits one relatively prominent cluster that falls between Fracture Set 1 and Fracture Set 2. Less prominent pole clusters overlap with all three fracture sets (Figure 42). The distribution of calcite-filled fractures is heterogeneous along the borehole with a varying, but relatively high, frequency in the upper 125 m and between 250 and 625 m, and a marked decrease with increasing position down to the bottom of the borehole (Figure 38).

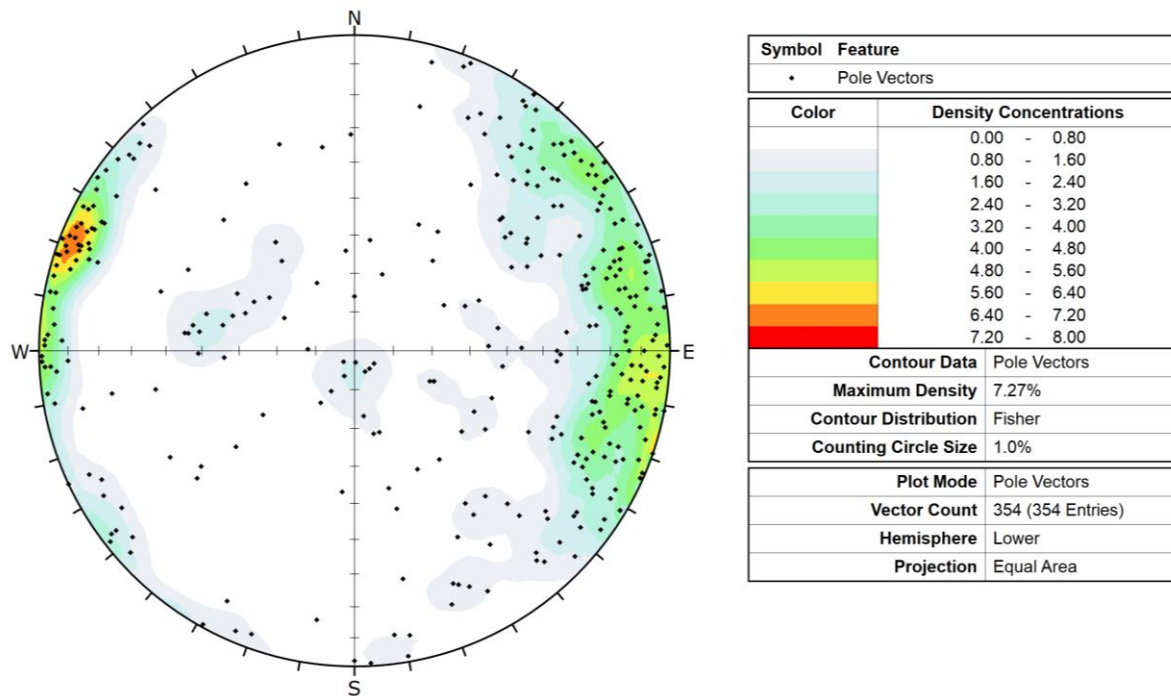


Figure 43: Stereonet plot showing poles to all fracture planes logged with epidote (n = 354).

Epidote is identified as a mineral infill phase on 354 of the 2468 (14 %) oriented fractures. The distribution of poles to epidote-filled fractures exhibits one prominent pole cluster that coincides with Fracture Set 2, and to a lesser extent a cluster of poles also coincides with Fracture Set 3 (Figure 43). Epidote-filled fractures are relatively uniformly distributed along the entire length of the borehole, with slightly increased intensity around 100 m and 700 m, and again below 900 m (Figure 38).

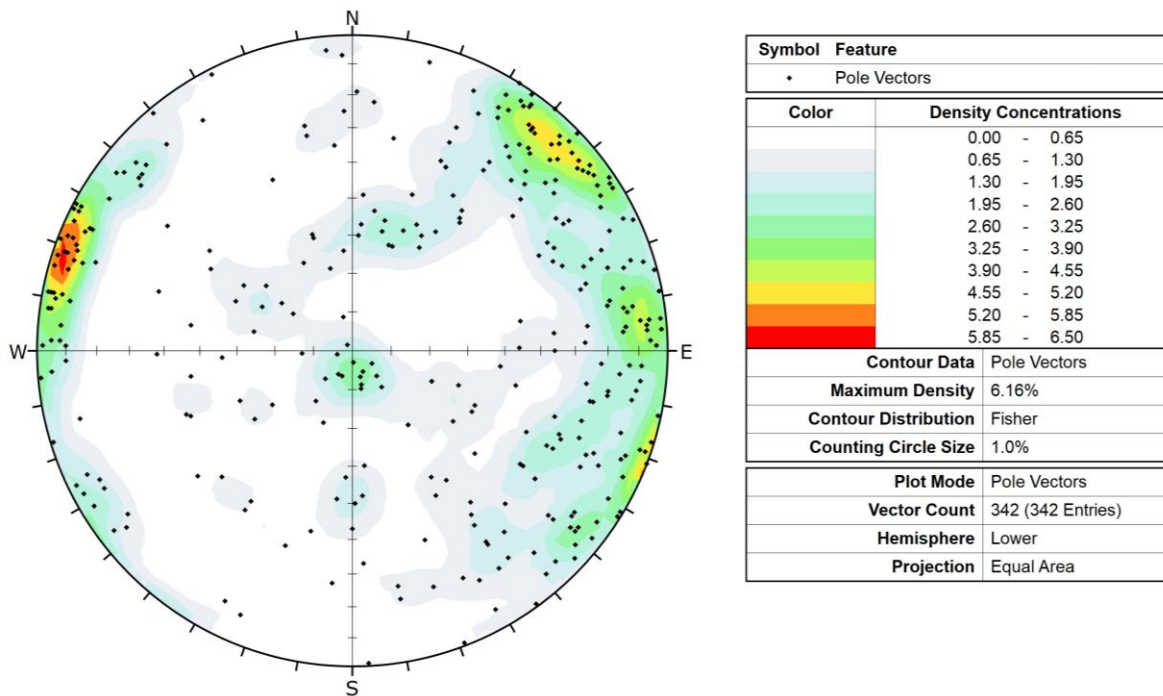


Figure 44: Stereonet plot showing poles to all fracture planes logged with granitic infill, including alkali-feldspar +/- quartz, plagioclase and biotite (n = 342).

A granitic infill assemblage characterized by alkali-feldspar +/- quartz, plagioclase and biotite, and lesser muscovite, including some coarser-grained pegmatitic occurrences, is identified in 342 of the 2468 (14 %) oriented fractures. Two prominent cluster of poles to granitic-filled fractures overlap with Fracture Set 2 and Fracture Set 3, while a lesser pole cluster overlaps with Fracture Set 1 (Figure 44). Granitic-filled fractures are relatively heterogeneously distributed along the entire length of the borehole (Figure 38).

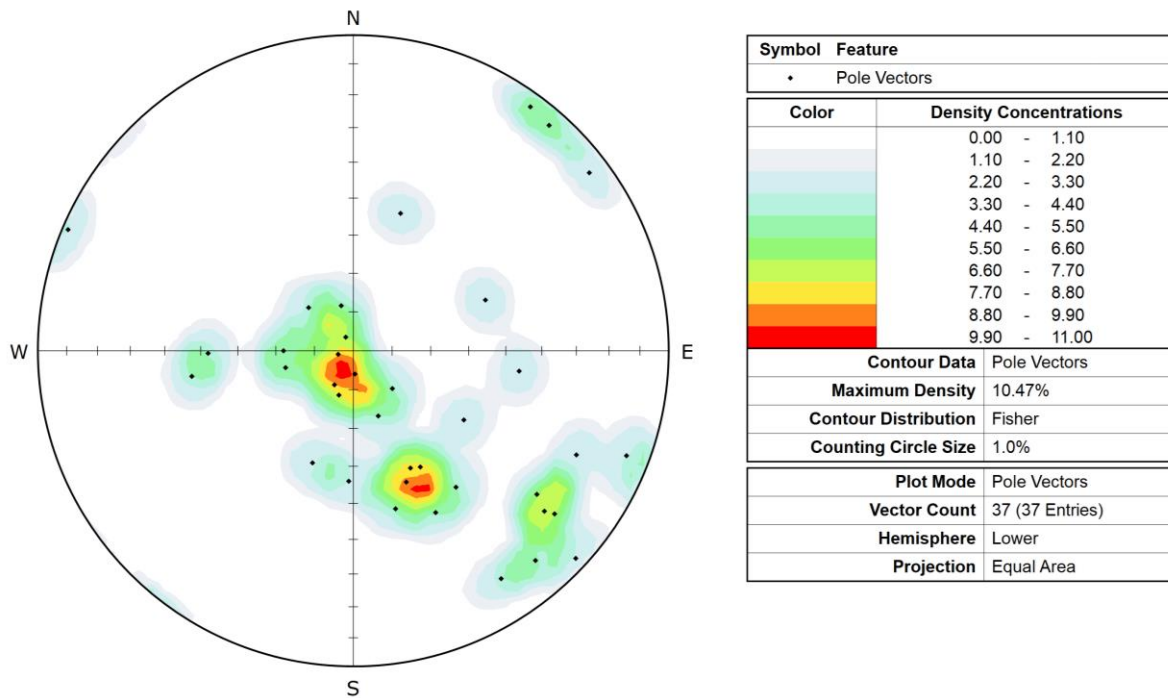


Figure 45: Stereonet plot showing poles to all fracture planes logged with clay, broken rock, or soft gouge (n = 37).

Fractures infilled with clay, soft or stiff clay gouge, or broken rock, were logged in 37 of 2468 (1 %) oriented fractures. One prominent pole cluster defines gently inclined fracture planes that dip east or north (Figure 45), overlapping Fracture Set 1. Less pole clusters overlap Fracture Set 2 and Fracture Set 3. These clay or broken rock-filled fractures are localized at around 100 m, 250 m, 600 m, and below 900 m, along the borehole (Figure 38).

A total of 745 fractures (30%) have no associated infill mineral phase assigned to them. This includes 113 fractures that were only identified in the televiewer datasets and could not confidently be assessed for infill mineral type, even if present (Figure 46). The poles to fractures with no assigned infill minerals exhibit one prominent cluster that overlaps with Fracture Set 2. Less prominent pole clusters overlap with Fracture Set 1 and Fracture Set 3.

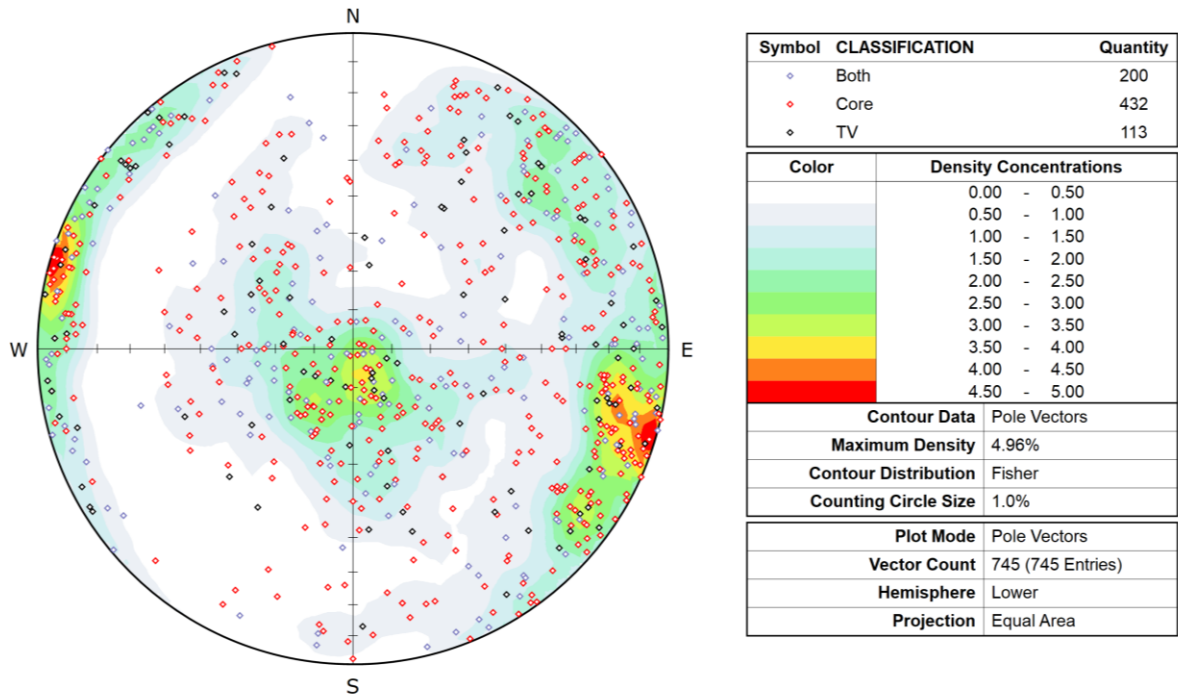


Figure 46: Stereonet showing poles to all fractures logged as having no identifiable mineral infill phase. Fractures logged in ‘televiewer’ (TV) datasets only, geological ‘core’ logging only (Core), or identified in ‘both’ datasets, are distinguished (n = 745).

3.2.5 Structural Unit Classification

Structural units (SU) have been defined to capture the general variation in fracture frequency along the length of the borehole. Boundaries between structural units were defined primarily on the basis of broad changes in slope visible in the cumulative fracture frequency curve. This curve was derived using the fracture dataset (i.e., joints, veins, and faults, including broken and intact/partially intact structures) and is presented in Figure 47. The per metre mean fracture frequency and per metre aperture sum, derived using the same dataset, is also reported as an additional indicator of these same general trends. A total of six SUs are defined for IG_BH04 (Figure 47). Stereonets of fracture orientation data for each defined SU are included in Appendix E:.

Structural unit 1 (SU1) extends from the ground surface (0 m) to 98.75 m along borehole (Figure 47). This unit exhibits a slope in the cumulative fracture frequency curve that corresponds to an average fractures per metre of 2.33. As a result, this shallow portion of the borehole has a lower degree of fracturing than the adjacent SU2. The fracture frequency is not consistent throughout the unit, and ranges from metre-long intervals completely devoid of fractures and intervals up to 13 fractures per metre. There are 169 oriented fractures in SU1, including 164 joints and 5 veins (Appendix E:). Poles to these fractures predominantly overlap with Fracture Sets 1 and 3, and to a lesser extent Set 2.

Structural unit 2 (SU2) is a 54 m interval that extends from 98.75 m to 152.75 m along borehole. Over this relative short interval, SU2 is defined by a shallow slope in the cumulative fracture frequency curve, corresponding to a high degree of fracturing of the bedrock compared to the adjacent SU's above and below (Figure 47). SU2 has an average fracture frequency of 6.41 fractures per metre and exhibits high local variability in counts ranging between 0 and 20 fractures per metre. There are 229 oriented fractures in SU2, including 204 joints, and 25 veins (Appendix E:). Poles to these fractures overlap with all three defined fracture sets.

Structural unit 3 (SU3) comprises almost half of the borehole at 420 m in length, extending from 152.75 m to 572.75 m along borehole (Figure 47). This unit shows a steep slope in the cumulative fracture frequency curve corresponding to an overall low fracture frequency with an average of 1.76 fractures per metre. Despite the low average, the interval fracture frequency shows local variability ranging between 0 and 31 fractures per metre. These higher fracture peaks tend to only exist over very short distances (1 to 2 metres) and return to relatively sparsely fractured bedrock. There are 565 oriented fractures in SU3, including 528 joints, and 37 veins (Appendix E:). Poles to these fractures mainly overlap with Fracture Sets 2 and 3 as well as a wide range of fractures from the random set.

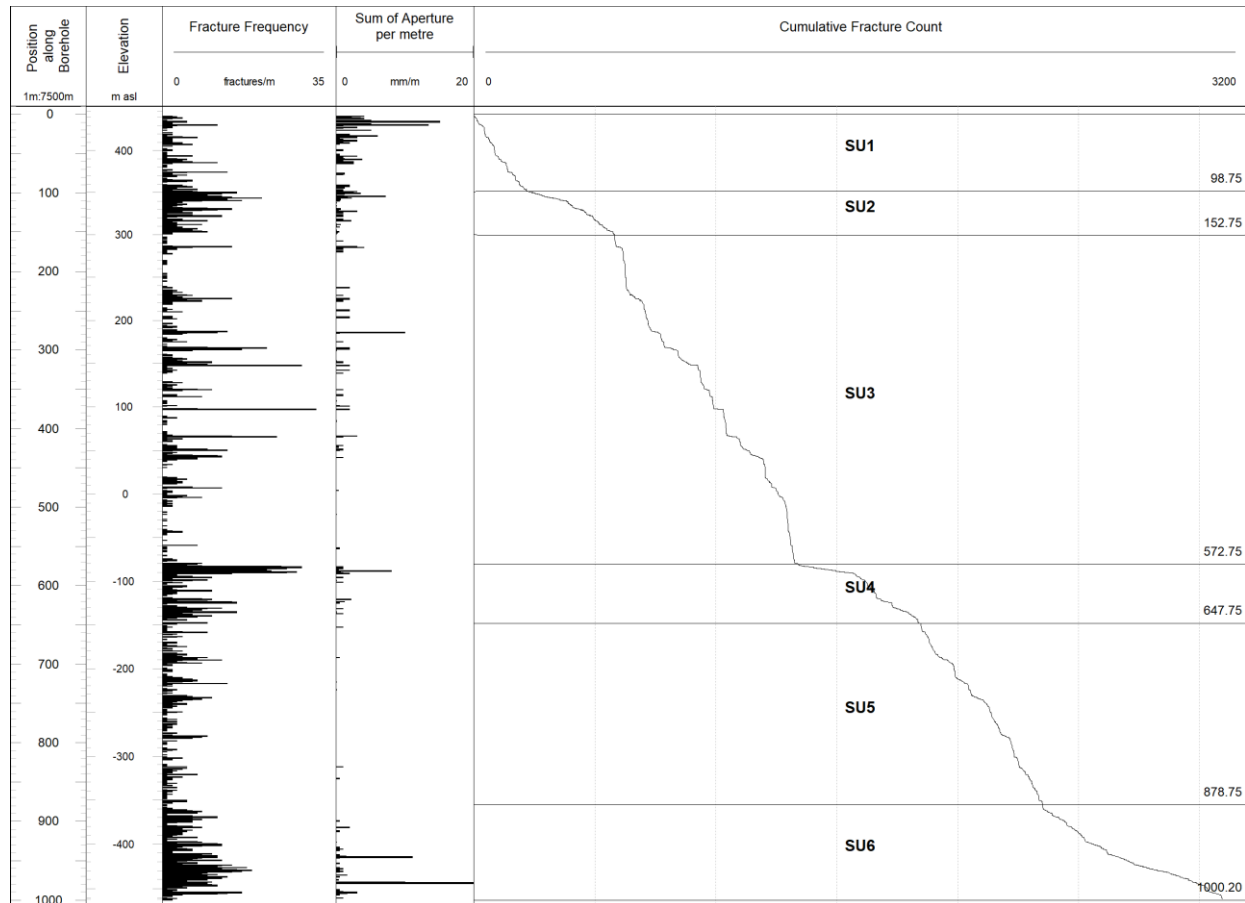


Figure 47: Per metre fracture frequency (left), the sum of aperture per metre (centre) and cumulative fracture frequency curve (right) showing vertical distribution of all logged joints, faults, and veins along the borehole. The cumulative fracture frequency curve shows changes in slope where boundaries in structural units (SU) are defined. Structural unit boundaries are marked on the figure, and their positions are described in Table 9.

Structural unit 4 (SU4) extends from 572.75 m to 647.75 m along borehole (Figure 47), with a length of 75 m. Over this relatively short interval, both the fracture frequency and cumulative frequency curves show a high amount of fracturing compared to neighbouring intervals in the borehole, with an average frequency of 6.57 fractures per metre and ranging between 0 and 28 fractures per metre. The upper portion of this SU4 interval shows a sharp change in the slope of the cumulative fracture frequency curve. This zone is marked by an abrupt increase in fracture frequency associated with the presence of a highly fractured amphibolite unit. There are 433 oriented fractures in SU4, including 392 joints, 37 veins, and only 4 faults (Appendix E:). Poles to these fractures are broadly spread within the SE quadrant, dipping moderately towards the NW.

These fractures tend to cluster tightly in an orientation consistent with the occurrence of a moderately dipping amphibolite unit. Fewer fractures also overlap with Fracture Sets 2 and 3. Structural unit 5 (SU5) extends from 647.75 m to 878.75 and represents a 231 m length along the borehole with a relatively low fracture intensity. The change in the slope of the cumulative fracture frequency curve is not well defined at 647.75 m transitioning from SU4 to structural unit 5 (SU5). The cumulative fracture frequency curve for SU5 is characterized by a steep slope reflecting a lower degree of fracturing of the bedrock. Overall, the fractures recorded appear to be uniformly distributed and the interval is characterized by an average frequency of 1.98 fractures per metre, ranging from 0 up to 13 fractures per metre. There are 411 oriented fractures in SU5, including 317 joints, 93 veins, and 1 fault (Appendix E:). The vast majority of poles to these fractures are high angle and overlap with defined Fracture Sets 2 and 3. The occurrence of Set 1 fractures is limited within this SU interval.

The lower portion of the borehole is defined as structural unit 6 (SU6) and extends from 878.75 m to bottom of hole at 1000.2 m along borehole (Figure 47). This unit has a length of 121.45 m. Both the fracture frequency and cumulative frequency curves show a high amount of fracturing compared to the shallower interval in the borehole, with an average frequency of 6.05 fractures per metre and ranging between 0 and 18 fractures per metre. The location of this SU interval in the borehole is approximately consistent with the lower rock unit interval, comprising a feldspar-phyric biotite granodiorite-tonalite as well as numerous thin amphibolites. There are 663 oriented fractures in SU4, including 557 joints, 103 veins, and 3 faults (Appendix E:). The majority of fractures within this SU interval are steeply dipping and mainly fall within Fracture Sets 2 and 3. There is a small cluster of fractures that are consistent with the subhorizontal orientation of Set 1.

As with the rock units defined previously, the criteria for defining the interpreted structural units may be modified once additional fracture data is collected in future boreholes. The framework presented here represents an interpretation based on general broad trends in the available data.

Table 9: Position ranges and standard statistics for fracture frequencies captured within the defined structural units (SU) within the borehole.

	<i>SU1</i>	<i>SU2</i>	<i>SU3</i>	<i>SU4</i>	<i>SU5</i>	<i>SU6</i>
<i>Position Range (m)</i>	0 – 98.75	98.75 – 152.75	152.75 – 572.75	572.75 – 647.75	647.75 – 878.75	878.75-1000.20
<i>Thickness (m)</i>	98.75	54	420	75	231	121.45
<i>Min (fractures/m)</i>	0	0	0	0	0	0
<i>Max (fractures /m)</i>	13	20	31	28	13	18
<i>Average (fractures /m)</i>	2.33	6.41	1.76	6.57	1.98	6.05
<i>Standard Deviation (fractures /m)</i>	2.62	4.66	3.54	7.27	2.33	4.25

3.2.6 High Fracture Frequency Intervals (HFFIs)

Along with the broad changes in fracture frequency that are used to define the SUs described above, additional discrete intervals of increased fracture frequency were also identified in IG_BH04. These occurrences are referred to as high fracture frequency intervals (HFFIs) and are defined as a cluster of fractures (i.e., faults, joints and or veins) that exceeds a minimum relative fracture intensity threshold along a distinct borehole length (see below for details of IG_BH04). The spatial distribution of fractures and their intensity over the length of the borehole provide meaningful justification for defining HFFIs within the subsurface. Within the boreholes, the HFFIs are primarily dominated by fractures that share similar orientations within a single fracture set (i.e., fracture corridor) or by fractures in a range of orientations (i.e., fracture swarm), and locally may also comprise few minor ductile shear zones. Fracture summaries presented in the previous sections

provide details on fracture sets, fracture types and fracture mineral infilling, which may contribute to the characterization of the HFFIs. At the end of this section, an attempt is made to broadly correlate the identified HFFIs with lineaments trends that were interpreted based on remote sensing data on the ground surface in proximity to IG_BH04 (DesRoches et al. 2018).

HFFIs were defined using a semi-automated approach applied to the borehole fracture frequency per metre log. To visualize contiguous zones of increased fracture intensity, the fracture frequency distribution was smoothed with a uniformly weighted moving average filter using the “uniform_filter1d” function from the SciPy processing package in Python (Virtanen et al. 2020). This filter is equivalent to a moving mean and is commonly applied to time-series data to smooth high-frequency data and enable detection of broader responses. This filter preserves the low-frequency components of the input data while high-frequency components are attenuated. The magnitude of the filter is defined by the uniform window size (w), which controls the degree of smoothing applied. In this study, a step size and window size of 1 m and 15 m, respectively, were defined.

The HFFIs are defined using the smoothed fracture frequency curve using two peak detection algorithms, “find_peaks” and “peak_widths” from the SciPy processing package (Virtanen et al. 2020). The peak detection algorithm finds all local maxima by simple comparison of neighboring values. A peak is defined as a local maximum where any sample whose two direct neighbours have a smaller amplitude. The difference in magnitude with the neighbouring values is defined by a threshold value in the algorithm, such as the peak prominence. The prominence of a peak measures the magnitude of the peak relative to the neighbouring values and is defined as the vertical distance between the peak and its lowest neighbouring value. Using the smoothed fracture frequency curve as input data, the peak prominence threshold was set at four for this study.

Once peaks are defined, the peak widths are based on the anomaly width at a specified distance between the peak maxima and the lowest neighbouring value (i.e., along the prominence height). In this study, a relative height of 0.5 is used at a threshold to extract the width of the peak.

Figure 48 presents the HFFI results from the fracture frequency data in IG_BH04. Based on the smoothed fracture frequency data and the peak detection analysis, six HFFIs have been defined. Figure 48 shows the cumulative counts of fractures along the length of the borehole and displays the fracture frequency per metre and the filtered fracture frequency. The cumulative curve, along with these data plots show evidence of discrete intervals of increased fracture intensity. Stick plots of joints, veins and faults display the location of each individual fracture type along the borehole length. A summary of the HFFIs for IG_BH04 are presented in Table 10, including dominant fracture orientation(s), rock type(s) present, fracture set association, alteration, and fracture infill characteristics.

Although the results presented in Figure 48 are visually verified to be ideal candidates for HFFI interpretation, changing the peak detection algorithm input parameters can result in other possible HFFI outcomes. For example, reducing the peak prominence threshold or the applied window size in the smoothing function results in an increase in the number of peaks identified from the data. Conversely, increasing these parameters reduces the number of peaks identified. Similarly, adjusting the peak height parameter used in the peak width algorithm works to either increase or decrease the width of the identified interval, however the peak location remains the same. Despite these possible uncertainties, the approach used here attempted to optimize the peak picking parameters through trial and error in order to visually match the identified peaks to the obvious increases in fracture frequency observed in the data. The application of this approach can then be applied to other boreholes, therefore reducing interpreter bias and subjectivity in the identification of HFFI in the boreholes.

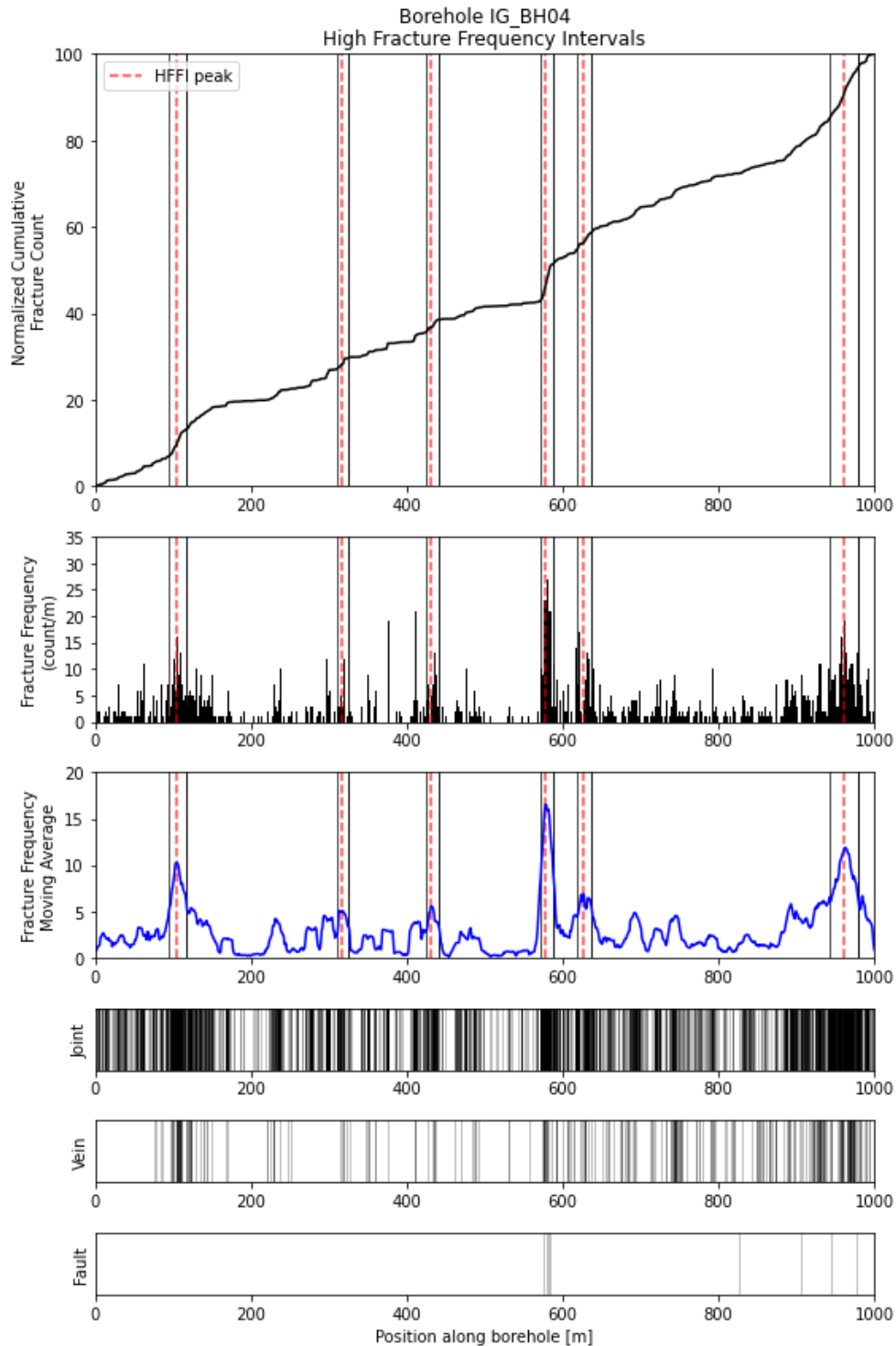


Figure 48: High fracture frequency intervals (HFFIs) interpreted based on fracture intensity from borehole fracture frequency log. Six high fracture frequency intervals are outlined by interval depths and the red dashed line represents the peak location. Stick plots indicate the distribution of each fracture type (joint, vein, fault) along the length of the borehole.

Table 10: High Fracture Frequency Intervals from IG_BH04

High Fracture Frequency Interval (HFFI)	Top Position (m)	Bottom Position (m)	Width (m)	Dominant Fracture Set Orientations* (major; minor (STR TYPE))	Rock Type, Alteration, Infill
IG_BH04_HFFI_1	94.08	116.97	22.89	228/84 (JN, VN); 292/86 (JN, VN)	Biotite granodiorite-tonalite with no subordinate rock types. Potassic alteration, chloritization and minor carbonatization. Epidote, chlorite, and iron oxide are most common infill types, along with alkali feldspar. These infill types are associated with both dominant fracture sets.
IG_BH04_HFFI_2	310.08	325.75	15.67	286/79 (JN, VN)	Biotite granodiorite-tonalite with no subordinate rock types. Potassic alteration and minor chloritization, hematization, silicification and carbonatization. Iron oxide, calcite and chlorite are most common infill types, along with lesser epidote, quartz, alkali feldspar and plagioclase.
IG_BH04_HFFI_3	424.25	441.33	17.08	219/76 (JN, VN)	Biotite granodiorite-tonalite, one feldspar-phyric tonalite dykes. Potassic alteration, chloritization and minor hematization, silicification and carbonatization. Calcite, chlorite, and alkali feldspar are most common infill types, along with minor epidote and quartz.
IG_BH04_HFFI_4	570.71	588	17.29	306/38 (JN, VN, FLT)	Biotite granodiorite-tonalite, one amphibolite. Potassic alteration, and hematization with minor chloritization, silicification and bleaching. Calcite, chlorite, and quartz are most common infill types, with minor iron oxide, epidote, clay, broken rock, and alkali feldspar.
IG_BH04_HFFI_5	618.17	637.65	19.48	274/63 (JN, VN)	Biotite granodiorite-tonalite with one amphibolite. Silicification, chloritization, potassic alteration, and hematization, with minor carbonatization and bleaching. Calcite and quartz are most common infill types, with minor chlorite, iron oxide, sulphide, and alkali feldspar.
IG_BH04_HFFI_6	943.62	978.81	35.19	111/87 (JN, VN, FLT), 190/48 (JN, VN)	Feldspar-phyric biotite granodiorite-tonalite with two amphibolites, as well as one amphibolite immediately above this interval. Chloritization and potassic alteration with minor silicification. Epidote, quartz, chlorite, calcite with minor alkali feldspar, iron oxide, pyrite, soft gouge and broken rock.

*DipDirection/Dip convention

For each HFFI, fracture (including joints, veins, and faults) orientations are plotted on stereonet to further evaluate the orientation distributions and define one or more orientations that are characteristic of the interval (e.g. HFFI_1 in Figure 50, see Appendix F: for stereonet of all defined HFFIs). Figure 49 presents a Terzaghi-weighted stereonet for HFFI_1 containing 116 fractures (veins, and joints). Dominant orientations in Table 10 are interpreted manually as the peaks defined by the Terzaghi-weighted pole density maxima. The resulting fracture orientations from within the HFFIs can provide input into modelling such zones as surfaces in deterministic fracture network models.

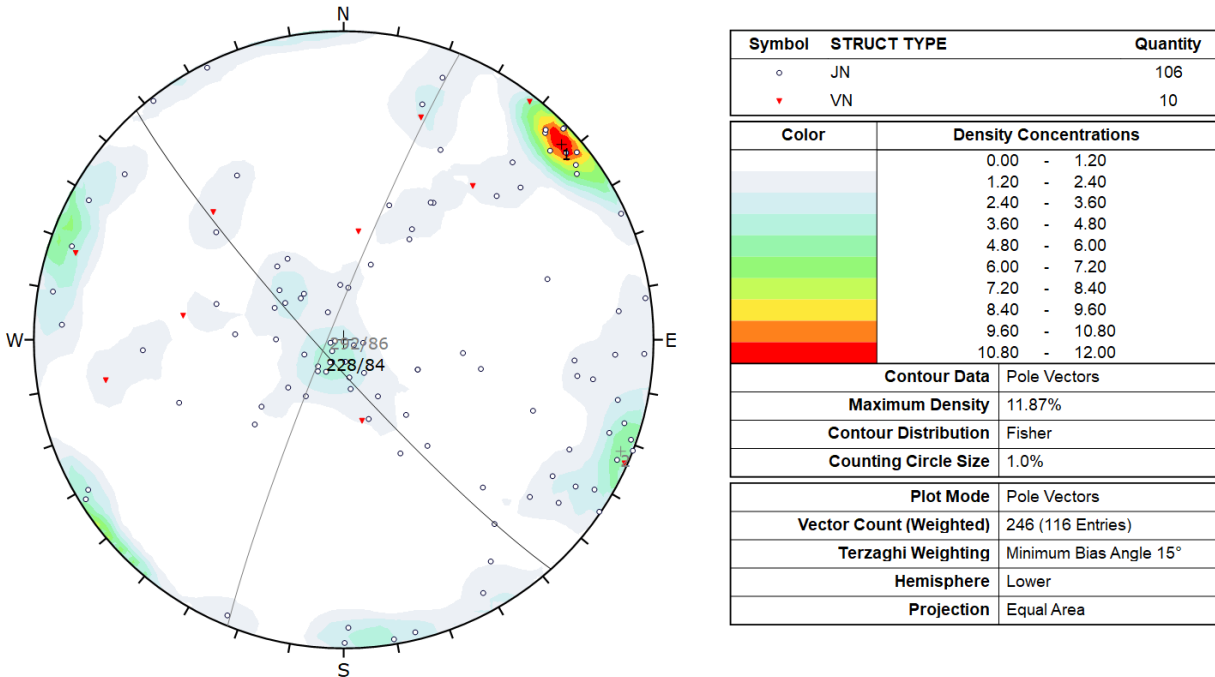


Figure 49: Terzaghi-weighted stereonet plot of fractures (JN, VN) within high fracture frequency interval HFFI_1 from 94.08 – 116.97 m. Two peaks are defined, a major peak with a mean orientation of 228/84 (best fit plane shown as black great circle) and a minor peak with a mean orientation of 292/86 (best fit plane shown as grey great circle; Dip Direction/Dip convention).

HFFI_1 (94.08 – 116.97 m)

The interval defined by HFFI_1 is composed of biotite granodiorite-tonalite (Figure 5048) and is positioned relatively shallow in the borehole between 94.08 – 116.97 m with a length of 22.89 m. Throughout the interval, there are visible pink-coloured alteration logged as potassic alteration and hematization, and minor amount of chloritization and bleaching, mainly ranging from moderate to high alteration index. An almost 3 metre interval of high alteration (A4) is logged from approximately 98 to 101 m which appears to coincide with an increase in fracture intensity. The HFFI_1 interval occurs within the RU1 rock unit domain and occurs at the boundary of the SU1 and SU2 structural unit domains.

The fractures in this interval mainly comprise joints (N=106) with 10 logged veins. Over the HFFI_1 interval, the fracture frequency reaches a maximum of 20 fractures per metre at approximately 106 m depth along borehole. Fractures orientations range from a relatively low angle to the core-axis, forming two dominant steeply dipping fracture orientations. Roughly half of the fractures in the interval belong to the subhorizontal fracture set (Fracture Set 1).



Figure 50: Core from a portion of HFFI_1 (95.17 – 110.00 m). Biotite granodiorite-tonalite is characterized by well spaced, shallow and steeply dipping fractures.

HFFI_2 (310.08 – 325.75 m)

In terms of rock types, HFFI_2 is composed of only biotite granodiorite-tonalite. Pink and white coloured alteration, logged as potassic alteration, is visible through the entire length of the interval (Figure 51). Hematization is logged over a four-metre interval from approximately 316 to 320 m along borehole correlated to an increase in fractures. Chloritization, silicification and carbonatization are also logged in minor amounts through the interval.

The orientations of the fractures in this interval are well dispersed making it difficult to identify any clear fracture sets. The fractures in this interval mainly comprise joints (N=61) with 4 logged veins. Over the HFFI_2 interval, the fracture frequency reaches a maximum of 28 fractures per metre at approximately 319.5 m depth along borehole. Fracture orientations range from a relatively low angle to the core-axis, forming one dominant steeply dipping fracture set with a mean plane steeply dipping towards the WNW at 286/79 (Fracture Set 2). Other steeply dipping fractures tend to be randomly distributed and do not form well defined clusters.



Figure 51: Core from a portion of HFFI_2 (309.27 – 326.69 m). Biotite granodiorite-tonalite with visible pink alteration logged mainly as hematization and potassic alteration. There is a local increase in fracturing in proximity to the zones of alteration

HFFI_3 (424.25 – 441.33 m)

HFFI_3 is mainly biotite granodiorite-tonalite with a 1 m wide feldspar-phyric tonalite dyke (Figure 52). The majority of the interval is logged with potassic and chlorite alteration occurring within the biotite granodiorite-tonalite. Alteration logged within the feldspar phyric tonalite dyke was primarily carbonatization with a moderate alteration intensity (A3).

Increases in fracture intensity within this HFFI_3 interval are mainly focused within and around the feldspar-phyric tonalite dyke (see Figure 52). Orientations of fractures within the interval are predominantly steeply dipping with a dip direction towards the southwest. This is interesting given that the borehole is plunging towards the southeast, making the intersection of this fracture orientation difficult. Fractures in this interval mainly comprise joints (N=80) with 6 logged veins. Over the HFFI_4 interval, the fracture frequency reaches a maximum of 13 fractures per metre at approximately 427.5 m depth along borehole and reach 12 fractures per metre within the feldspar-phyric tonalite dyke at a depth of 435.5 m along borehole. Fracture orientations form one dominant steeply dipping fracture set with a mean plane steeply dipping towards the SW at 219/76 (Fracture Set 3). Other steeply dipping fractures tend to be randomly distributed and do not form well defined clusters.



Figure 52: Boxed core images showing the majority of the HFFI_3 (from 424.54 – 442.06 m). Interval is dominated by biotite granodiorite-tonalite with a 1 m interval of feldspar-phyrlic tonalite dyke. Pink coloured alteration is present throughout the length of the core interval logged mainly as potassic alteration and minor chloritization. Carbonatization is logged within the feldspar-phyrlic tonalite dyke. Fractures are well spaced in the biotite granodiorite-tonalite and more concentrated within the dyke.

HFFI_4 (570.71 – 588.0 m)

HFFI_4 interval is mainly comprised biotite granodiorite-tonalite (16.73 m) with a 0.56 m wide amphibolite from 576.11 m to 576.67 m depth along borehole (Figure 53). The interval starts at approximately the same borehole depth as the boundary between SU3 and SU4. HFFI_4 is the most well-defined fractured interval within the borehole. Throughout the interval, there is visible pink coloured alteration present within the biotite granodiorite-tonalite logged as low to moderate intensity hematization and potassic alteration (Figure 53). In proximity to the amphibolite (within 5 metres), low to moderate alteration intensity are also observed as chloritization, silicification and bleaching. Within the amphibolite unit, high intensity alteration is recorded as hematization, chloritization and carbonatization.

Fractures within HFFI_4 broadly form a cluster of fractures that dip shallow to moderately towards the NE, with the peak of the fracture poles dipping 38° towards 306° . This orientation is distinct from the fracture sets assigned earlier in the report, exhibiting a similar strike direction but shallower dip than Fracture Set 2, and steeper dip than Fracture Set 1. This orientation overlaps with the spread of amphibolite contact orientations in IG_BH04 (Figure 25) and is also similar to the general attitude of amphibolite contacts described at the site scale (DesRoches et al., 2021). The

interval contains 215 fractures, comprising 198 joints, 13 veins, and 4 faults. The orientation of the peak of the fracture poles is consistent with the orientation of the amphibolite upper and lower contacts, with a mean dip of 27° towards 276° . Fracture intensity reaches a maximum within the amphibolite of 28 fractures per metre, with a broad highly fractured interval extending below the amphibolite into the biotite granodiorite-tonalite. The most common infill minerals in HFFI_4 are calcite, chlorite, and quartz. Less common infill types include iron oxide, epidote, clay, broken rock, and alkali feldspar. The high fracture intensity also visually coincides with the increases in rock alteration in proximity to the amphibolite unit. The lower contact of the amphibolite also displays increased deformation in a 10 cm wide interval marked by the presence of a strong foliation and shearing. Fracturing along this lower amphibolite contact resulted in the loss of drill fluid circulation and an opportunistic groundwater sample was collected. This interval has been classified as a hydraulically conductive fracture.



Figure 53: Boxed core images showing a portion of HFFI_4 (a: 570.33 – 587.67 m). Interval is dominated by biotite granodiorite-tonalite with a 0.5 m interval of amphibolite. Pink coloured alteration is present throughout the length of the core interval logged mainly as potassic alteration and hematization. Fracture intensity peaks within the amphibolite and continues as a broad highly fractured interval into the biotite granodiorite-tonalite rock deeper in the interval.

HFFI_5 (618.17 – 637.65 m)

HFFI_5 straddles the bottom of RU2 and the top of RU1b rock unit domains. The upper boundary of the HFFI_5 interval comprises approximately 2.5 m amphibolite with the remainder of the interval comprising biotite granodiorite-tonalite (Figure 54). The amphibolite is logged with minor amounts

of alteration recorded as moderate to low intensity chloritization along with carbonatization, mainly along the lower and upper contacts (upper contact is just outside the HFFI_5 interval). Bounding the amphibolite is a halo of potassic alteration with silicification, in the biotite granodiorite-tonalite. The amphibolite is marked by a sharp increase in gamma-gamma density values and a reduction in neutron counts. The upper and lower contacts of the amphibolite are also marked by a strong increase in natural gamma ray counts, inferred to be associated with the presence of the alteration assemblages noted above. The biotite granodiorite-tonalite throughout the HFFI_5 interval is fairly uniform, equigranular, and is logged locally with weak to moderate amounts of hematization and potassic alteration. The central portion of the HFFI_5 interval displays low to moderate intensity silicification, which presents itself in core as darkened glassy texture within the biotite granodiorite-tonalite.

Fractures (faults and joints) show a broad spread in orientations, with fractures predominantly dipping moderately to steeply towards the SW, W, and NW. Overall, the interval contains 115 fractures, comprising 104 joints and 11 veins. A single weakly defined peak is interpreted based on Terzaghi weighted pole density as a mean plane dipping 63° towards 274° . Fracture intensity reaches a maximum of 17 fractures per metre, within the amphibolite near the top of the interval. Ductile strain localization is also evident along the margins of the amphibolite and into the surrounding biotite granodiorite-tonalite.

The most common infill minerals in HFFI_5 are calcite and quartz. Where calcite is identified it often occurs in association with chlorite and to a lesser extent iron oxide. These calcite-filled fractures follow the same broad distribution in poles that is evident for the entire HFFI_5 interval. Where quartz is identified, it is the only mineral present, except in one instance where plagioclase was also logged. The poles to quartz-filled fractures plot primarily within the southeastern quadrant.



Figure 54: Boxed core images showing the majority of the HFFI_5 (from 616.74 – 637.03 m). The interval starts in amphibolite, transitioning down hole across a sheared contact into variably altered biotite granodiorite-tonalite. A visibly dark grey section of the biotite granodiorite-tonalite is a result of silicification, hematization and potassic alteration. Brittle structures throughout the interval dip moderately to steeply towards the SW, W, and NW.

HFFI_6 (943.62 – 978.81 m)

HFFI_6 is near the base of RU3, at the bottom of IG_BH04. The upper boundary of the HFFI_6 interval comprises two amphibolite occurrences, one 1.88 m in length and the other 0.47 m in length, interlayered with feldspar-phyric biotite granodiorite-tonalite (Figure 6).. Two additional amphibolites occur along the remainder of HFFI_6, one 0.09 m in length and the other 0.76 m in length, also interlayered with feldspar-phyric biotite granodiorite-tonalite, which persists to the bottom of the interval. Ductile strain is localized along the margins of, and within, all amphibolite occurrences. No other subordinate rock types are identified in this interval.

There is pinkish alteration visible around the amphibolites, logged as potassic alteration, as well as hematization, and local silicification. Chloritization is identified throughout the entire HFFI_6 interval, most prominently evident around fractures in the amphibolite and in association with distinct bleached halos around fractures in the feldspar-phyric biotite granodiorite-tonalite.

Overall, fractures (faults, joints, and veins) are mostly near-vertical with a broad spread in orientations. A single prominent peak is interpreted based on Terzaghi weighted pole density as a mean plane dipping 87° towards 111° . A second, weaker, pole cluster defines a mean plane dipping 48° towards 190° on a subset of moderately dipping fractures. Fracture intensity reaches a maximum of 20 fractures per metre, within the centre of the interval near the narrow (0.09 m length) amphibolite occurrence.

The most common infill minerals in HFFI_6 are epidote, chlorite and quartz. Epidote is the only identified infill mineral in some fractures, otherwise it occurs in association with some combination of calcite, chlorite, quartz and alkali feldspar. Quartz is commonly associated with alkali feldspar and chlorite. All of these infill minerals are represented in the group of near vertical NNE striking fractures. Only chlorite and, to a lesser degree quartz, are represented in the group of moderately SW dipping fractures. Iron oxide is a less common infill mineral that occurs in more randomly distributed fractures. One occurrence of soft gouge is identified within the fault logged near the base of the HFFI_6 interval.



Figure 55: Boxed core images showing the majority of the HFFI_6 (from 941.02 – 978.01 m). The interval starts with two amphibolites, interlayered with feldspar-phyric biotite granodiorite-tonalite. The majority of the interval exhibits chloritization, most evident in association with distinct bleached halos around fractures in the feldspar-phyric biotite granodiorite-tonalite. Epidote, iron oxide, and calcite infilled fractures are common. The majority of brittle structures are near vertical and strike NNE.

Comparison of Fracture Orientations to Local Lineament Network

Fracture orientations tend to be strongly correlated with the dominant lineament trends that were interpreted using remote sensing data (DesRoches et al., 2018). Figure 56 displays the interpreted structural lineaments in proximity to IG_BH04. North-northeast trending lineaments are the most prominent in close proximity to the borehole, and other than several short north-trending features and one short northwest-trending feature, are the only features near to or transected by the surface trace of the borehole path. Rose diagrams for both unweighted and Terzaghi-weighted borehole-logged fractures, with a minimum dip angle of 45°, are shown in Figure 58. The unweighted rose diagram (Figure 57) shows a dominant north-northeast trend in the lineaments. However, lineaments in this orientation tend to be mainly short and discontinuous. Despite the discontinuity of these lineament traces, it is possible these features are connected in the bedrock. Figure 57b shows the lineaments weighted by length to increase the importance of long structural features. The length weighed lineaments still shows a north-northeast trend, however, east and north-west trending lineaments are also present.

Comparing the interpreted lineament trends with those of the interpreted fracture sets highlights some similarities in orientations. The north-northeast-trending lineaments are consistent with the strike of Fracture Set 2 and dominant or subordinate fracture peaks in HFFI_1, 2, 4, 5 and 6. The one short northwest-trending lineament near IG_BH04 is consistent with the strike of Fracture Set 3 and dominant fracture peaks in HFFI_1 and HFFI_3. An east-southeast-trending Wabigoon diabase dyke is present in proximity to IG_BH04 but this orientation does not appear in the suite of interpreted fracture sets. It should also be noted that the gently-inclined to subhorizontal fractures of Fracture Set 1 will not be well represented in the lineament data.

It is worth noting that the north-northeast-trending lineaments near IG_BH04 parallel the dominant direction of glacial advance and retreat across the region. There is therefore some uncertainty regarding whether they do, or do not, reflect structurally significant features of the bedrock or if some are instead a product of glacial erosion. However, the understanding that the steeply inclined and north-northeast-striking Fracture Set 2 is present along the length of the borehole, and is a dominant fracture orientation in several HFFI's, suggests that at least some of these lineaments do represent real bedrock structures. It is also noteworthy that the surface trace lengths of the interpreted north-northeast-trending lineaments are general short (< 500 m) where transected by the surface trace of the borehole path and yet the deepest high fracture frequency interval, HFFI_6 at approximately 950 m along the borehole path shares the same orientation. This may suggest either that these north-northeast-trending lineaments are longer than the current interpretation or they extend to greater depths than the length of their surface trace would suggest.

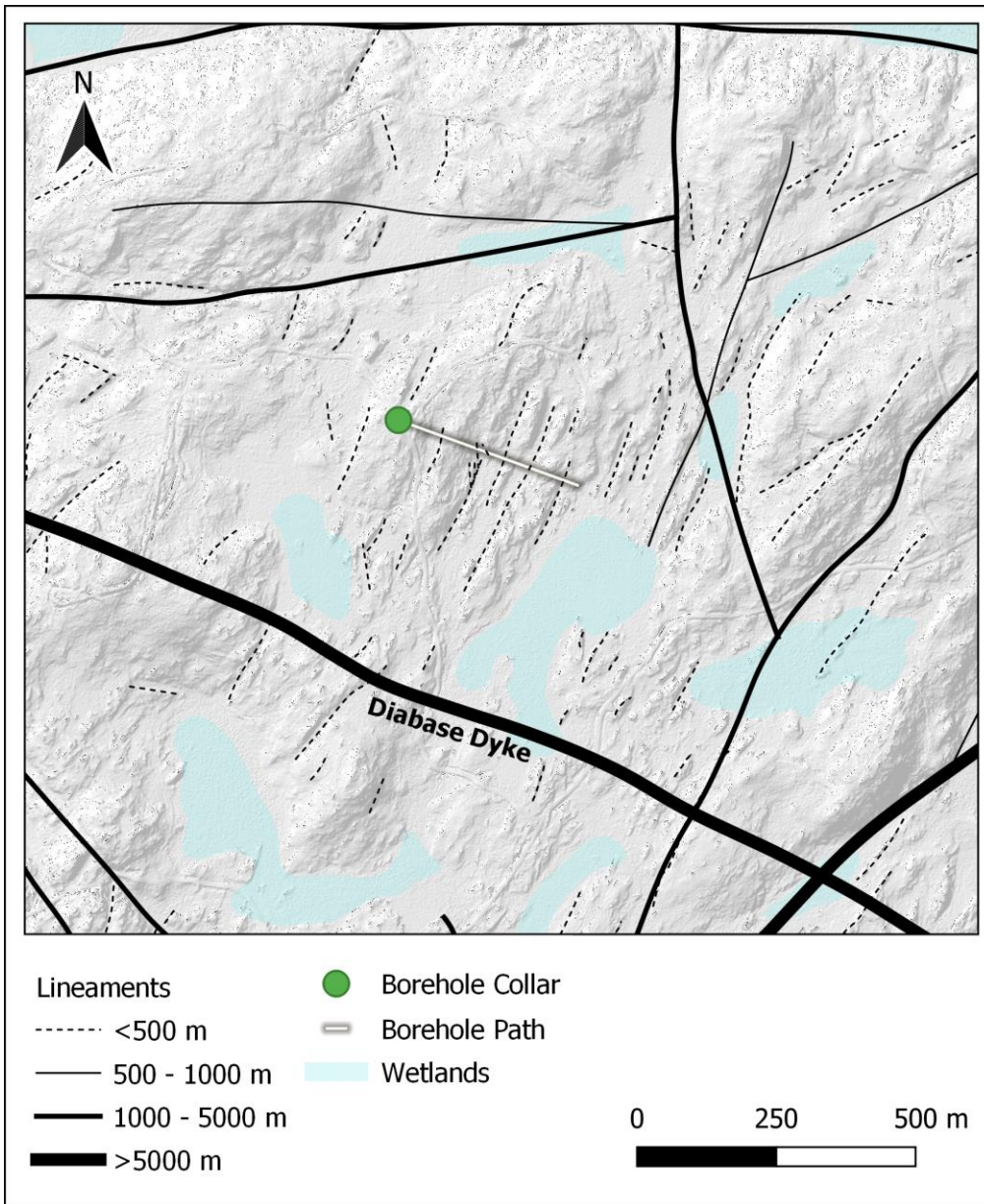


Figure 56: Lineament traces near IG_BH04 interpreted from LiDAR DEM and airborne geophysics data (DesRoches et al., 2018). Lineament traces are dominantly north-northeast trending, with fewer westerly to northwesterly trending lineaments. The approximate trace of IG_BH04 is shown as a white line.

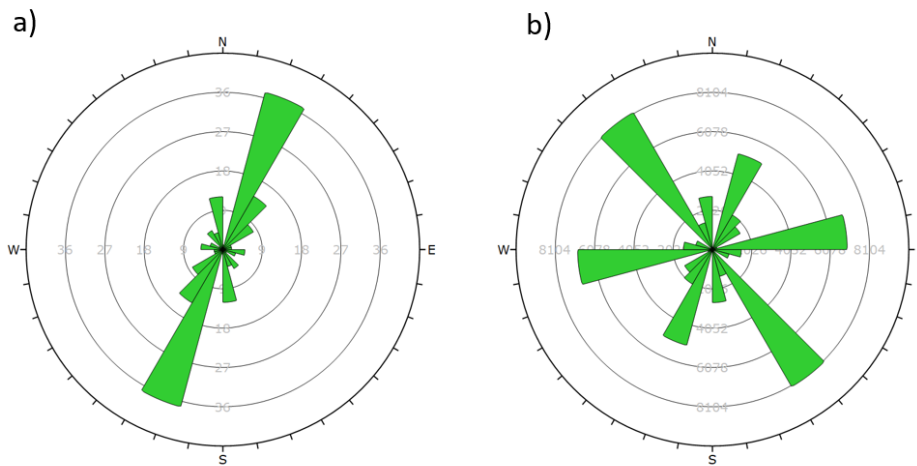


Figure 57: Rose diagram of the lineaments (N = 94) around IG_BH04 (see Figure 56) interpreted from LiDAR DEM and airborne geophysics data (DesRoches et al., 2018). a) Unweighted; b) Length-weighted to highlight more prominent lineaments. Lineament orientations are plotted using a bin size of 15 degrees.

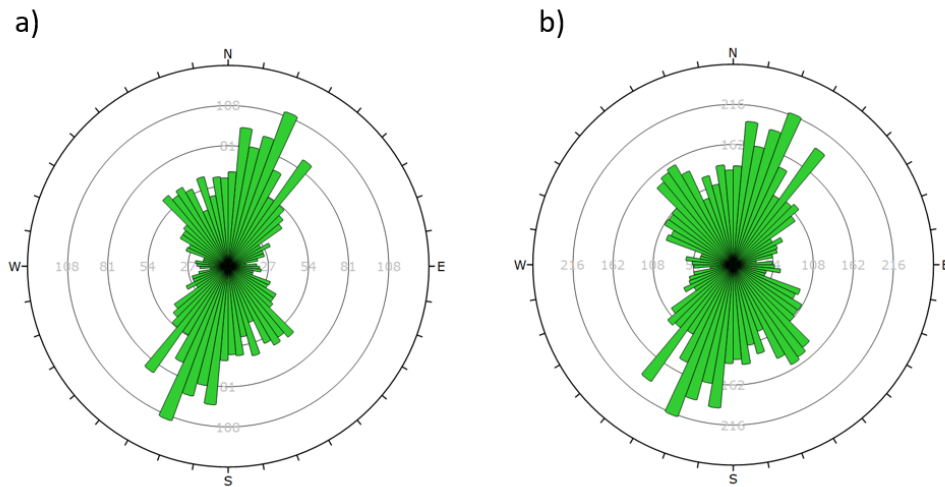


Figure 58: Rose diagrams of the borehole logged fracture orientations using a minimum dip angle of 45 degrees, and bin size of 5 degrees. a) Unweighted (N = 1706 is the total number of fractures); b) Terzaghi-weighted to account for directional bias of the borehole path (weighted N = 3945 is the sum of the weightings).

4 SUMMARY OF FINDINGS AND UNCERTAINTIES

4.1 Findings

The geological findings are based on the geological information available to date, which are summarized in this report. One primary consideration is the understanding that the available

information *is from a single borehole*. Whether or not the characteristics of the bedrock described throughout this report will transfer to other boreholes remains uncertain. However, the level of uncertainty related to the overall understanding of the bedrock across the study area is expected to decrease as information from multiple boreholes is acquired and integrated together. A simplified summary of the geological model for IG_BH04 is presented in Figure 59, showing the final lithology log, rock units, per metre fracture frequency, structural units, and high fracture frequency intervals.

The main rock type intersected by borehole IG_BH04 is a biotite granodiorite-tonalite, accounting for more than 85 % of the recovered core. Additional primary rock types identified in IG_BH04 include a slightly more porphyritic endmember (feldspar-phyric biotite granodiorite-tonalite intruding biotite granodiorite-tonalite) representing 11 % of recovered core, and a tonalitic endmember (biotite tonalite) representing 2.3 % of recovered core. While the biotite tonalite has been recognized in other boreholes, the feldspar-phyric biotite granodiorite-tonalite is a newly identified rock type, and its occurrence in the lower portion of IG_BH04 suggests the presence of a distinct intrusive body. Compositionally, all three of these rock types are still quite similar and, together, represent 98.7 % of the recovered core. Rare earth element (REE) data exhibit a similar pattern for all three rock types which suggests a common magmatic source.

Subordinate rock types, representing less than 2 % of the total core recovered, include distinct metre- to sub-metre scale thick units of amphibolite, and several suites of sub-metre thick dykes of varying felsic composition. These subordinate rock types are of the same types, and in similarly low volume of recovered core, as identified in previous boreholes. Amphibolites represents the most common subordinate rock type identified during borehole drilling, accounting for 1 % of all recovered core in a total of 10 occurrences. These rocks have a complex and variable mineralogical assemblage, and as in other boreholes, exhibit ductile to brittle ductile strain localization both internally and their margins with the surrounding bedrock. The amphibolites occur in contact both with the biotite granodiorite-tonalite and the feldspar-phyric biotite granodiorite-tonalite. Poles to amphibolite contacts plot in the southeast quadrant of the stereonet indicating gently to steeply inclined contacts that dip northwest. Two feldspar-phyric tonalite dykes were encountered in IG_BH04, representing only 0.2 % of the recovered core.

Optical and acoustic televiewer, natural and spectral gamma, gamma-gamma density and neutron geophysical logs provided additional evidence to distinguish subordinate rock types from the main rock types in this crystalline rock environment. The integration of visual geological core logging and geophysical logging was useful for developing the final interpretation of logged rock types and alteration and was critical for assigning true orientations to the logged structures.

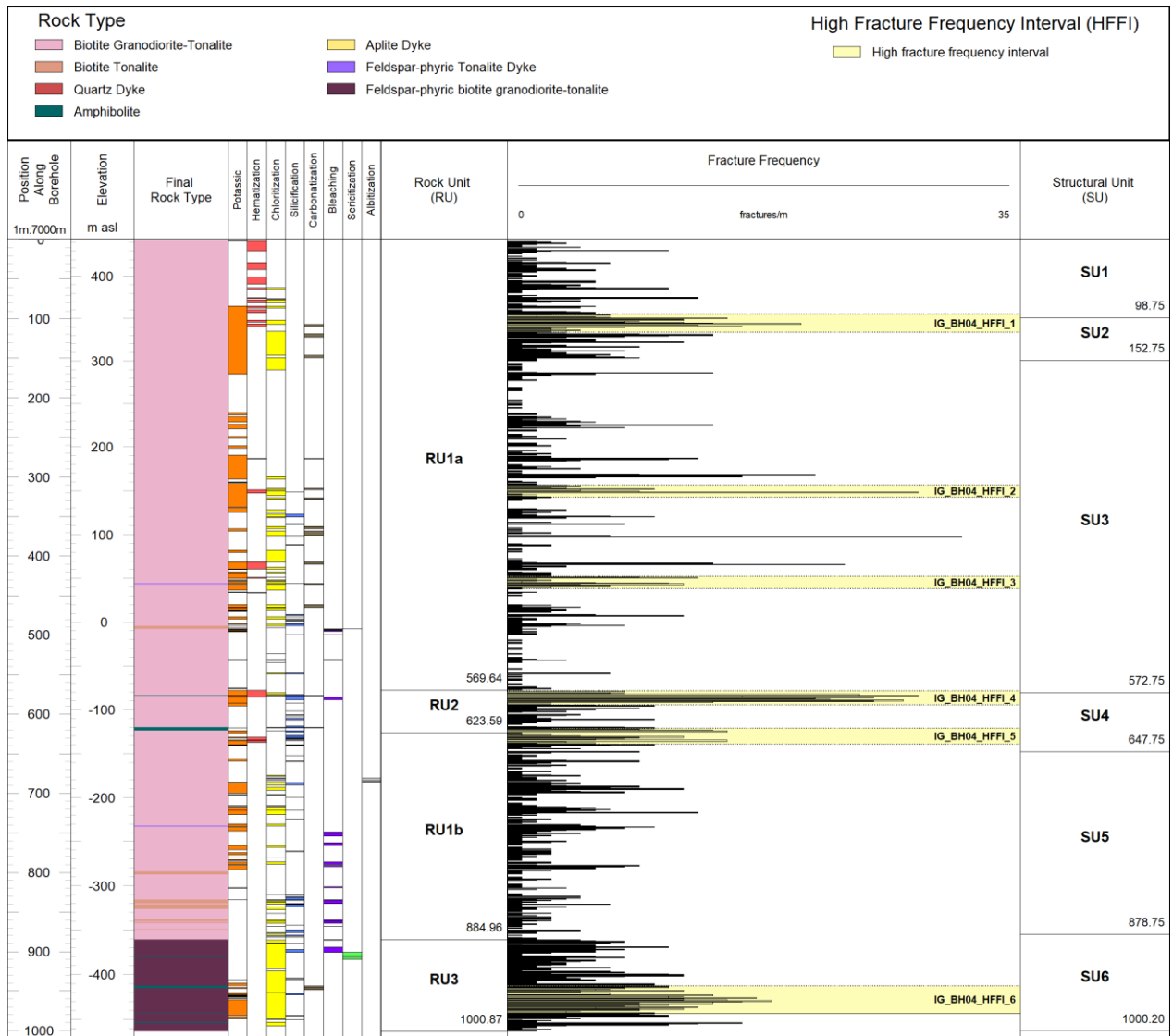


Figure 59: Summary log of geological information, including (from left to right), final log of lithology, alteration, classification of rock units, per metre fracture frequency, and structural units, representing the 1-dimensional geological model for IG_BH04.

Overall, the degree of alteration of the bedrock intersected by IG_BH04 appears to be relatively low even though alteration products are found along a large proportion of the borehole length. Eight alteration types (potassic, silicification, hematization, chloritization, bleaching, sericitization, carbonatization, and albitization) were identified during geological and geophysical logging. Chloritization and potassic alteration, as well as silicification, were present along the majority of the length of the borehole. Hematization was the only alteration type logged at, and near to, the surface. Bleaching, sericitization and albitization were only logged in the lower half of the borehole. It should be noted that, based on optical petrographic analysis, none of the intervals logged visually as potassic alteration showed evidence of true hydrothermal potassic alteration (secondary alkali feldspar, biotite, sulphides) when examined petrographically. The pink colour of the recovered core is a product of magmatic (primary) alkali feldspar or replacement of very fine-grained sulphides with iron oxide minerals.

Based on broad changes in rock type along the borehole, four rock units were defined. This included two rock units dominated by biotite granodiorite-tonalite (RU1a, RU1b), one rock unit with biotite granodiorite-tonalite with amphibolite (RU2), and one rock unit defined by the distribution of feldspar-phyrlic biotite granodiorite-tonalite and amphibolite (RU3). The distribution of alteration was not considered to be a useful characteristic for distinguishing the rock units. The majority of the borehole has a massive texture, with some minor rock types dominantly hosting ductile or brittle-ductile structure (foliation and shear zones). The presence or absence of ductile or brittle-ductile fabric was not considered to be a useful characteristic for defining rock units. Two high-fracture frequency intervals (see below) coincide with amphibolite occurrences at the margins of RU2.

The structures identified in the borehole included features associated with ductile, brittle-ductile, and brittle deformation processes. Ductile structures are distributed irregularly along the entire length of the borehole, with up to 100 m long gaps. One cluster of foliation is present at around 300 m length along the borehole. A foliation is defined as weak, and its orientation varies. Shear zones exhibit characteristics of both brittle and ductile deformation processes. Shear zones are commonly identified in association with amphibolite occurrences where they manifest as cm- to dm-scale localized shear zones that are developed along, and sub-parallel to, the amphibolite contacts. Accordingly, poles to shear planes exhibit a similar distribution to amphibolite contacts with a spread throughout the SE quadrant of the stereonet. Overall an increased degree of ductile to brittle structural complexity is commonly associated with the amphibolite, occurrences suggesting that the presence of these rock types has served to focus fluid flow at some point in the geological past.

Joints are overwhelmingly the most common fracture type identified in the borehole, followed by veins and faults. Faults are consistently very narrow, identified mainly by the presence of minor offset of markers, broken rock, or soft gouge. Poles to faults also follow a similar distribution to those of amphibolite contacts and shear zones.

The complete fracture dataset appears to indicate the presence of three fracture sets:

- a subhorizontal to moderately inclined set, dipping east-southeast (Set 1),
- a near-vertical set, striking north-northeast (Set 2), and
- a near-vertical set, striking northwest (Set 3)

The borehole was subdivided into six structural units based on variation in fracture frequency log and slope of the cumulative fracture frequency curve. The subdivision resulted in average fracture frequencies for the structural units ranging between 1.98 and 6.57 fractures per metre.

Six high fracture frequency intervals (HFFIs) were defined along the borehole using a semi-automated approach applied to the borehole fracture frequency per metre log. The intervals range in width from just over 15 m to just over 35 m. Five of the HFFIs were identified between approximately 100 and 600 m along the borehole, with one additional occurrences below 950 m. The four deepest HFFIs include at least one rock type occurrence other than biotite granodiorite-tonalite. The most common other rock types represented are amphibolite in three HFFIs and one feldspar-phyrlic tonalite dyke in the other HFFI.

Logged structures, defined fracture sets and HFFIs in the borehole display some correlation to the dominant lineament trends in proximity to the borehole. The north-northeast-trending lineaments are consistent with the strike of Fracture Set 2 and dominant or subordinate fracture peaks in HFFI_1, 2, 5 and 6. The one short northwest-trending lineament near IG_BH04 is consistent with the strike of Fracture Set 3 and dominant fracture peaks in HFFI_1 and HFFI_3. These correlative borehole-interpreted fracture sets and peak HFFI orientations are subvertical to moderately inclined. Therefore, it is possible that some lineaments, currently interpreted to represent vertically oriented fracture zones, could instead have steep to moderate dips.

Considering all of the geological observations described throughout the report, several key summary points are highlighted below. These observations align with a developing understanding that, while the rock is homogeneous overall, there are distinct regions along the borehole that have relatively distinct character, including that:

- an additional end-member of the granitoid bedrock, feldspar-phyric biotite granodiorite-tonalite that is also finer-grained than the main biotite granodiorite-tonalite, occurs together with amphibolite as a distinct intrusive unit in the lower approximately 100 m of the borehole (RU3);
- amphibolite occurrences cluster around 600 m allowing a rock unit with biotite granodiorite-tonalite and amphibolite to be defined (RU2); and
- amphibolite occurrences show evidence of ductile strain and brittle deformation internally and along their contacts, as well as evidence of hematization and chloritization.

The significance of the geological relationships identified here will continue to be explored as additional information is gathered from future surface and subsurface investigations, including the drilling of additional boreholes, and both two-dimensional and vertical seismic profiling.

4.2 Uncertainties

With respect to the feldspar-phyric biotite granodiorite-tonalite end-member identified at the base of IG_BH04, its overall appearance and composition is suggesting association with the feldspar-phyric tonalite dykes present throughout the site (in this and other boreholes). However, only a relatively small volume of such dykes were identified in IG_BH04. Regardless, the composition of this rock suggests it is a close relation to the dominant biotite granodiorite-tonalite and biotite tonalite already identified in the previous boreholes. Importantly, these granitoid rocks comprise the majority of the bedrock with only very minor amounts of subordinate rocks, which is consistent with expectations. The overall geometry of this feldspar-phyric biotite granodiorite-tonalite also remains uncertain since it has only been encountered in one borehole. Though the distribution of the amphibolite and the other subordinate rock types in three-dimensions is also a remaining uncertainty, the overall volume of these subordinate rocks is extremely low. Regarding the significance of the logged alteration, it is acknowledged that some uncertainty remains regarding the timing and conditions on its formation. However, it is likely that the hydrothermal fluids associated with the alteration are products of ancient geological processes rather than recent events.

With respect to structure, there is uncertainty in the true density and mean orientation of steeply dipping structures. Although a Terzaghi-weighting was applied to correct for borehole orientation bias, it is understood that there are other techniques available. Further exploration of the best approach to account for the borehole orientation bias will be investigated as additional data becomes available, including data from differently oriented angled boreholes. Specifically regarding HFFI_4, the dominant fracture plane identified for this fractured interval does not coincide well with the fracture sets assigned for IG_BH04. The HFFI_4 pole cluster is between that of Fracture Sets 1 and 2. The relationship between the structure of HFFI_4 and the defined fractures sets in IG_BH04 continues to be investigated.

Whether or not the drilling activity itself, or stress relief, may have induced the broken character of logged fractures also remains an uncertainty. The true nature of logged televiewer-only and core-only structures also remains uncertain. In addition, the timing and number of stages of fracture development (and re-activation), mineral infilling and alteration, and the resulting implications for the geological history of the area remain uncertain.

The surface trace lengths of the interpreted north-northeast-trending lineaments are generally short (< 500 m) where transected by the surface trace of the borehole path and yet the deepest high fracture frequency interval, HFFI_6 at approximately 950 m along the borehole path shares the

same orientation. This may suggest either that these north-northeast-trending lineaments are longer than the current interpretation or they extend to greater depths than the length of their surface trace would suggest.

The subset of identified fractures that are likely to be hydraulically conductive also remains uncertain. This is especially important in understanding the significance of logged geological apertures. As mentioned above, geological apertures are estimated values only because there are multiple possible sources of uncertainty in how a reported aperture value relates to the true aperture of a fracture identified as broken. There are uncertainties related to measurement inaccuracy, including where the opening is very small, where the opposing fracture planes are not parallel or fit poorly together, or due to limits in televiewer resolution. In addition, effects due to drilling or decompression may create or enhance the visible open space identified as aperture. Finally, aperture measured in core or on a borehole wall is only a local aperture that is not necessarily representative over the entire fracture. There are also cases where fractures are logged as broken but exhibit no measurable geological aperture. Additional analysis of the observed structures in the acoustic and optical televiewer datasets, including fractures and their characteristics (e.g., broken vs intact nature, mineral infilling, orientation), will aim to reduce these uncertainties.

The absolute dimensions of the rock units (RU) and structural units (SU) presented above were defined based on a subjective and non-unique approach. With the same data inputs, alternative approaches may have defined more or less units and ultimately produced a different geological model for the borehole. Finally, a statistically robust method was used to define high fracture frequency intervals (HFFI) along the borehole. However, the approach is still non-unique. Different analytical approaches may produce a different result. Furthermore, the broader geological significance of these intervals, identified along a single borehole, remains uncertain.

5 REFERENCES

- American Petroleum Institute (API), 1985. Directional Drilling Survey Calculation Methods and Terminology (Bulletin No. D20). Dallas, TX.
- Blackburn, C.E., Hinz, P., 1996. Gold and base metal potential of the northwest part of the Raleigh Lake greenstone belt, northwestern Ontario-Kenora Resident Geologist's District; in Summary of Field Work and Other Activities 1996, Ontario Geological Survey, Miscellaneous Paper 166, p.113-115.
- Daniels, J.J., Olhoeft, G.R., Scott, J.H., 1984. Interpretation of core and well log physical property data from drill hole UPH-3, Stephenson County, Illinois (USGS Numbered Series No. 82-941). United States Geological Survey.
- Davy, P., Darcel, C., Bour, O., Munier, R., De Dreuzy, J.-R., 2006. A note on the angular correction applied to fracture intensity profiles along drill core. *Journal of Geophysical Research: Solid Earth* 111, B11408. <https://doi.org/10.1029/2005JB004121>
- Debon, F., Le Fort, P., 1983. A chemical and mineralogical classification of common plutonic rocks and associations. *Earth and Environmental Science Transactions of the Royal Society of Edinburgh* 73, 135–149.
- DesRoches, A., Waffle, L., Parmenter, L. 2021. 3D Site-Scale Geological Model in the Revell Batholith: Model Version 1.0. NWMO report: NWMO-TR-2021-12
- DesRoches, A., Sykes, M., Parmenter, A., Sykes, E., 2018. Lineament Interpretation of the Revell Batholith and Surrounding Greenstone Belts (No. NWMO-TR-2018-19). Nuclear Waste Management Organization.
- Golder Associates Ltd., 2015. Phase 2 Geoscientific Preliminary Assessment, Findings from Initial Field Studies: Township of Ignace, Ontario (No. APM-REP-06145-0001). Nuclear Waste Management Organization.
- Golder Associates Ltd., Paterson Grant and Watson, Ltd., 2017. Phase 2 Geoscientific Preliminary Assessment: Geological Mapping, Township of Ignace and Area, Ontario (No. APM-REP-01332-0225). Nuclear Waste Management Organization.
- Golder Associates, 2022. Phase 2 Initial Borehole Drilling and Testing, Ignace Area. WP05 Data Report – Geophysical Well Logging for IG_BH04. NWMO Document Number: APM-REP-01332-0356
- Halla, J., 2018. Highlights on Geochemical Changes in Archaean Granitoids and Their Implications for Early Earth Geodynamics. *Geosciences* 8, 353. <https://doi.org/10.3390/geosciences8090353>
- Halla, J., van Hunen, J., Heilimo, E., Hölttä, P., 2009. Geochemical and numerical constraints on Neoproterozoic plate tectonics. *Precambrian Research* 174, 155–162. <https://doi.org/10.1016/j.precamres.2009.07.008>
- Keys, W.S., 1997. *A Practical Guide to Borehole Geophysics in Environmental Investigations*. CRC Press.
- Le Bas, M.J., Streckeisen, A.L., 1991. The IUGS systematics of igneous rocks. *Journal of the Geological Society* 148, 825–833. <https://doi.org/10.1144/gsjgs.148.5.0825>
- OGS (Ontario Geological Survey), 2011. 1:250 000 scale bedrock geology of Ontario, Ontario Geological Survey, Miscellaneous Release Data 126 - Revision 1.
- Parmenter, A., Waffle, L., DesRoches, A. 2020. An updated bedrock geology map and geological database for the northern portion of the Revell batholith (No. NWMO-TR-2020-08). Nuclear Waste Management Organization.
- Sander Geophysics Limited (SGL), 2020. 3D Geophysical Forward and Inversion Modelling of the Revell Batholith and Surrounding Greenstone Belt. (No. APM-REP-01332-0270). Nuclear Waste Management Organization.

- SRK Consulting, Inc., Golder Associates Ltd., 2015. Phase 2 Geoscientific Preliminary Assessment, Observation of General Geological Features, Township of Ignace, Ontario (No. APM-REP-06145-0004). Nuclear Waste Management Organization.
- Stone, D., 2009. Geology of the Bending Lake Area, Northwestern Ontario (Open File Report No. 6240), Summary of Field Work and Other Activities 2009. Ontario Geological Survey, Sudbury, Canada.
- Stone, D., 2010a. Geology of the Stormy Lake Area, Northwestern Ontario, Project Unit 09-003 (Open File Report No. 6260), Summary of Field Work and Other Activities 2010. Ontario Geological Survey, Sudbury, Canada.
- Stone, D., 2010b. Precambrian geology of the central Wabigoon Subprovince area, northwestern Ontario (Open File Report No. 5422). Ontario Geological Survey.
- Stone, D., Davis, D.W., Hamilton, M.A., Falcon, A., 2010. Interpretation of 2009 Geochronology in the Central Wabigoon Subprovince and Bending Lake Areas, Northwestern Ontario, Project Unit 09-003 (Open File Report No. 6260), Summary of Field Work and Other Activities 2010. Ontario Geological Survey.
- Stone, D., Halle, J., Chaloux, E., 1998. Geology of the Ignace and Pekagoning Lake Areas, Central Wabigoon Subprovince (Misc. Paper No. 169), Summary of Field Work and Other Activities 1998. Ontario Geological Survey.
- Taylor, S.R., McLennan, S.M., 1985. The continental crust: Its composition and evolution. United States.
- Terzaghi, R.D., 1965. Sources of Error in Joint Surveys. *Géotechnique* 15, 287–304.
<https://doi.org/10.1680/geot.1965.15.3.287>
- Virtanen, P. et al. 2020. SciPy 1.0--Fundamental Algorithms for Scientific Computing in Python. *Nature Methods*, 17, 261–272.
- WOOD, 2021a. Phase 2 Initial Borehole Drilling and Testing, Ignace Area. WP02 Data Report – Drilling and Coring for IG_BH04. NWMO Document Number: APM-REP-01332-0242.
- WOOD, 2021b. Phase 2 Initial Borehole Drilling and Testing, Ignace Area WP03 Data Report – Geological and Geotechnical Core Logging, Photography and Sampling for IG_BH04. NWMO Document Number: APM-REP-01332-0258.

**Appendix A: Summary List of Work
Packages Completed for IG_BH04**

WP Number	WP Name
WP01	Site Infrastructure and Access Road Construction
WP02	Borehole Drilling and Coring
WP03	Geological and Geotechnical Core Logging, Photography and Sampling
WP04a	Effective Diffusion Coefficients – Crystalline Rock
WP04b	Geomechanical Testing of Core
WP04c	Porewater Extraction and Analysis and Petrographic Analysis
WP05	Geophysical Well Logging and Interpretation
WP06	Hydraulic Testing
WP07	Opportunistic Groundwater Sampling and Testing
WP08	Temporary Well Sealing
WP12	Vertical Seismic Profiling

**Appendix B: Petrography and
lithogeochemistry data**

Petrography

Semi-quantitative optical petrography was completed by QFIR (Kingston, ON). Modal mineralogy was determined using a mineral liberation analysis technique. Note that only rock types plotted on the QAP diagram (Figure 8) are listed. PLA = plagioclase feldspar; QTZ = quartz; AFS = alkali feldspar.

Rock type mineral composition (original and normalized) presented as percentages, determined semi-quantitatively using polished thin sections.

Sample ID	From (position along borehole; m)	To (position along borehole; m)	Mineral %			Total	Mineral %			Total	Final Rock Type
			PLA	QTZ	AFS		PLA	QTZ	AFS		
IG_BH04_MG001	163.83	164.09	46.92	34.49	7.29	88.70	52.89	38.89	8.22	100.0	Biotite granodiorite-tonalite
IG_BH04_MG002	210.5	210.75	51.03	29.54	9.52	90.10	56.64	32.79	10.57	100.0	Biotite granodiorite-tonalite
IG_BH04_MG003	240.58	240.83	50.06	31.74	9.10	90.90	55.07	34.92	10.02	100.0	Biotite granodiorite-tonalite
IG_BH04_MG003 dup	240.58	240.83	50.17	31.75	9.12	91.04	55.11	34.88	10.02	100.0	Biotite granodiorite-tonalite
IG_BH04_MG004	268.11	268.37	43.64	37.38	6.56	87.59	49.83	42.68	7.49	100.0	Biotite granodiorite-tonalite
IG_BH04_MG005	292.97	293.22	50.49	31.97	6.33	88.78	56.87	36.01	7.13	100.0	Biotite granodiorite-tonalite
IG_BH04_MG006	319.86	320.12	47.61	31.23	7.06	85.91	55.42	36.36	8.22	100.0	Biotite granodiorite-tonalite
IG_BH04_MG007	345.2	345.46	43.69	35.49	10.09	89.27	48.94	39.76	11.30	100.0	Biotite granodiorite-tonalite
IG_BH04_MG007 dup	345.2	345.46	43.91	35.20	10.03	89.14	49.26	39.49	11.25	100.0	Biotite granodiorite-tonalite
IG_BH04_MG008	372.4	372.61	50.34	36.38	3.68	90.39	55.69	40.24	4.07	100.0	Biotite granodiorite-tonalite
IG_BH04_MG009	396.81	397.04	49.38	34.14	5.06	88.58	55.74	38.54	5.71	100.0	Biotite granodiorite-tonalite
IG_BH04_MG010	424.32	424.54	53.60	29.93	5.32	88.84	60.33	33.69	5.98	100.0	Biotite granodiorite-tonalite
IG_BH04_MG011	450.46	450.69	50.80	33.23	5.35	89.37	56.84	37.18	5.99	100.0	Biotite granodiorite-tonalite
IG_BH04_MG012	478.95	479.23	50.99	30.31	4.65	85.95	59.32	35.27	5.42	100.0	Biotite granodiorite-tonalite
IG_BH04_MG012 dup	478.95	479.23	51.27	30.18	4.55	86.00	59.62	35.09	5.29	100.0	Biotite granodiorite-tonalite
IG_BH04_MG013	505.81	506.03	55.02	24.50	7.78	87.29	63.03	28.06	8.91	100.0	Biotite granodiorite-tonalite
IG_BH04_MG014	532.61	532.83	53.40	30.26	4.34	88.00	60.68	34.39	4.93	100.0	Biotite granodiorite-tonalite
IG_BH04_MG015	558.87	559.12	54.35	27.09	4.76	86.20	63.05	31.43	5.53	100.0	Biotite granodiorite-tonalite
IG_BH04_MG016	587.3	587.51	49.35	28.77	12.73	90.85	54.32	31.67	14.01	100.0	Biotite granodiorite-tonalite
IG_BH04_MG016 dup	587.3	587.51	49.53	28.83	12.72	91.09	54.38	31.65	13.97	100.0	Biotite granodiorite-tonalite
IG_BH04_MG017	623.21	623.46	53.26	26.68	10.17	90.11	59.10	29.61	11.28	100.0	Biotite granodiorite-tonalite
IG_BH04_MG018	637.58	637.83	44.24	31.52	15.19	90.94	48.65	34.66	16.70	100.0	Biotite granodiorite-tonalite
IG_BH04_MG019	664.96	665.2	51.64	35.24	2.83	89.72	57.56	39.28	3.16	100.0	Biotite granodiorite-tonalite
IG_BH04_MG020	691.96	692.21	50.27	35.02	4.05	89.34	56.27	39.20	4.53	100.0	Biotite granodiorite-tonalite
IG_BH04_MG021	719.74	719.98	56.97	24.64	5.77	87.38	65.20	28.20	6.60	100.0	Biotite granodiorite-tonalite
IG_BH04_MG022	740.7	740.96	55.26	26.10	7.52	88.88	62.18	29.36	8.46	100.0	Biotite granodiorite-tonalite
IG_BH04_MG022 dup	740.7	740.96	55.31	26.10	7.45	88.85	62.25	29.37	8.38	100.0	Biotite granodiorite-tonalite
IG_BH04_MG023	770.87	771.14	45.96	30.87	16.52	93.35	49.24	33.07	17.69	100.0	Biotite granodiorite-tonalite
IG_BH04_MG024	797.28	797.49	44.03	34.36	15.39	93.78	46.95	36.64	16.41	100.0	Biotite granodiorite-tonalite
IG_BH04_MG025	826.21	826.42	45.72	31.77	13.30	90.80	50.36	34.99	14.65	100.0	Biotite granodiorite-tonalite
IG_BH04_MG026	850.19	850.39	47.03	31.57	11.44	90.05	52.23	35.06	12.71	100.0	Biotite granodiorite-tonalite
IG_BH04_MG027	878.52	878.79	48.03	33.10	10.77	91.90	52.27	36.02	11.72	100.0	Biotite granodiorite-tonalite
IG_BH04_MG027 dup	878.52	878.79	48.05	33.07	10.76	91.87	52.30	35.99	11.71	100.0	Biotite granodiorite-tonalite
IG_BH04_MG028	903.54	903.76	37.88	27.94	26.07	91.89	41.22	30.40	28.38	100.0	Feldspar-phyrlic biotite granodiorite-tonalite
IG_BH04_MG029	936.28	936.545	49.59	30.12	8.31	88.01	56.34	34.22	9.45	100.0	Feldspar-phyrlic biotite granodiorite-tonalite
IG_BH04_MG029 dup	936.28	936.545	49.57	30.15	8.30	88.02	56.31	34.25	9.43	100.0	Feldspar-phyrlic biotite granodiorite-tonalite
IG_BH04_MG030	957.15	957.4	48.29	28.97	7.05	84.31	57.27	34.36	8.36	100.0	Feldspar-phyrlic biotite granodiorite-tonalite

Litho geochemistry

All analyses performed by ALS Geochemistry Lab (Vancouver, BC) and QFIR (Kingston, ON).

Litho geochemical results of various tests carried out by ALS Geochemistry. For details on each analysis performed, see section 3.2.1.

Report Number: VA21227434																									
Report Date: 09/11/2021																									
Analyte Symbol	From (position along borehole; e; m)	To (position along borehole; e; m)	Ag	Al	As	Ba	Be	Bi	Ca	Cd	Ce	Co	Cr	Cs	Cu	Fe	Ga	Ge	Hf	In	K	La	Li		
Unit Symbol			ppm	%	ppm	ppm	ppm	ppm	ppm	%	ppm	ppm	ppm	ppm	ppm	ppm	%	ppm	ppm	ppm	ppm	%	ppm	ppm	
Detection Limit			0.002	0.01	0.02	1	0.02	0.002	0.01	0.005	0.01	0.005	0.01	0.005	0.3	0.01	0.02	0.002	0.05	0.05	0.004	0.005	0.01	0.005	0.2
Analysis Method			ME- MS61 L																						
IG_BH04_MG001	163.83	164.09	0.071	7.07	0.37	460	0.83	0.052	1.75	0.025	32.5	4.08	7.4	1.11	10.9	1.54	20.8	0.05	3.03	0.015	1.67	0.071	7.07		
IG_BH04_MG002	210.5	210.75	0.057	6.86	0.08	550	0.74	0.05	1.7	0.028	35	3.55	7.2	0.99	9.24	1.37	18.65	<0.05	2.89	0.01	1.73	0.057	6.86		
IG_BH04_MG003	240.58	240.83	0.044	6.99	0.03	500	0.77	0.037	1.73	0.026	34.5	3.72	8.5	1.49	9.61	1.43	19.05	0.05	3.13	0.013	1.64	0.044	6.99		
IG_BH04_MG004	268.11	268.37	0.054	6.79	0.17	460	0.93	0.101	1.68	0.029	37.8	3.58	7.7	1.77	8.72	1.4	19.35	0.05	3.2	0.011	1.63	0.054	6.79		
IG_BH04_MG005	292.97	293.22	0.042	6.91	0.08	490	0.89	0.061	1.71	0.022	32.3	3.39	7.8	1.36	8.48	1.34	19	<0.05	2.97	0.013	1.66	0.042	6.91		
IG_BH04_MG006	319.86	320.12	0.028	7.06	0.22	520	0.86	0.056	1.66	0.019	33.7	3.73	10.8	1.18	8.97	1.48	20.2	0.05	3.15	0.013	1.49	0.028	7.06		
IG_BH04_MG007	345.2	345.46	0.048	7.11	0.14	500	0.84	0.05	1.79	0.028	35.6	3.65	10.2	1.11	8.03	1.4	20	0.05	3.19	0.014	1.59	0.048	7.11		
IG_BH04_MG008	372.4	372.61	0.082	7.05	0.21	480	0.79	0.04	1.78	0.022	35.2	3.65	10.1	1.14	10.45	1.42	19.8	0.05	3.03	0.011	1.55	0.082	7.05		
IG_BH04_MG009	396.81	397.04	0.064	7.08	0.07	540	0.75	0.041	1.81	0.023	38.2	3.49	9.2	0.94	9.67	1.4	19.1	0.05	2.92	0.013	1.62	0.064	7.08		
IG_BH04_MG010	424.32	424.54	0.058	6.99	0.18	490	0.78	0.044	1.79	0.022	32.2	3.25	8.2	0.94	7.85	1.41	19.25	0.07	3.08	0.008	1.53	0.058	6.99		
IG_BH04_MG011	450.46	450.69	0.062	7.27	0.14	520	0.76	0.038	1.88	0.023	34.8	3.72	9.4	1.24	8.26	1.52	19.05	0.07	3.07	0.012	1.52	0.062	7.27		
IG_BH04_MG012	478.95	479.23	0.059	7.36	0.17	610	0.75	0.031	1.89	0.023	36.3	3.65	10.4	1.18	7.63	1.52	20.1	0.07	3.1	0.011	1.66	0.059	7.36		
IG_BH04_MG013	505.81	506.03	0.081	7.42	0.15	440	0.8	0.03	1.97	0.023	37.9	3.87	9.6	1.29	8.52	1.55	19.4	0.07	3.39	0.011	1.41	0.081	7.42		
IG_BH04_MG014	532.61	532.83	0.093	7.48	0.19	500	0.8	0.04	1.99	0.023	38.9	4.1	7.7	1.29	8.22	1.66	20.2	0.07	3.29	0.009	1.55	0.093	7.48		
IG_BH04_MG015	558.87	559.12	0.065	7.4	0.07	449	0.82	0.031	1.99	0.027	37.3	4.1	8.5	1.12	8.48	1.65	19.9	0.07	3.39	0.011	1.55	0.065	7.4		
IG_BH04_MG016	587.3	587.51	0.039	7.09	0.15	530	0.83	0.039	1.36	0.022	21.6	2.44	10.3	2.19	4.7	1.03	17.15	0.06	2.05	0.01	3	0.039	7.09		
IG_BH04_MG017	623.21	623.46	0.081	6.89	0.12	377	1.01	0.059	1.57	0.03	19.7	3.02	9.8	1.91	5.99	1.19	19	0.06	2.89	0.01	2	0.081	6.89		
IG_BH04_MG018	637.58	637.83	0.04	6.93	0.19	510	1	0.059	1.5	0.016	19.8	3.02	12.9	2.44	6.75	1.21	18	0.06	2.6	0.011	2.33	0.04	6.93		
IG_BH04_MG019	664.96	665.2	0.039	7.18	0.17	301	1.17	0.051	1.86	0.024	23.5	3.36	11.1	2.5	4.97	1.28	19.65	0.06	2.95	0.006	1.06	0.039	7.18		
IG_BH04_MG020	691.96	692.21	0.029	7.22	0.12	366	1	0.015	1.9	0.024	27.6	3.43	10.9	1.23	2.26	1.32	18.45	0.06	3.12	0.01	1.15	0.029	7.22		

IG_BH04_MG021	719.74	719.98	0.045	7.46	0.14	500	0.8	0.028	2.01	0.054	40.8	4.47	9.2	1.01	10.05	1.71	19.5	0.07	3.47	0.016	1.55	0.045	7.46
IG_BH04_MG022	740.7	740.96	0.057	7.59	0.15	580	0.78	0.04	2.07	0.026	41.7	4.39	9.6	1.42	8.98	1.72	20.7	0.08	3.36	0.017	1.58	0.057	7.59
IG_BH04_MG023	770.87	771.14	0.037	7.23	0.12	490	1.12	0.04	1.41	0.042	17.95	2.41	9.4	3.38	2.93	1.06	19.5	0.06	2.4	0.014	2.62	0.037	7.23
IG_BH04_MG024	797.28	797.49	0.042	7.04	0.17	510	1.03	0.042	1.5	0.028	25.5	2.58	9	2.71	3.48	1.11	18.45	0.07	2.81	0.013	2.3	0.042	7.04
IG_BH04_MG025	826.21	826.42	0.053	6.95	0.18	444	1.11	0.095	1.55	0.043	22	3.26	10.5	3.38	11.6	1.19	19.65	0.07	3.19	0.013	2.16	0.053	6.95
IG_BH04_MG026	850.19	850.39	0.053	7.34	0.15	421	1.17	0.055	1.76	0.037	22.6	3.43	11.3	2.57	7.47	1.31	20	0.06	3.12	0.014	1.95	0.053	7.34
IG_BH04_MG027	878.52	878.79	0.026	7.15	0.13	550	1.08	0.023	1.63	0.028	20.7	3.2	10.5	2.03	2.4	1.22	19.95	0.06	2.96	0.016	2.25	0.026	7.15
IG_BH04_MG028	903.54	903.76	0.052	7.23	0.13	395	0.9	0.023	1.94	0.03	25.3	5.13	9.7	1.05	5.66	1.61	20.8	0.07	2.39	0.02	1.65	0.052	7.23
IG_BH04_MG029	936.28	936.545	0.06	7.61	0.09	480	0.76	0.029	2.08	0.032	28.1	5.68	10.2	0.99	7.73	1.75	21	0.07	1.96	0.016	1.63	0.06	7.61
IG_BH04_MG030	957.15	957.4	0.055	7.52	0.08	540	0.73	0.024	2.13	0.032	24.8	6.04	10.8	0.93	6.18	1.8	19.95	0.07	2.06	0.016	1.68	0.055	7.52

Analyte Symbol	Mg	Mn	Mo	Na	Nb	Ni	P	Pb	Rb	Re	S	Sb	Sc	Se	Sn	Sr	Ta	Te	Th	Ti	Y
Unit Symbol	%	ppm	ppm	%	ppm	ppm	%	ppm	ppm	ppm	%	ppm	%	ppm							
Detection Limit	0.01	0.2	0.02	0.001	0.005	0.08	0.001	0.01	0.02	0.0004	0.01	0.02	0.01	0.006	0.02	0.02	0.01	0.005	0.004	0.001	0.01
Analysis Method	ME-MS61L																				
IG_BH04_MG001	0.3	229	0.46	3.38	4.93	1.95	0.031	7.81	59.6	<0.0004	<0.01	0.3	2.25	0.017	0.83	255	0.48	<0.005	4.99	0.153	3.47
IG_BH04_MG002	0.27	200	0.51	3.25	4.23	1.73	0.03	7.94	57	<0.0004	<0.01	0.12	1.84	0.012	0.72	255	0.38	<0.005	4.76	0.141	3.13
IG_BH04_MG003	0.31	213	0.64	3.26	4.35	1.97	0.031	7.47	56	<0.0004	<0.01	0.02	2.01	0.006	0.72	259	0.39	<0.005	5.02	0.154	3.28
IG_BH04_MG004	0.29	212	0.54	3.23	4.72	1.82	0.031	8.12	64.6	<0.0004	<0.01	0.03	1.98	0.01	0.75	250	0.54	<0.005	4.98	0.151	3.54
IG_BH04_MG005	0.29	198	0.53	3.23	4.2	1.64	0.03	7.31	62.3	<0.0004	<0.01	0.02	1.9	<0.006	0.75	253	0.48	<0.005	3.94	0.14	3.14

IG_BH04_MG006	0.31	212	0.81	3.31	4.69	1.92	0.032	7.98	57.6	<0.0004	<0.01	0.04	2.19	0.011	0.77	264	0.47	<0.005	3.99	0.153	3.36
IG_BH04_MG007	0.3	208	0.76	3.32	4.44	1.95	0.032	7.53	58.2	<0.0004	<0.01	0.02	2.16	0.008	0.74	268	0.42	<0.005	4.15	0.151	3.27
IG_BH04_MG008	0.3	205	0.75	3.36	4.24	1.87	0.032	6.99	53.3	<0.0004	<0.01	0.02	2.09	0.014	0.78	270	0.37	<0.005	4.12	0.151	3.14
IG_BH04_MG009	0.29	201	0.65	3.27	4.05	1.78	0.032	7.13	54.6	<0.0004	<0.01	<0.02	2.01	0.013	0.7	272	0.35	<0.005	4.11	0.149	3.07
IG_BH04_MG010	0.27	196.5	0.56	3.35	3.75	1.71	0.032	7.2	44.6	<0.0004	<0.01	0.02	1.95	0.013	0.63	269	0.32	<0.005	4.42	0.142	2.66
IG_BH04_MG011	0.3	197.5	0.65	3.35	3.85	2.02	0.035	6.99	47	<0.0004	<0.01	0.02	2.08	0.01	0.66	282	0.31	<0.005	3.92	0.157	2.6
IG_BH04_MG012	0.3	195.5	0.78	3.36	3.81	1.87	0.036	7.2	48.9	<0.0004	<0.01	0.02	2.17	0.008	0.65	288	0.3	<0.005	3.96	0.157	2.67
IG_BH04_MG013	0.31	197.5	0.68	3.41	4.03	1.93	0.038	6.82	47.6	<0.0004	<0.01	0.02	2.12	0.009	0.66	290	0.35	<0.005	4.23	0.164	2.9
IG_BH04_MG014	0.33	209	0.49	3.42	4.11	2.01	0.039	7.08	50.3	<0.0004	<0.01	0.02	2.2	0.008	0.68	297	0.37	<0.005	4.42	0.169	2.83
IG_BH04_MG015	0.34	191	0.54	3.37	4.18	2.01	0.039	7.78	55.5	<0.0004	<0.01	<0.02	2.17	0.012	0.55	295	0.43	<0.005	4.64	0.173	3.34
IG_BH04_MG016	0.21	206	0.68	3.03	4.03	2.1	0.015	12.8	106	<0.0004	<0.01	0.02	2.18	0.006	0.85	167.5	0.39	<0.005	3.57	0.088	2.83
IG_BH04_MG017	0.24	241	0.64	3.2	6.22	2.54	0.02	10.95	77.6	<0.0004	<0.01	<0.02	2.27	0.009	1.11	181	1	<0.005	3.76	0.109	5.8
IG_BH04_MG018	0.24	231	0.86	3.06	5.39	2.51	0.021	10.85	89.3	<0.0004	<0.01	0.02	2.02	0.014	0.98	180	0.84	<0.005	3.65	0.107	4.24
IG_BH04_MG019	0.26	156	0.68	3.63	4.11	2.75	0.023	8.04	49.1	<0.0004	<0.01	<0.02	1.73	0.006	0.68	224	0.58	<0.005	3.77	0.121	2.84
IG_BH04_MG020	0.28	161.5	0.7	3.45	3.29	2.87	0.026	6.5	43.3	<0.0004	<0.01	<0.02	1.71	0.007	0.52	244	0.36	<0.005	4.05	0.14	2.54
IG_BH04_MG021	0.36	274	0.59	3.37	4.16	2.29	0.043	6.61	53.2	<0.0004	<0.01	<0.02	2.16	0.015	0.65	297	0.35	<0.005	4.91	0.188	3.16
IG_BH04_MG022	0.34	321	0.61	3.37	4.08	2.24	0.042	6.98	52	<0.0004	<0.01	<0.02	2.77	0.01	0.67	307	0.28	<0.005	4.43	0.182	2.71
IG_BH04_MG023	0.19	255	0.68	3.18	6.29	1.88	0.017	15.45	105.5	<0.0004	<0.01	0.02	2.26	0.012	1.18	162.5	1.15	<0.005	4.44	0.089	6.67
IG_BH04_MG024	0.2	234	0.58	3.2	5.52	2.06	0.018	12.55	80.3	<0.0004	<0.01	0.02	2.07	0.006	1.03	169.5	0.62	<0.005	4.37	0.095	4.15
IG_BH04_MG025	0.24	229	0.58	3.18	5.97	2.78	0.02	13.6	96.5	<0.0004	<0.01	<0.02	2.38	0.008	1.29	186	1.03	<0.005	4.67	0.115	5.54
IG_BH04_MG026	0.26	240	0.67	3.34	6.02	2.9	0.023	12	76.5	<0.0004	<0.01	<0.02	2.49	0.006	1.17	201	0.85	<0.005	4.32	0.12	5.41
IG_BH04_MG027	0.24	238	0.63	3.14	5.9	2.64	0.021	12.9	86.3	<0.0004	<0.01	<0.02	2.5	0.007	1.08	190	0.86	<0.005	4.18	0.113	4.81
IG_BH04_MG028	0.36	241	0.65	3.35	3.89	3.16	0.03	8.51	50.3	<0.0004	<0.01	<0.02	3.26	0.007	0.73	262	0.41	<0.005	3.41	0.172	5.09
IG_BH04_MG029	0.41	248	0.64	3.39	3.16	3.63	0.033	8.04	45.8	<0.0004	<0.01	0.02	3.64	0.009	0.62	289	0.28	<0.005	3.22	0.184	3.89
IG_BH04_MG030	0.42	250	0.7	3.37	3.3	3.75	0.035	7.96	45.7	<0.0004	<0.01	<0.02	3.93	0.009	0.64	303	0.26	<0.005	2.84	0.197	3.74

Analyte Symbol	Tl	U	V	W	Zn	Zr	Dy	Er	Eu	Gd	Ho	Lu	Nd	Pr	Sm	Tb	Tm	Yb	Si	C	LOI
Unit Symbol	ppm	ppm	ppm	ppm	ppm	ppm	ppm	ppm	ppm	ppm	ppm	ppm	%	%	%						
Detection Limit	0.002	0.01	0.1	0.008	0.2	0.1	0.005	0.004	0.004	0.005	0.002	0.002	0.005	0.004	0.004	0.002	0.002	0.004	0.5	0.01	0.01
Analysis Method	ME-MS61L	ME-MS61L	ME-MS61L	ME-MS61L	ME-MS61L	ME-MS61L	MS61L-REE	pXRF-34	C-IR07	OA-GRA05											
IG_BH04_MG001	0.299	0.94	19	0.11	67.1	127.5	0.722	0.3	0.461	1.13	0.119	0.038	11.25	3.22	1.7	0.142	0.041	0.251	34	0.02	1.04
IG_BH04_MG002	0.286	1.24	17.4	0.045	53.6	120.5	0.654	0.264	0.478	1.105	0.111	0.032	11.65	3.4	1.765	0.143	0.035	0.222	34.7	0.01	0.39
IG_BH04_MG003	0.278	1.04	19.4	0.043	56.6	136	0.699	0.279	0.486	1.115	0.113	0.033	11.8	3.41	1.76	0.14	0.038	0.235	34.1	0.02	0.45
IG_BH04_MG004	0.328	1.46	18.1	0.032	56.1	132.5	0.708	0.31	0.463	1.14	0.116	0.038	12.6	3.66	1.785	0.143	0.043	0.258	33.2	0.01	0.47
IG_BH04_MG005	0.302	1.49	17.5	0.07	51.9	125	0.608	0.285	0.481	0.998	0.107	0.033	10.7	3.16	1.555	0.125	0.04	0.236	34.9	0.01	0.48
IG_BH04_MG006	0.282	0.63	19	0.041	58.7	135.5	0.643	0.284	0.504	1.05	0.108	0.038	11.15	3.24	1.615	0.128	0.041	0.225	33.9	0.02	0.42
IG_BH04_MG007	0.284	0.8	18.7	0.032	54	139	0.675	0.298	0.497	1.065	0.113	0.036	11.6	3.46	1.735	0.138	0.036	0.238	33.7	0.02	-0.86
IG_BH04_MG008	0.273	1.01	18.4	0.033	56.8	132	0.643	0.258	0.494	1.005	0.107	0.036	11.6	3.37	1.65	0.135	0.036	0.212	35.6	0.02	-1.13
IG_BH04_MG009	0.274	1.05	18.7	0.031	55.2	128	0.619	0.272	0.524	1.03	0.107	0.035	12.3	3.65	1.755	0.125	0.034	0.207	34.6	0.02	0.37
IG_BH04_MG010	0.249	0.71	17.8	0.027	54.5	133	0.588	0.247	0.478	0.975	0.095	0.032	10.1	3.01	1.57	0.115	0.032	0.218	33.2	0.01	0.42
IG_BH04_MG011	0.26	0.72	20	0.031	57.1	135.5	0.552	0.249	0.506	0.943	0.095	0.029	10.75	3.21	1.585	0.11	0.032	0.222	33.6	0.02	0.35
IG_BH04_MG012	0.272	0.77	20	0.055	55.7	136.5	0.549	0.247	0.531	0.977	0.097	0.032	11.25	3.4	1.65	0.114	0.032	0.216	35	0.02	0.44
IG_BH04_MG013	0.269	0.84	21.1	0.19	57.7	147	0.601	0.274	0.544	1.015	0.102	0.038	11.8	3.53	1.75	0.121	0.036	0.258	33.6	0.02	0.35
IG_BH04_MG014	0.288	0.74	21.8	0.102	61.7	145	0.593	0.266	0.543	1.03	0.102	0.035	12.05	3.62	1.735	0.12	0.036	0.235	34.5	0.02	0.62
IG_BH04_MG015	0.317	1.64	22.2	0.028	60	148.5	0.668	0.313	0.536	1.05	0.115	0.045	11.7	3.48	1.75	0.13	0.044	0.293	33.3	0.01	0.79
IG_BH04_MG016	0.527	1.11	12.6	0.035	40.7	75.9	0.551	0.257	0.389	0.859	0.098	0.035	7.6	2.14	1.36	0.108	0.035	0.25	35.4	0.04	0.77
IG_BH04_MG017	0.427	2.27	15.3	0.034	48.3	103	1.02	0.526	0.385	1.165	0.191	0.067	7.09	1.945	1.475	0.175	0.075	0.497	36.2	0.02	0.66
IG_BH04_MG018	0.466	0.98	15.2	0.038	48.1	95.3	0.783	0.391	0.401	1.015	0.145	0.057	7.12	1.99	1.345	0.138	0.055	0.376	36.3	0.03	0.42
IG_BH04_MG019	0.273	1.13	16.9	0.029	46.9	107.5	0.567	0.269	0.451	0.913	0.098	0.04	8.33	2.34	1.425	0.108	0.041	0.256	35.2	0.01	0.3
IG_BH04_MG020	0.227	0.99	15.8	0.032	42.8	112.5	0.528	0.238	0.488	0.904	0.089	0.038	9.37	2.71	1.525	0.101	0.033	0.239	35.2	0.01	0.53
IG_BH04_MG021	0.286	0.87	24.2	0.03	57.7	158.5	0.653	0.285	0.563	1.065	0.111	0.04	12.55	3.78	1.83	0.127	0.037	0.259	34.2	0.02	0.69
IG_BH04_MG022	0.293	0.7	23.9	0.031	60.8	153.5	0.59	0.262	0.563	1.045	0.099	0.033	12.8	3.85	1.82	0.116	0.033	0.224	33.2	0.02	0.44
IG_BH04_MG023	0.531	3.03	12.2	0.03	41.6	81.9	1.12	0.593	0.383	1.27	0.208	0.088	6.69	1.825	1.515	0.193	0.087	0.599	36.5	0.02	0.35
IG_BH04_MG024	0.417	2.2	13	0.024	43	97.2	0.775	0.386	0.405	1.08	0.143	0.057	8.85	2.49	1.54	0.138	0.056	0.376	36.4	0.02	0.29

IG_BH04_MG025	0.505	2.65	15.9	0.029	46.3	108	1.025	0.52	0.402	1.245	0.191	0.071	7.99	2.21	1.595	0.179	0.073	0.491	35.7	0.02	0.31
IG_BH04_MG026	0.432	2.57	17.1	0.096	49.4	110.5	0.998	0.515	0.415	1.225	0.184	0.068	8	2.24	1.58	0.169	0.071	0.473	35.3	0.01	0.31
IG_BH04_MG027	0.459	2.78	16	0.032	48.5	105	0.902	0.454	0.417	1.13	0.169	0.063	7.4	2.04	1.435	0.161	0.064	0.437	36.3	0.02	0.38
IG_BH04_MG028	0.307	0.92	29.4	0.027	54.4	80	0.989	0.501	0.457	1.33	0.19	0.064	9.21	2.56	1.76	0.174	0.068	0.453	33.4	0.01	0.52
IG_BH04_MG029	0.277	0.65	30.6	0.035	56.4	73.5	0.752	0.386	0.452	1.095	0.136	0.051	9.8	2.77	1.64	0.138	0.052	0.361	33.1	0.01	0.49
IG_BH04_MG030	0.288	0.63	33.8	0.053	59.1	79.7	0.775	0.375	0.484	1.115	0.145	0.051	8.86	2.48	1.58	0.142	0.054	0.344	31.3	0.01	0.44

**Appendix C: Geophysical Near and Far
Density Log Correction**

The correction was determined by averaging the difference between each laboratory measurement and the field measurement at the corresponding Position, for the near and far density data sets. Forty laboratory core wet density measurements were considered. This correction was applied to the near and far density logs in WellCAD and the updated logs are exported from WellCAD and updated as .LAS files in the NWMO Acquire database.

Position along borehole m	Near Density (ND) g/cm ³	Far Density (FD) g/cm ³	Lab Wet Density g/cm ³	Difference ND-Lab g/cm ³	Difference FD-lab g/cm ³	NDCorrection	FDCorrection
162.5	2.79	2.75	2.67	0.115	0.08	1.043	1.03
163.7	2.77	2.73	2.65	0.124	0.083	1.047	1.031
167.4	2.78	2.69	2.67	0.113	0.024	1.042	1.009
168.1	2.75	2.76	2.64	0.11	0.12	1.042	1.046
213.2	2.79	2.70	2.64	0.153	0.061	1.058	1.023
213.9	2.77	2.69	2.66	0.11	0.032	1.041	1.012
236.4	2.79	2.68	2.67	0.119	0.008	1.045	1.003
238	2.75	2.73	2.64	0.111	0.086	1.042	1.032
267.7	2.76	2.70	2.65	0.109	0.05	1.041	1.019
268	2.80	2.77	2.58	0.217	0.194	1.084	1.075
293.4	2.75	2.70	2.67	0.083	0.033	1.031	1.012
294.5	2.77	2.74	2.66	0.106	0.077	1.04	1.029
317.4	2.78	2.71	2.67	0.107	0.036	1.04	1.013
318.1	2.79	2.71	2.64	0.147	0.066	1.056	1.025
347.4	2.79	2.73	2.68	0.114	0.047	1.042	1.018
348.2	2.77	2.73	2.67	0.096	0.059	1.036	1.022
372	2.74	2.73	2.65	0.086	0.083	1.033	1.031
372.2	2.67	2.66	2.66	0.012	0.005	1.005	1.002
397.8	2.79	2.73	2.65	0.142	0.077	1.053	1.029
423.6	2.78	2.72	2.64	0.144	0.082	1.055	1.031
450.9	2.76	2.73	2.67	0.091	0.064	1.034	1.024
478.1	2.75	2.73	2.68	0.07	0.047	1.026	1.017
505.1	2.77	2.72	2.66	0.111	0.063	1.042	1.024
531.9	2.76	2.73	2.68	0.077	0.049	1.029	1.018
561.3	2.77	2.76	2.67	0.103	0.086	1.038	1.032
586.2	2.78	2.72	2.66	0.125	0.058	1.047	1.022
614.4	2.73	2.70	2.65	0.083	0.051	1.031	1.019
636.8	2.75	2.69	2.7	0.051	-0.012	1.019	0.996
665.4	2.76	2.63	2.67	0.085	-0.04	1.032	0.985
692.4	2.78	2.69	2.67	0.112	0.02	1.042	1.008
711.3	2.79	2.69	2.67	0.117	0.02	1.044	1.008
746.3	2.78	2.69	2.68	0.101	0.012	1.038	1.004
771.6	2.72	2.64	2.66	0.056	-0.017	1.021	0.994
795.3	2.72	2.65	2.65	0.07	0.001	1.026	1
825.3	2.72	2.73	2.66	0.06	0.067	1.022	1.025
849.3	2.76	2.68	2.65	0.107	0.031	1.04	1.012
877.8	2.73	2.65	2.65	0.084	-0.003	1.032	0.999
904	2.74	2.68	2.69	0.051	-0.011	1.019	0.996
931.1	2.76	2.75	2.64	0.117	0.106	1.044	1.04
959	2.78	2.70	2.69	0.091	0.012	1.034	1.005
Mean Correction						1.038	1.018
Standard deviation						0.013	0.016

**Appendix D: Structure log integration
methodology**

Borehole IG_BH04 - Structure type and position verification and the integration activity to define the azimuth of the arbitrary reference line.

Introduction

The orientation of all structures measured during core logging, as described in the WP03 Data Reports, are initially defined based on alpha and beta angles relative to (1) the core axis, and (2) an arbitrary reference line drawn along the length of each core run. Since the core was not oriented, these relative orientation angles (alpha/beta for planes; gamma/delta for lineations on planes), for each logged structure need to be corrected to a true orientation in order to produce the final structural log for IG_BH04.

A final structural log was produced by comparing the core logged structures and the televiewer logged structures. This appendix describes the methodology used to compare the structures from core and televiewer logging to (1) assess the nature of the structure type, (2) determine a correct position of the structure, and (3) identify the angle of each arbitrary reference line traced on each core run relative to low side (reference line correction factor, $\beta_{\text{correction}}$).

The process described in this appendix were the steps taken to develop a *final structure log* that included the final assignment of structure positions along borehole, positional discrepancies, structure type (e.g., vein, foliation, etc.), structure dip and dip direction and/or alpha and beta, and structure geological aperture.

Correction and verification Methodology

The following sections describe the steps to *correct* or *verify* individual structures recorded in core logging and televiewer logging activities, which were ultimately used to form the final structural log.

Structure Type and Position Verification

Based on the integration between the two datasets, the structures were classified as being observed in 'both' datasets, in 'core logging only', or in 'televiewer only'. When a structure was observed in both datasets, the position and structure type recorded from core logging were used as the final structure position along borehole and final structure type. For structures only seen in the televiewer survey, a positional correction was applied based on the positional offset calculated from the structures observed in both datasets. Positional corrections were applied to these structures in a way as to preserve structure order. Additional detail relating to the positional corrections applied to structures identified from the televiewer surveys is discussed in WP05 Data Report (Golder, 2020c).

At this stage, each individual structure that was common to both data sets was evaluated, and an integrated structure was carried forward to the *final structure log*. The integration of common structures was as follows:

- a) Position along borehole of the final structure was based on the position of the core logged structure;
- b) Dip and Dip direction of the final structure was based on the orientation of the televiewer logged structure (relative to *low side*);
- c) Structure type was assigned, based on the core logging;
- d) Other characteristics, such as mineral infilling, etc. was assigned based on core logging.

If a structure was identified only in the televiewer logs, core run photographs acquired during core logging were reviewed to aid in evaluating if this structure was present in the core. If it is determined that this is a real structure and not a drill feature, it was included in the final

structural log, along with its interpreted structure type, dip and dip direction, and corrected position.

If a structure was identified only in core logging, this structure was carried forward to the final structural log, along with its structure type, alpha and beta angles, and position.

Structure Orientation

For each core run logged in WP03, an arbitrary reference line was drawn along the length of the core, where the location is initially unknown. Orientations of all structures identified during core logging were described relative to this reference line (beta angles) in each run. The purpose of this section is to describe the process used to define the *true* location, from the 'low side' of the borehole, of this reference line (between 0 – 360°) by integrating the oriented televiewer images.

When a structure was observed in both datasets, the alpha and beta angles from the televiewer survey were used as the final structure orientation.

For structures only observed in core logging, a reference line correction factor was applied to the beta angles in order to locate the arbitrary reference line relative to the bottom of the *borehole* ('low-side'). The reference line correction factor relies on structures seen in both datasets within the same continuously referenced interval. The correction factor takes an average of the beta angle correction(s), which is the angle from the borehole 'low-side' (identified from the televiewer survey) to the arbitrary reference from core logging, calculated for each structure ($\beta_{\text{correction}} = \beta_{\text{televiewer}} - \beta_{\text{core logging}}$). Figure 1 shows how the beta angle correction relates to the arbitrary reference line and the borehole 'low-side'.

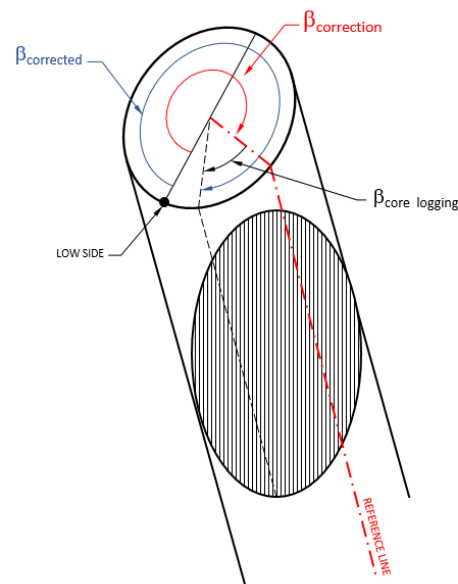


Figure 1: Schematic Showing Beta Angle Correction

$$\beta_{\text{core logging}} + \text{Reference Line Correction Factor (Average)} = \beta_{\text{corrected}}$$

(if $\beta_{\text{corrected}} > 360^\circ$, subtract 360°)

If no core logged structure within a continuously referenced interval was identified in the televiewer logs, then no reference line correction could be developed and orientation of the structure(s) within that interval was not possible.

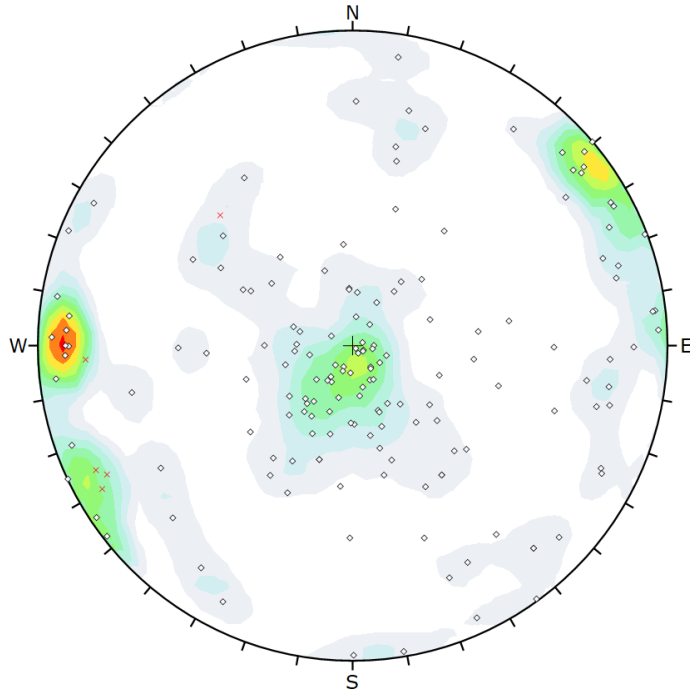
Dip and dip direction of the structures were calculated using the software DIPS© (Version 7), by Rocscience, which processes the data by using stereographic projections based on the alpha and corrected beta measurements and to the borehole deviation survey. The borehole survey file generated from the average of six separate televiewer probe runs using 1 m intervals between survey points was used for the projection of the final structure orientations.

Final Structural Log

The integration of core logged structures and televiewer logged structures resulted in a final structural log. The result of the final structural log includes a table that captures a complete set of attributes of each structure recorded either from core logging, televiewer logging, or a combination of both. Where certain attributes are duplicated between the two logging approaches (i.e., structure type, or position) decisions were made to carry forward the most accurate value to the final structure log. For example, position values and structure type were obtained from the core logging structures.

**Appendix E: Stereonets of Fractures by
Structural Unit**

SU1 (0 – 98.75 m)



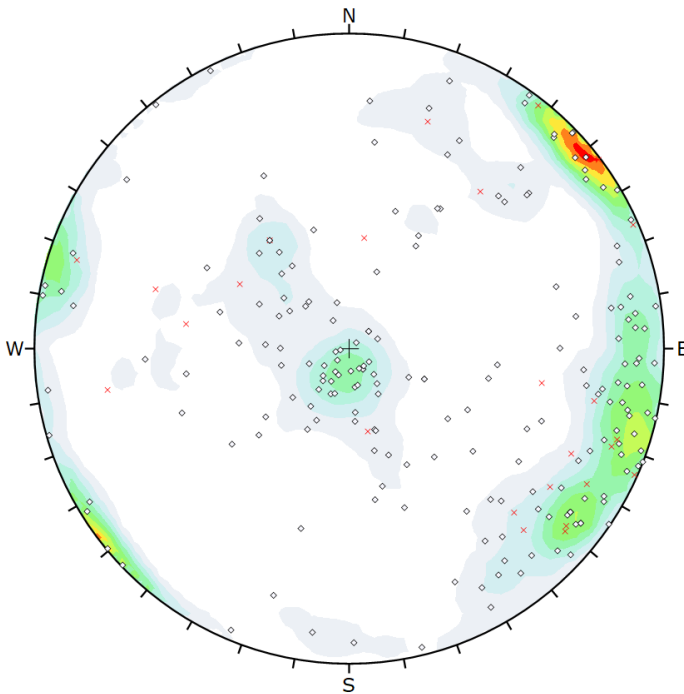
Symbol	STRUCT TYPE	Quantity
◇	JN	164
×	VN	5

Color	Density Concentrations
	0.00 - 0.90
	0.90 - 1.80
	1.80 - 2.70
	2.70 - 3.60
	3.60 - 4.50
	4.50 - 5.40
	5.40 - 6.30
	6.30 - 7.20
	7.20 - 8.10
	8.10 - 9.00

Contour Data	Pole Vectors
Maximum Density	8.39%
Contour Distribution	Fisher
Counting Circle Size	1.0%

Plot Mode	Pole Vectors
Vector Count (Weighted)	323 (169 Entries)
Terzaghi Weighting	Minimum Bias Angle 15°
Hemisphere	Lower
Projection	Equal Area

SU2 (98.75 – 152.75 m)



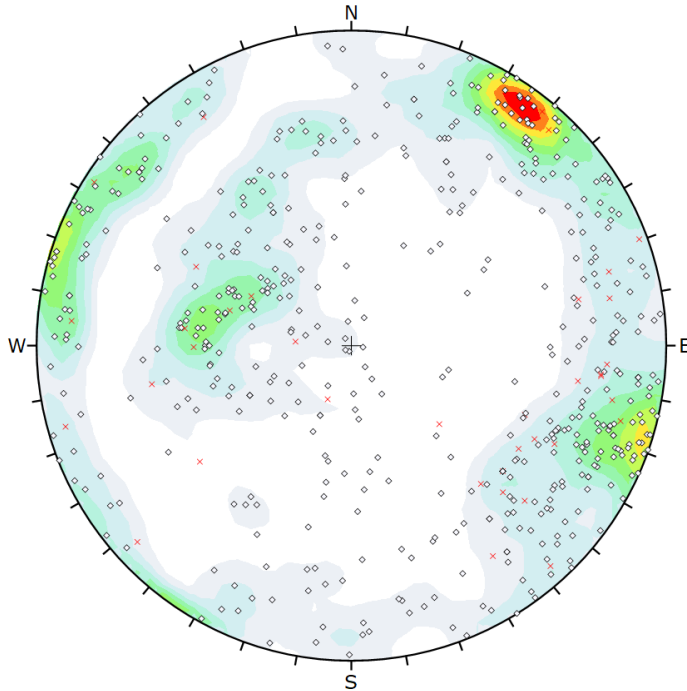
Symbol	STRUCT TYPE	Quantity
◇	JN	204
×	VN	25

Color	Density Concentrations
	0.00 - 0.90
	0.90 - 1.80
	1.80 - 2.70
	2.70 - 3.60
	3.60 - 4.50
	4.50 - 5.40
	5.40 - 6.30
	6.30 - 7.20
	7.20 - 8.10
	8.10 - 9.00

Contour Data	Pole Vectors
Maximum Density	8.46%
Contour Distribution	Fisher
Counting Circle Size	1.0%

Plot Mode	Pole Vectors
Vector Count (Weighted)	451 (229 Entries)
Terzaghi Weighting	Minimum Bias Angle 15°
Hemisphere	Lower
Projection	Equal Area

SU3 (152.75 – 572.75 m)



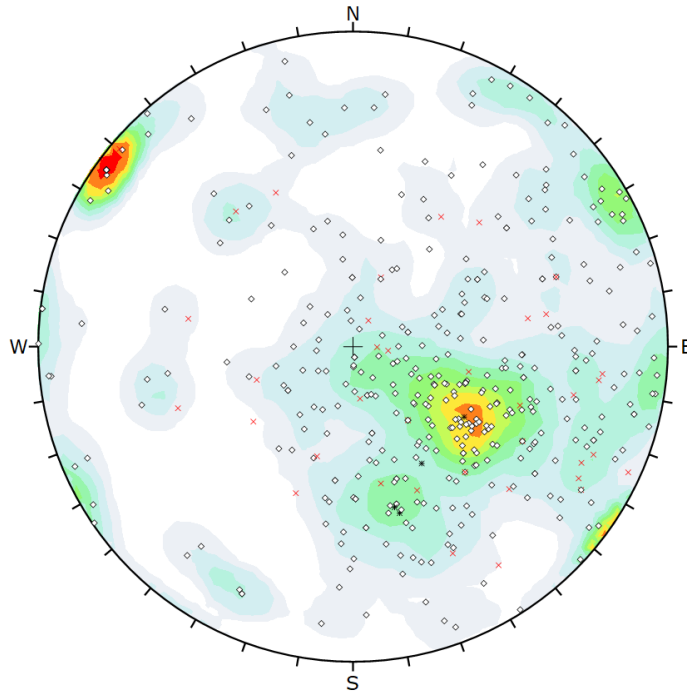
Symbol	STRUCT TYPE	Quantity
◇	JN	528
×	VN	37

Color	Density Concentrations
	0.00 - 0.60
	0.60 - 1.20
	1.20 - 1.80
	1.80 - 2.40
	2.40 - 3.00
	3.00 - 3.60
	3.60 - 4.20
	4.20 - 4.80
	4.80 - 5.40
	5.40 - 6.00

Contour Data	Pole Vectors
Maximum Density	5.91%
Contour Distribution	Fisher
Counting Circle Size	1.0%

Plot Mode	Pole Vectors
Vector Count (Weighted)	1252 (565 Entries)
Terzaghi Weighting	Minimum Bias Angle 15°
Hemisphere	Lower
Projection	Equal Area

SU4 (572.75 – 647.75 m)



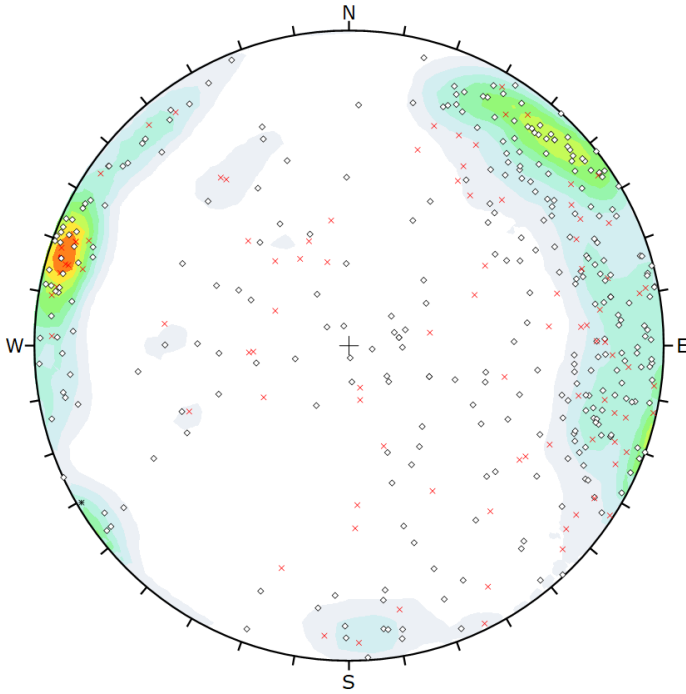
Symbol	STRUCT TYPE	Quantity
*	FLT	4
◇	JN	392
×	VN	37

Color	Density Concentrations
	0.00 - 0.55
	0.55 - 1.10
	1.10 - 1.65
	1.65 - 2.20
	2.20 - 2.75
	2.75 - 3.30
	3.30 - 3.85
	3.85 - 4.40
	4.40 - 4.95
	4.95 - 5.50

Contour Data	Pole Vectors
Maximum Density	5.25%
Contour Distribution	Fisher
Counting Circle Size	1.0%

Plot Mode	Pole Vectors
Vector Count (Weighted)	691 (433 Entries)
Terzaghi Weighting	Minimum Bias Angle 15°
Hemisphere	Lower
Projection	Equal Area

SU5 (647.75 – 878.75 m)



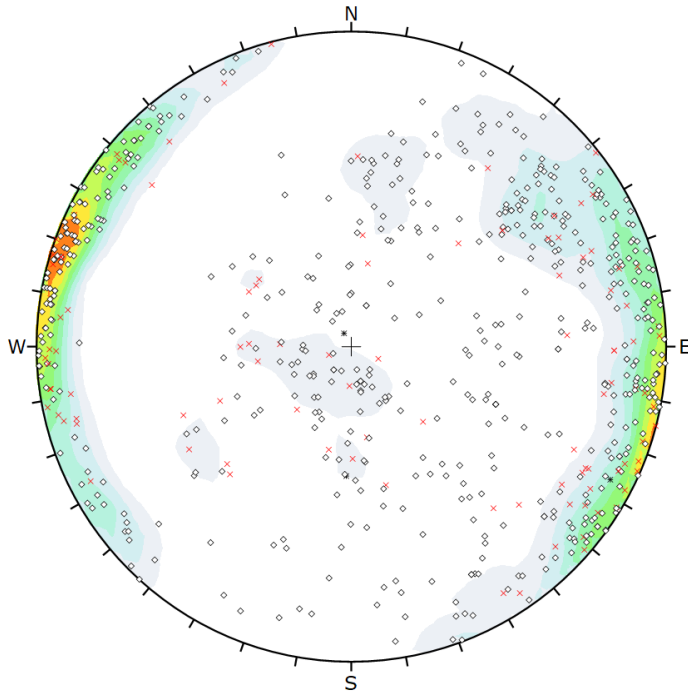
Symbol	STRUCT TYPE	Quantity
*	FLT	1
◇	JN	317
×	VN	93

Color	Density Concentrations
	0.00 - 0.90
	0.90 - 1.80
	1.80 - 2.70
	2.70 - 3.60
	3.60 - 4.50
	4.50 - 5.40
	5.40 - 6.30
	6.30 - 7.20
	7.20 - 8.10
	8.10 - 9.00

Contour Data	Pole Vectors
Maximum Density	8.23%
Contour Distribution	Fisher
Counting Circle Size	1.0%

Plot Mode	Pole Vectors
Vector Count (Weighted)	894 (411 Entries)
Terzaghi Weighting	Minimum Bias Angle 15°
Hemisphere	Lower
Projection	Equal Area

SU6 (878.75 – 1000.2 m)



Symbol	STRUCT TYPE	Quantity
*	FLT	3
◇	JN	557
×	VN	103

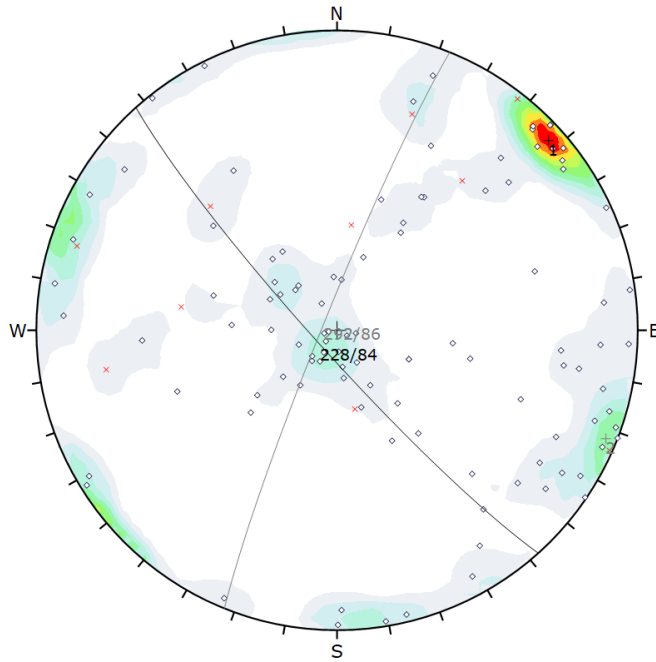
Color	Density Concentrations
	0.00 - 0.90
	0.90 - 1.80
	1.80 - 2.70
	2.70 - 3.60
	3.60 - 4.50
	4.50 - 5.40
	5.40 - 6.30
	6.30 - 7.20
	7.20 - 8.10
	8.10 - 9.00

Contour Data	Pole Vectors
Maximum Density	8.01%
Contour Distribution	Fisher
Counting Circle Size	1.0%

Plot Mode	Pole Vectors
Vector Count (Weighted)	1329 (663 Entries)
Terzaghi Weighting	Minimum Bias Angle 15°
Hemisphere	Lower
Projection	Equal Area

**Appendix F: Stereonets of IG_BH04
High Fracture Frequency Intervals
(HFFI)**

IG_BH04 HFFI_1 (94.08 – 116.97 m):



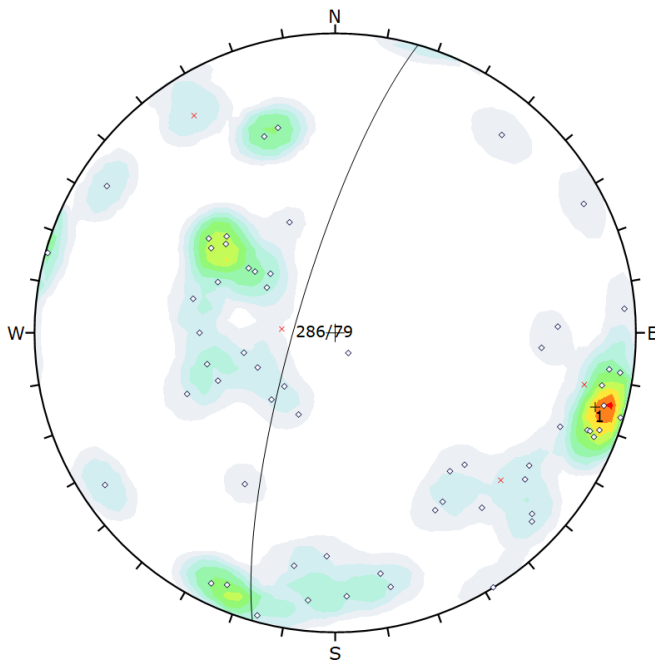
Symbol	STRUCT TYPE	Quantity
◊	JN	106
×	VN	10

Color	Density Concentrations
	0.00 - 1.20
	1.20 - 2.40
	2.40 - 3.60
	3.60 - 4.80
	4.80 - 6.00
	6.00 - 7.20
	7.20 - 8.40
	8.40 - 9.60
	9.60 - 10.80
	10.80 - 12.00

Contour Data	Pole Vectors
Maximum Density	11.87%
Contour Distribution	Fisher
Counting Circle Size	1.0%

Plot Mode	Pole Vectors
Vector Count (Weighted)	246 (116 Entries)
Terzaghi Weighting	Minimum Bias Angle 15°
Hemisphere	Lower
Projection	Equal Area

IG_BH04 HFFI_2 (310.08 – 325.75 m):



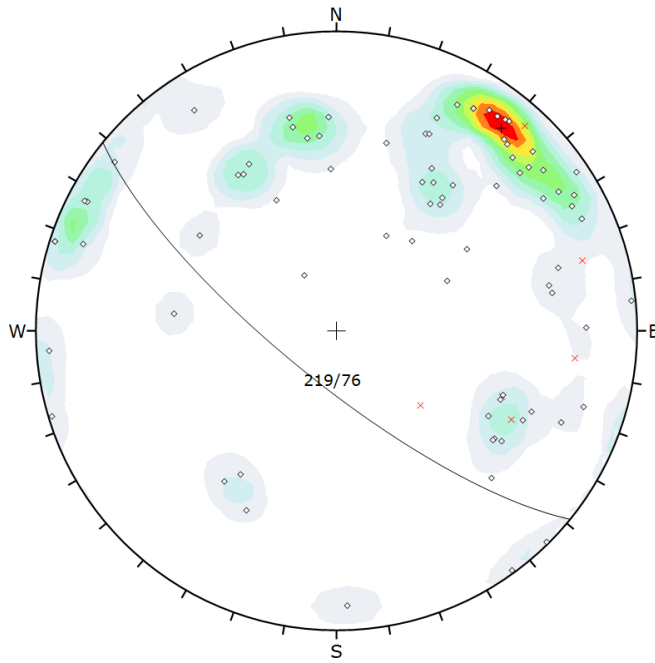
Symbol	STRUCT TYPE	Quantity
◊	JN	61
×	VN	4

Color	Density Concentrations
	0.00 - 1.10
	1.10 - 2.20
	2.20 - 3.30
	3.30 - 4.40
	4.40 - 5.50
	5.50 - 6.60
	6.60 - 7.70
	7.70 - 8.80
	8.80 - 9.90
	9.90 - 11.00

Contour Data	Pole Vectors
Maximum Density	10.21%
Contour Distribution	Fisher
Counting Circle Size	1.0%

Plot Mode	Pole Vectors
Vector Count (Weighted)	136 (65 Entries)
Terzaghi Weighting	Minimum Bias Angle 15°
Hemisphere	Lower
Projection	Equal Area

IG_BH04 HFFI_3 (424.25 – 441.33 m):



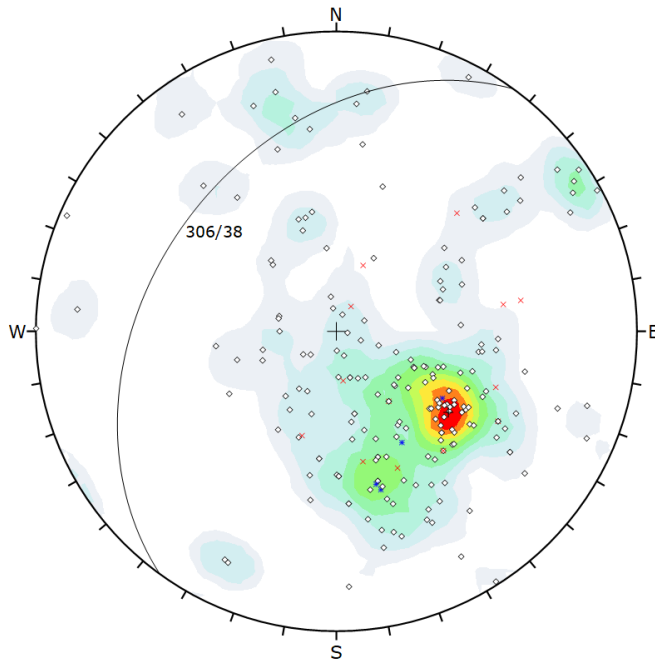
Symbol	STRUCT TYPE	Quantity
◊	JN	80
×	VN	6

Color	Density Concentrations
	0.00 - 1.30
	1.30 - 2.60
	2.60 - 3.90
	3.90 - 5.20
	5.20 - 6.50
	6.50 - 7.80
	7.80 - 9.10
	9.10 - 10.40
	10.40 - 11.70
	11.70 - 13.00

Contour Data	Pole Vectors
Maximum Density	12.98%
Contour Distribution	Fisher
Counting Circle Size	1.0%

Plot Mode	Pole Vectors
Vector Count (Weighted)	184 (86 Entries)
Terzaghi Weighting	Minimum Bias Angle 15°
Hemisphere	Lower
Projection	Equal Area

IG_BH04 HFFI_4 (570.71 – 588.00 m):



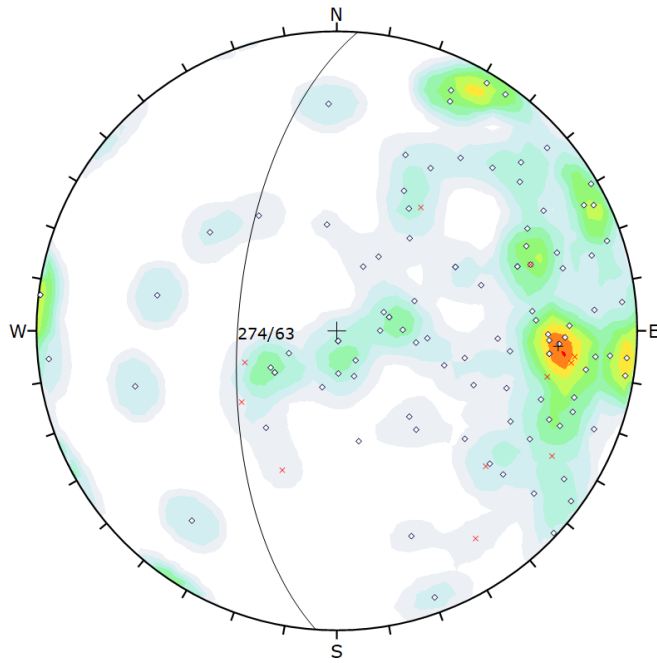
Symbol	STRUCT TYPE	Quantity
★	FLT	4
◊	JN	198
×	VN	13

Color	Density Concentrations
	0.00 - 0.90
	0.90 - 1.80
	1.80 - 2.70
	2.70 - 3.60
	3.60 - 4.50
	4.50 - 5.40
	5.40 - 6.30
	6.30 - 7.20
	7.20 - 8.10
	8.10 - 9.00

Contour Data	Pole Vectors
Maximum Density	8.93%
Contour Distribution	Fisher
Counting Circle Size	1.0%

Plot Mode	Pole Vectors
Vector Count (Weighted)	308 (215 Entries)
Terzaghi Weighting	Minimum Bias Angle 15°
Hemisphere	Lower
Projection	Equal Area

IG_BH04 HFFI_5 (618.17 – 637.65 m):



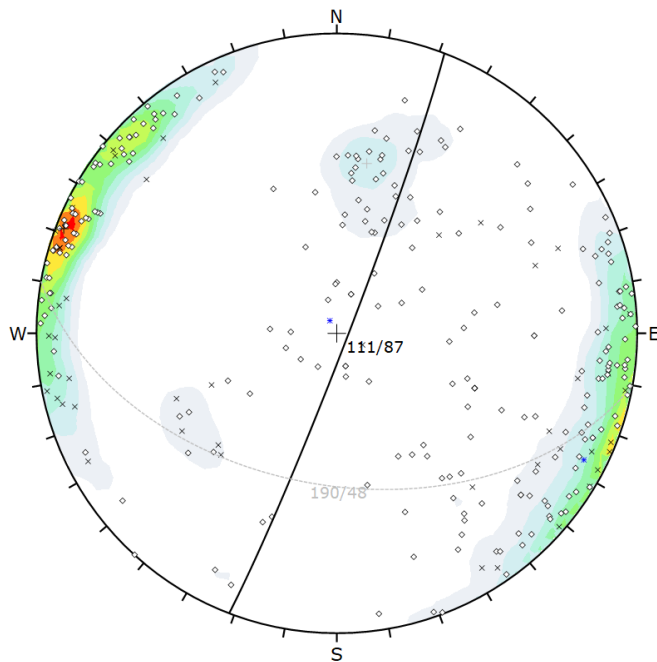
Symbol	STRUCT TYPE	Quantity
◊	JN	104
×	VN	11

Color	Density Concentrations
	0.00 - 0.70
	0.70 - 1.40
	1.40 - 2.10
	2.10 - 2.80
	2.80 - 3.50
	3.50 - 4.20
	4.20 - 4.90
	4.90 - 5.60
	5.60 - 6.30
	6.30 - 7.00

Contour Data	Pole Vectors
Maximum Density	6.38%
Contour Distribution	Fisher
Counting Circle Size	1.0%

Plot Mode	Pole Vectors
Vector Count (Weighted)	188 (115 Entries)
Terzaghi Weighting	Minimum Bias Angle 15°
Hemisphere	Lower
Projection	Equal Area

IG_BH04 HFFI_6 (943.62 – 978.81 m):



Symbol	STRUCT TYPE	Quantity
★	FLT	2
◊	JN	248
×	VN	47

Color	Density Concentrations
	0.00 - 1.20
	1.20 - 2.40
	2.40 - 3.60
	3.60 - 4.80
	4.80 - 6.00
	6.00 - 7.20
	7.20 - 8.40
	8.40 - 9.60
	9.60 - 10.80
	10.80 - 12.00

Contour Data	Pole Vectors
Maximum Density	11.19%
Contour Distribution	Fisher
Counting Circle Size	1.0%

Plot Mode	Pole Vectors
Vector Count (Weighted)	612 (297 Entries)
Terzaghi Weighting	Minimum Bias Angle 15°
Hemisphere	Lower
Projection	Equal Area

**Appendix G: Summary of borehole logs
at 1:1,000 scale**

